



5-2011

## **A Thermal Feasibility Study and Design of an Air-cooled Rectangular Wide Band Gap Inverter**

Jacob Christopher Faulkner  
jfaulkn4@utk.edu

Follow this and additional works at: [https://trace.tennessee.edu/utk\\_gradthes](https://trace.tennessee.edu/utk_gradthes)

 Part of the [Heat Transfer, Combustion Commons](#)

---

### **Recommended Citation**

Faulkner, Jacob Christopher, "A Thermal Feasibility Study and Design of an Air-cooled Rectangular Wide Band Gap Inverter. " Master's Thesis, University of Tennessee, 2011.  
[https://trace.tennessee.edu/utk\\_gradthes/870](https://trace.tennessee.edu/utk_gradthes/870)

This Thesis is brought to you for free and open access by the Graduate School at TRACE: Tennessee Research and Creative Exchange. It has been accepted for inclusion in Masters Theses by an authorized administrator of TRACE: Tennessee Research and Creative Exchange. For more information, please contact [trace@utk.edu](mailto:trace@utk.edu).

To the Graduate Council:

I am submitting herewith a thesis written by Jacob Christopher Faulkner entitled "A Thermal Feasibility Study and Design of an Air-cooled Rectangular Wide Band Gap Inverter." I have examined the final electronic copy of this thesis for form and content and recommend that it be accepted in partial fulfillment of the requirements for the degree of Master of Science, with a major in Mechanical Engineering.

Rao V. Arimilli, Major Professor

We have read this thesis and recommend its acceptance:

Jay Frankel, James Conklin

Accepted for the Council:

Carolyn R. Hodges

Vice Provost and Dean of the Graduate School

(Original signatures are on file with official student records.)

To the Graduate Council:

I am submitting herewith a thesis written by Jacob Christopher Faulkner entitled “A Thermal Feasibility Study and Design of an Air-Cooled Rectangular Wide Band Gap Inverter.” I have examined the final electronic copy of this thesis for form and content and recommend that it be accepted in partial fulfillment of the requirements for the degree of Master of Science, with a major in Mechanical Engineering.

Rao V. Arimilli , Major Professor

We have read this thesis  
and recommend its acceptance:

Jay Frankel

James Conklin

Accepted for the Council:

Carolyn R. Hodges  
Vice Provost and Dean of the Graduate School

(Original signatures are on file with official student records.)

A Thermal Feasibility Study and the Design of an Air-Cooled Rectangular Wide Band Gap  
Inverter

A Thesis  
Presented for the  
Master of Science  
Degree  
The University of Tennessee, Knoxville

Jacob Christopher Faulkner

May 2011

## **Acknowledgements**

I would like to thank everybody who has helped me complete my Master of Science degree. I have received a lot of help along the way, and would not have been able to complete this degree without the following individuals.

I would like acknowledge Dr. Rao V. Arimilli and Mr. Madhu Chinthavali. Dr. Arimilli has provided guidance in my academic endeavors since my undergraduate degree. His level of knowledge and skills can only be obtained over a long career of academic and research excellence and I feel lucky to have studied and worked with him. Many thanks are extended to Mr. Chinthavali for sponsoring my research endeavors. I would also like to extend special thanks to Dr. Jay Frankel and Dr. James Conklin for serving on my thesis committee.

I would also like to thank my parents and grandparents for all of their financial and emotional support throughout my education. I am very thankful to have a loving and supportive family. I would not have become the man I am today without them.

Finally, I would like to give thanks and praise to my father in heaven. I am eternally grateful for the challenges he has blessed me with throughout my professional and academic endeavors. I will always serve faithfully in his name.

## **Abstract**

All power electronics consist of solid state devices that generate heat. Managing the temperature of these devices is critical to their performance and reliability. Traditional methods involving liquid-cooling systems are expensive and require additional equipment for operation. Air-cooling systems are less expensive but are typically less effective at cooling the electronic devices. The cooling system that is used depends on the specific application.

Until recently, silicon based devices have been used for the solid-state devices in power electronics. Newly developed silicon-carbide based wide band gap devices operate at maximum temperatures higher than traditional silicon devices. Due to the permissible increase in operating temperatures, it has been proposed to develop an air-cooling system for an inverter consisting of silicon carbide devices.

This thesis presents recent research efforts to develop the proposed air-cooling system. The thermal performance of the each design iteration was determined by numerical simulations via the finite element method in both steady state and transient mode using COMSOL Multi-physics software version 3.5a. For all simulations presented in this thesis, the heat dissipated in the MOSFETS and diodes are specified as functions of current, voltage, switching frequency, and junction temperature. For both the steady state and transient simulations, the junction temperature was determined iteratively. Additionally in the transient simulations, the current distribution is a function of time and was deduced from the EPA US06 drive cycle. After several design iterations, a thermally feasible design has been reached. This design is presented in detail in this thesis.

Under transient simulations of the final design, the maximum junction temperatures were determined to be below 146 °C for air flow rates of 30 and 60 CFM, which is substantially lower than the 250 °C maximum allowable junction temperature of Si-C devices. However for steady state simulations, junction temperatures were found to be much higher than the transient simulations. It was determined that a minimum flow rate of 50 CFM is required to meet the temperature requirements of the Si-C devices under steady state operating conditions. The power density of this air-cooled final design is 11.75 kW/L, and it is competitive with liquid-cooled systems.

# Table of Contents

<b>Chapter 1 - Introduction</b>	<b>1</b>
1.1 Motivation for Air-Cooling	2
1.2 Objectives of this Study	3
1.3 Overall Design Considerations	4
<b>Chapter 2 - Literature Review</b>	<b>5</b>
2.1 Inverter Basics	5
2.2 State of Current Research	8
<b>Chapter 3 - Problem Statement and Boundary Conditions</b>	<b>14</b>
3.1 The Problem of Forced Convection Heat Transfer	14
3.2 Problem Solving Methodology	16
3.3 A Premise on Turbulence	17
3.4 Reynolds Number Calculations	18
3.5 Steady State Mass and Momentum Transport Simulations	20
3.6 Steady State Energy Transport Simulations	27
3.7 Heat Generation Equations	30
3.8 Transient Energy Transport Simulations	33
3.9 Input Parameters for the Simulations	35
3.10 Summary of the Thermal-Fluid Interaction Simulations	37
<b>Chapter 4 - Module Design Details</b>	<b>39</b>
4.1 Motivation for the Module Based Design	39
4.2 DBA Card	42
4.3 Motivation for the Relative Dimensions of the Trace	47
4.4 Electrical Connections	48
4.5 Module Casing	49
4.6 Assembly Details	51
4.7 Power Density Calculations	52
<b>Chapter 5 - Results and Discussion</b>	<b>53</b>
5.1 Steady State Velocity Results	53
5.2 Steady State Temperature Results	58
5.3 Special Steady State Simulation	82
5.4 Transient Temperature Results	85
5.5 Validation of the Results	89



<b>Chapter 6 - Conclusions</b>	<b>91</b>
<b>List of References</b>	<b>93</b>
<b>Vita</b>	<b>95</b>

## List of Figures

Figure 2.1	Electrical schematic of a voltage source inverter [3]	6
Figure 2.2	Isometric view of the FY 2009 design without fins [1]	9
Figure 2.3	Isometric view of the FY 2009 design with fins [1]	9
Figure 2.4	Isometric view of the velocity field of the FY 2009 design without fins [1]	10
Figure 2.5	Isometric view of the solid temperature distribution of the FY 2009 design without fins [1]	10
Figure 2.6	Isometric view of the velocity field of the FY 2009 design with fins [1]	11
Figure 2.7	Isometric view of the solid temperature distribution of the FY 2009 design with fins [1]	11
Figure 3.1	Schematic of the mean and fluctuating components of the velocity field	21
Figure 3.2	Plot of the heat generation equations	32
Figure 3.3	Plot of the input current for the transient simulations	34
Figure 3.4	Flow chart of the simulations	38
Figure 4.1	Isometric view of a single module	40
Figure 4.2	Front and isometric views of a stack of modules	40
Figure 4.3	Front and isometric views of an exploded DBA card	43
Figure 4.4	Front and Isometric views of the finned flow channel	45
Figure 4.5	Front and isometric views of an exploded module assembly	46
Figure 4.6	Front and isometric views of the assembled module	46
Figure 4.7	Top view of the trace with dimensions	47

Figure 4.8	Isometric view of the electrical connections	48
Figure 4.9	Isometric view of the exploded module casing	50
Figure 4.10	Isometric view of the exploded module assembly	51
Figure 4.11	Isometric view of the assembled module with dimensions	52
Figure 5.1	Isometric view of the velocity field	54
Figure 5.2	Top view of a slice plot of the velocity field	54
Figure 5.3	Isometric view of the pressure distribution in the fluid domain	56
Figure 5.4	Plot of the pressure drop across the inverter versus flow rate	56
Figure 5.5	Plot of the ideal blower power requirements versus flow rate	57
Figure 5.6	Isometric view of the temperature distribution with $Q = 60$ CFM	58
Figure 5.7	Isometric view of the temperature distribution with $Q = 40$ CFM	59
Figure 5.8	Plot of the device temperatures versus $T_{inlet}$	61
Figure 5.9	Plot of the heat generation rates versus $T_{inlet}$	62
Figure 5.10	Top view of the device temperatures	64
Figure 5.11	Plot of MOSFET temperatures versus $T_{inlet}$	65
Figure 5.12	Plot of the diode temperatures versus $T_{inlet}$	66
Figure 5.13	Schematic of the card illustrating the location of the devices	66
Figure 5.14	Isometric view of the module illustrating the location of the vertical planes used in the slice plots	67
Figure 5.15	Slice plots of the temperature distribution on the front plane	69
Figure 5.16	Slice plots of the temperature distribution on the middle plane	69
Figure 5.17	Slice plots of the temperature distribution on the back plane	69

Figure 5.18	Isometric view of the module illustrating the location of the horizontal planes used in the slice plots	70
Figure 5.19	Slice plots of the temperature distribution on the top plane	72
Figure 5.20	Slice plots of the temperature distribution on the middle plane	72
Figure 5.21	Slice plots of the temperature distribution on the bottom plane	72
Figure 5.22	Slice plots of the temperature distribution with $Q = 40$ and $60$ CFM	73
Figure 5.23	Slice plots of the temperature distribution with $Q = 40$ and $60$ CFM	73
Figure 5.24	Isometric view of the temperature distribution in the phase connection	74
Figure 5.25	Isometric view of the temperature distribution in the gate connections	75
Figure 5.26	Isometric view of the temperature distribution in the DC negative connection	76
Figure 5.27	Isometric view of the temperature distribution in the DC positive connection	76
Figure 5.28	Plot of the phase connection temperatures versus $T_{inlet}$	77
Figure 5.29	Plot of the gate connection temperatures versus $T_{inlet}$	78
Figure 5.30	Plot of the DC connection temperatures versus $T_{inlet}$	78
Figure 5.31	Isometric view of the temperature distribution in the module casing	80
Figure 5.32	Isometric view of the fluid temperature distribution	81
Figure 5.33	Top view of a slice plot of the fluid temperature distribution	82
Figure 5.34	Side view of a slice plot of the fluid temperature distribution	82
Figure 5.35	Plot of the input current for the transient simulations with red lines showing the average current over three distinct time intervals	85
Figure 5.36	Top view of the card with results from the special steady state simulation	86

Figure 5.37	Plots of the transient results showing the effect of changing one of the input parameters	89
Figure 5.38	Plots of the results for all 16 transient simulations	90

## List of Tables

Table 2.1	Results from the FY 2009 study	8
Table 3.1	Range of Reynolds numbers encountered based on inlet conditions	18
Table 3.2	Range of Reynolds numbers encountered based on channel conditions	19
Table 3.3	Constants used in the k- $\epsilon$ closure model	23
Table 3.4	Constants used in the heat generation equations	31
Table 3.5	Properties used in the simulations	36
Table 5.1	Results for the steady state velocity simulations	57
Table 5.2	Results of the steady state temperature simulations for device temperatures and heat generation rates	62
Table 5.3	Results of the steady state temperature simulations to illustrate the nonlinear trend in the results	63
Table 5.4	Results of the steady state temperature simulations for the temperature of the connections and the capacitor	79
Table 5.5	Comparison of the results of the steady state temperature simulations from the FY 2009 and FY 2010 studies	83
Table 5.6	Average current of the transient current distribution over three intervals	84
Table 5.7	Results of the transient temperature simulations for maximum device temperatures	87

# Nomenclature

A	area
a	electrical phase
AC	alternating-current
Al	aluminum
AlN	aluminum nitride
b	electrical phase
c	electrical phase
Cu	copper
CFD	computational fluid dynamics
C <sub>p</sub>	specific heat at constant pressure
CTE	coefficient of thermal expansion
D <sub>h</sub>	hydraulic diameter
DBA	direct bonded aluminum
DBC	direct bonded copper
DC	direct-current
DNS	direct numerical simulation
$\dot{E}_{Gen}$	heat generation rate
EMI	electromagnetic interference
EPA	Environmental Protection Agency
<b>F</b>	body force
FEA	finite element analysis

$f_{sw}$	switching frequency
FY	fiscal year
HEV	hybrid electric vehicle
H	heat transfer coefficient
$\bar{h}$	average heat transfer coefficient
i	current
<b>I</b>	identity matrix
$I_T$	turbulence intensity
IGBT	insulated gate bipolar transistor
$i(t)$	time dependent current
k	thermal conductivity
$k_T$	turbulent thermal conductivity
$k$	turbulent kinetic energy production
K	von Karman constant
$l^*$	viscous length scale
$L_T$	turbulent length scale
$\dot{m}$	mass flow rate
MOSFET	metal oxide semiconductor field effect transistor
<b>n</b>	outward unit normal vector
NTRC	National Transportation Research Center
ORNL	Oak Ridge National Laboratory
P	power



P	perimeter
$P_{\text{cond}}$	conduction losses
$P_{\text{swit}}$	switching losses
PF	power factor
PHEV	plug-in hybrid electric vehicle
PWM	pulse width modulation
Pr	Prandtl number = $\mu C_p/k$
p	pressure
$\bar{p}$	mean pressure
Q	volumetric flow rate
$q'''$	volumetric heat generation
q	heat transfer rate
$q''$	heat transfer per unit area
RANS	Reynolds averaged Navier-Stokes equations
$Re_D$	Reynolds number based on diameter = $\rho U D/\mu$
$Re_{D_h}$	Reynolds number based on hydraulic diameter = $\rho U D_h/\mu$
$Re_L$	Reynolds number based on a characteristic length = $\rho U L/\mu$
Si	silicon
SiC	silicon carbide
T	temperature
$T_{\text{amb}}$	ambient temperature surrounding the inverter
$T_D$	diode temperature

$T_f$	fluid temperature
$T_{\text{inlet}}$	temperature of the fluid domain at the inlet
$T_j$	junction temperature
$T_M$	MOSFET temperature
$T_{\text{max}}$	maximum temperature
$T_{\text{min}}$	minimum temperature
$T_s$	solid temperature
$T_{\infty}$	fluid temperature
$T_t$	time
$u$	velocity component
$\mathbf{u}$	velocity field vector
$\mathbf{u}'$	fluctuating component of the velocity vector
$u_{\tau}$	friction velocity
$U$	mean component of the velocity vector
$U_0$	normal inflow velocity
US06	US06 drive cycle
UTK	University of Tennessee Knoxville
$V$	voltage
$V_{\text{dc}}$	DC bus voltage
WBG	Wide Band Gap

## Units

A	Amperes
°C	degree Celsius
CFM	cubic feet per minute (actual volumetric flow rate)
J	joule
K	Kelvin
kg	kilogram
kW	kilowatt
m	meter
L	liter
mm	millimeter
Pa	Pascal
s	seconds
V	volts
W	watt

## Greek

$\Delta$	change
$\nabla$	gradient operator
$\delta_w$	wall offset
$\delta_w^+$	wall offset in viscous units
$\varepsilon$	dissipation rate of turbulent energy
$\mu$	dynamic viscosity
$\mu_T$	eddy viscosity
$\rho$	density

# Chapter 1. Introduction

An inverter is a specific example of a more general class of power electronics classified as converters. All converters consist of devices that generate heat. These solid-state devices require close temperature control for reliability, efficiency, and stability. Reliability and efficiency are inversely proportional to temperature. Thus cooling of these devices is critical to their performance, reliability, and stability. There are multiple ways of cooling such devices. Oak Ridge National Laboratory (ORNL) has proposed developing an air-cooled inverter that takes advantage of the higher operating temperatures of wide band gap (WBG) devices as compared to traditional silicon devices. Over the last two years, significant research progress has been made in determining the thermal performance of the proposed inverter. The design presented in this thesis is the result of several conceptual design iterations over the last year.

In order to determine the thermal performance of the design under consideration, finite element models were developed to simulate the physics of a forced convective heat transfer problem consisting of a three dimensional fully turbulent flow field. Finite element simulations were implemented in this study because they are significantly less expensive than building and testing prototypes. They also reduce the time required to get from a conceptual design to a feasible design.

The proposed rectangular inverter is designed with a specific application in mind, namely to be used in hybrid electric vehicles (HEVs). This application presents several additional design considerations that will be discussed later.

## 1.1 Motivation for Air-Cooling

Air-cooling of an inverter is significantly more difficult than the traditional methods that involve liquid-cooling. Air has a much lower thermal conductivity than most liquids, and as a result air-cooling systems typically have lower heat transfer coefficients than liquid-cooling systems. The motivation for air-cooling is a savings in cost and weight.

Liquid-cooling systems are more complicated than air-cooling systems primarily because they operate on a closed loop, i.e., the coolant is recycled through the system. This closed loop operation requires a separate heat exchanger to transfer the heat to the atmosphere.

On the other hand, air-cooling systems operate on an open cycle. The coolant, ambient air is taken in from the surroundings. At the exit of the air-cooling system, the heated coolant is exhausted to the surroundings. This type of open cycle operation eliminates the need for a heat exchanger within the loop to reject the heat to the surroundings.

Choosing which of the two types of cooling systems to use depends on the specific application. Liquid cooled systems are generally capable of transferring more heat. If air-cooling a proposed inverter is determined to be not feasible due to excess temperatures, then a liquid cooling system will be investigated for feasibility.

However, the operational cost of a liquid cooled system is typically higher than air-cooled system. Since the inverter in this research project consists of WBG devices, which have high operating temperatures, air-cooling is considered the preferable method of cooling

the devices due to the cost savings. Furthermore, the only part of the air-cooling system that is likely to fail is the blower that is driving the air flow. Therefore, air-cooling systems have the advantage of an increase in reliability as well.

## **1.2 Objectives of this Study**

The primary objective of this study is to determine whether or not the proposed rectangular air-cooled WBG inverter is thermally feasible when subjected to heat sources that are given as a function of electrical input parameters and local junction temperatures of the devices. In order to establish that the proposed design is thermally feasible, the maximum temperature of the devices must not exceed 250 °C.

The second objective of this study is to substantially reduce the blower power requirements to provide sufficient cooling compared to a previous air-cooled inverter [1]. In order to lower the blower power requirements to cool the inverter, changes in the inverter geometry were made to substantially reduce the convective acceleration term associated with the significant change in cross sectional area of the fluid domain.

The third objective of this study is to simulate the transient performance of the proposed inverter subject to the United States Environmental Protection Agency (EPA) US06 drive cycle as the time dependent input for current [2]. The transient simulations were studied over a range of input parameters to gain insight into the thermal performance of the inverter in real world operating conditions.

### **1.3 Overall Design Considerations**

Because the proposed inverter is to be implemented in HEVs, there are several additional considerations that led to the final design. One of the most important considerations of any automotive component design is cost. A lot of effort was made throughout this research and development project to lower cost wherever possible. Due to the cyclic loading nature of automotive components, the coefficient of thermal expansion of materials within the inverter should be the same or very close to each other to prevent thermally induced stresses. Another important consideration to any automotive component design is the overall volume of the component. In order to ensure the power density (kW/L) of the proposed air-cooled inverter is competitive with alternative liquid-cooled designs, the total volume of the entire inverter package should not exceed 5 L for an inverter rated at 55 kW. Manufacturability, maintenance, and reliability were all considerations that went into the final design as well.



## **Chapter 2. Literature Review**

The literature review contains two sections. The first section gives an overview of the inverter basics, various methods of cooling electrical devices, and what has been done by others in the electronic cooling community. The second section highlights the work that has been done by a team of researchers at the University of Tennessee Knoxville (UTK) on determining the thermal performance of an air-cooled WBG inverter prior to the start of this research project.

### **2.1 Inverter Basics**

An inverter is a power electronic device that converts a DC voltage source to an AC current source. It is implemented in HEV to convert the DC voltage from a battery, or any other electrical energy storage system like a capacitor, and convert it to a three phase AC current that is fed to the electric motor powering the wheels. An electrical schematic of a voltage source inverter is given in Figure 2.1. The capacitor on the left hand side of Figure 2.1 filters out any voltage ripple that may be present in the DC signal.

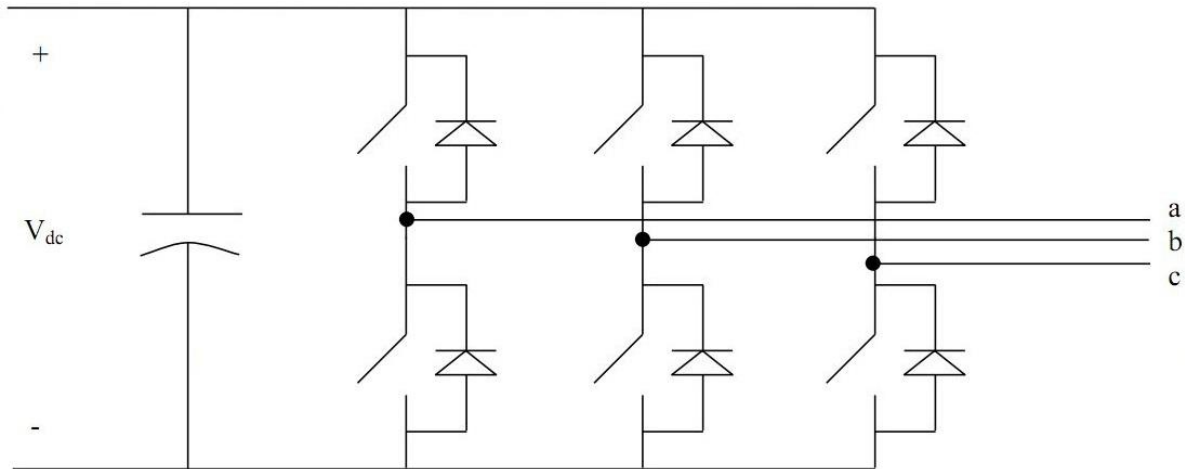


Figure 2.1 Electrical schematic of a voltage source inverter [3]

The DC current enters the inverter, and is converted to an AC current by a series of diodes and transistors. These solid state devices switch the current on and off at a high frequency to achieve the desired waveform, and in the process, dissipate heat within each device. It is for this reason that all inverters must be cooled. The efficiency, stability, and life of the devices depend on keeping the device temperatures below their maximum operating temperatures.

Advances in semiconductor technology have led to increases in heat load and power density of inverters. Traditionally, air-cooling is not used for inverters due to the high heat load of the inverter, and the low heat transfer coefficient of air. Over the years, various methods of liquid cooling, evaporative cooling, spray cooling, and cold plates have been implemented in such applications [4]. The method of cooling that is used depends on the specific application.

The attempts at air-cooling thus far have all been for low-power rated inverters. Gradingier and Liu [5] have studied the feasibility of air-cooling silicon insulated-gate bipolar

transistors (IGBTs) and diodes through CFD modeling. Their simulations consisted of a constant heat generation rate. The convective boundary condition was a turbulent correlation for an average heat transfer coefficient. For the geometry of the design under consideration, a correlation that can accurately describe the average heat transfer coefficient does not exist.

To this author's knowledge, there is no published literature on the feasibility of air-cooling an inverter consisting of WGB device through CFD simulations with variable heat generation equations. Furthermore, the fluid flow through the inverter has been simulated by solving the mass and momentum transport equations. This allowed the local heat transfer coefficient in the energy transport simulation to vary with position by coupling the mass and momentum transport simulations with the general viscous energy transport equation. This approach captures a lot more relevant physics than using a correlation for the convection boundary conditions.

## 2.2 State of the Current Research

Over the course of the fiscal year (FY) 2009 [1], a research project was undertaken at UTK that established the thermal feasibility and performance of an air-cooled WBG inverter. In this configuration, air flows radially inward over the cards, makes a 90° turn, and leaves the inverter through the center of the circular capacitor located at the bottom of the inverter. The FY 2009 design can be seen in Figures 2.2 and 2.3. The results from finite element simulations of the inverter can be seen in Figures 2.4 through 2.7. A summary of the performance results of that study are shown in Table 2.1 where the volumetric flow rate and the heat generation values are for a single unit cell and the ideal blower power is for the entire inverter.

Table 2.1 Results from finite element simulations of the air-cooled inverter from the FY 2009 study with  $Q = 60$  CFM,  $\dot{E}_{Gen} = 192$  W, and  $T_{amb} = T_{inlet} = 50$  °C

Performance Parameters	Units	Results of the First Design Without Fins	Results of the Final Design With Fins
$T_j$ max	°C	380	200
Pressure Drop	Pa	3400	3500
Ideal Blower Power	W	940	970

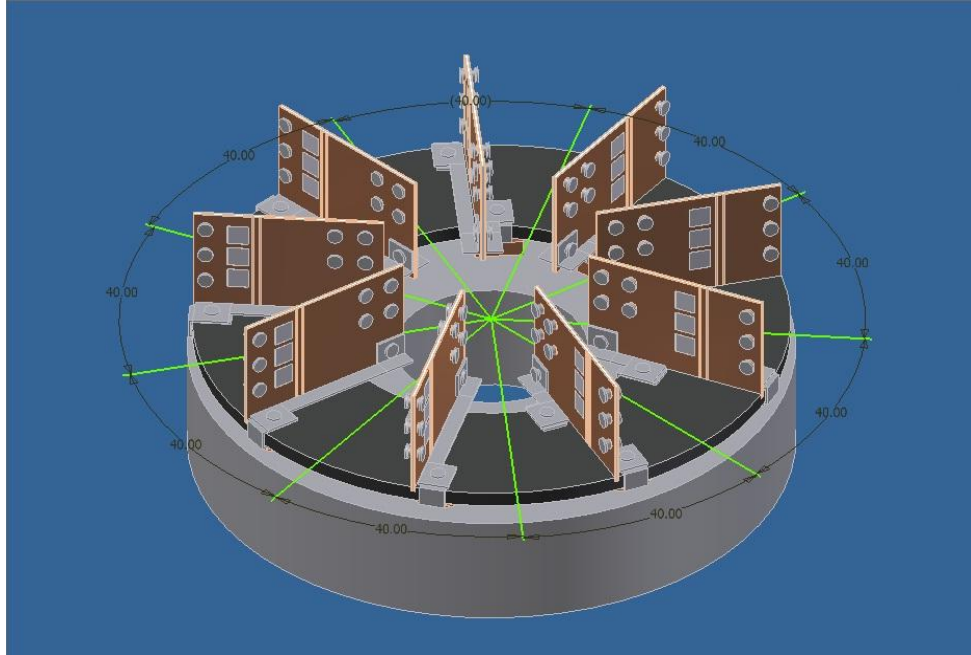


Figure 2.2 Isometric view of the FY 2009 inverter without fins [1]

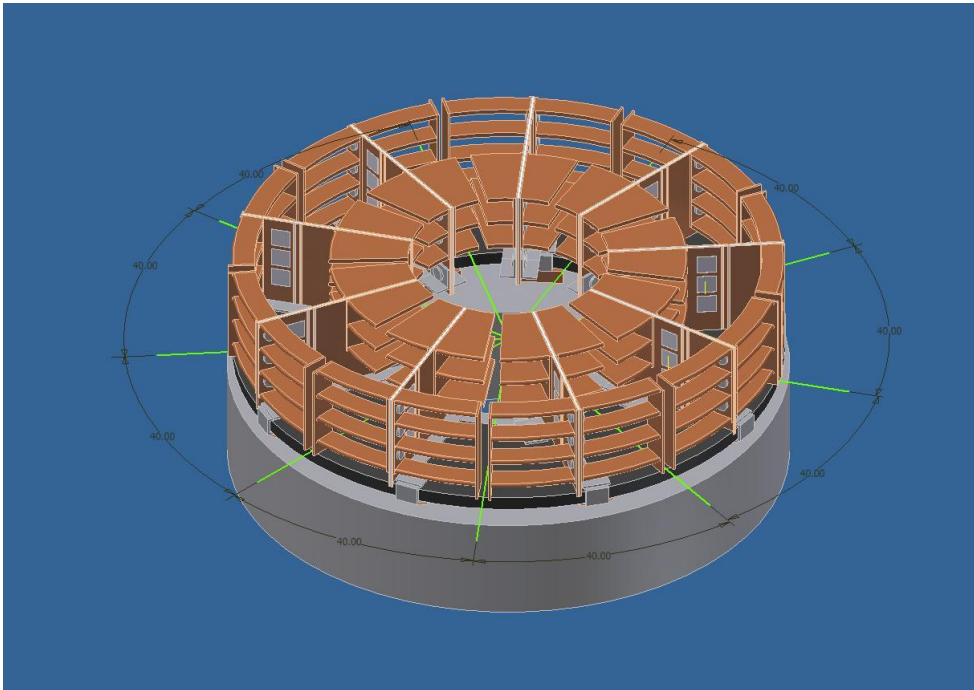


Figure 2.3 Isometric view of the FY 2009 inverter with fins [1]

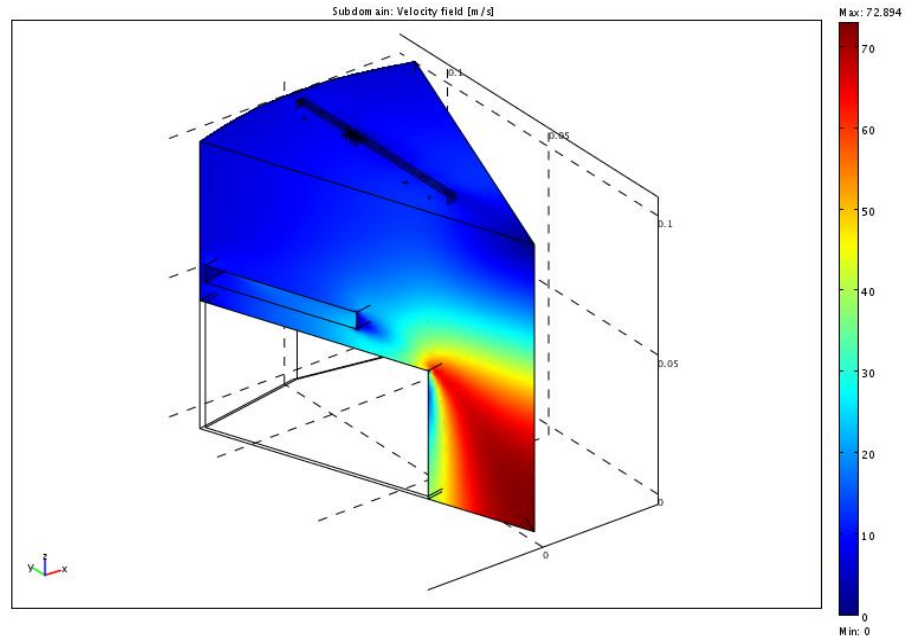


Figure 2.4 Fluid domain velocity field of the FY 2009 inverter without fins [1]  
with  $Q = 60$  CFM

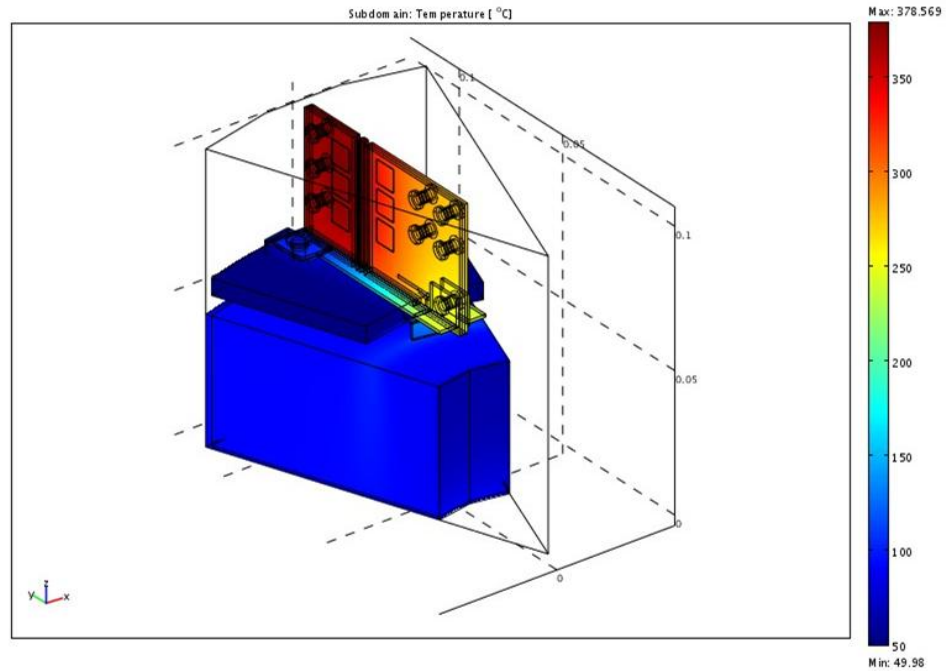


Figure 2.5 Solid domain temperature distribution of the FY 2009 inverter without fins [1]  
with  $Q = 60$  CFM,  $\dot{E}_{Gen} = 192$  W, and  $T_{amb} = T_{inlet} = 50$  °C

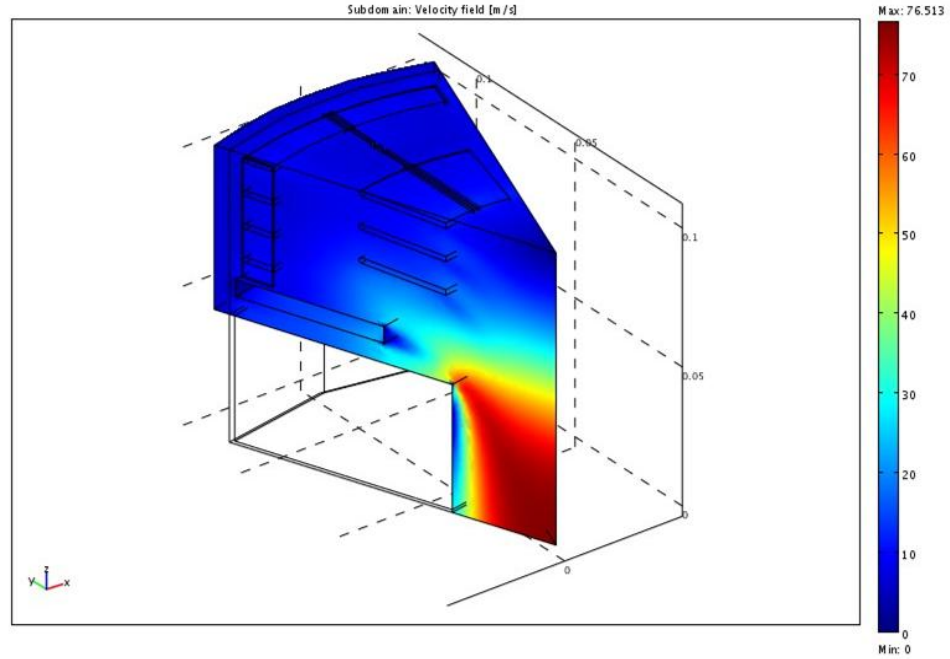


Figure 2.6 Fluid domain velocity field of the FY 2009 inverter with fins [1]  
with  $Q = 60$  CFM

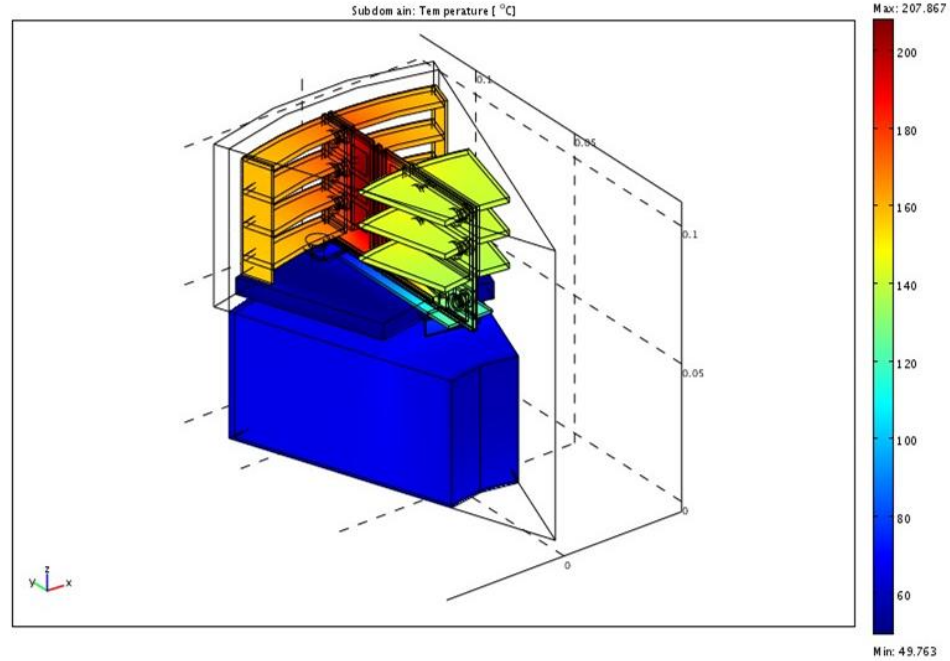


Figure 2.7 Solid domain temperature distribution of the FY 2009 inverter with fins [1]  
with  $Q = 60$  CFM,  $\dot{E}_{Gen} = 192$  W, and  $T_{amb} = T_{inlet} = 50$  °C

There are several issues with the performance of this design that warranted further research. First, the heat sources in the simulations of the FY 2009 project were specified as a constant volumetric heat generation rate. The rate of heat generation was specified to 24 W for each diode, while the rate of heat generation was specified to 36 W for each IGBT. Since the design consists of 3 diodes and 3 IGBTs, the total heat generation in the simulations was 192 W per unit cell.

This is not a very realistic simulation, as the heat sources will be dependent on the electrical power inputs, and on the local junction temperatures of the devices. The first major contribution of the research that is presented in this thesis is to simulate the thermal performance of an air-cooled inverter with heat sources that are given as a function of electrical input parameters and local junction temperatures of the devices.

The second performance issue with this design was the blower power required to provide sufficient cooling was deemed too high. It was concluded from the FY 2009 project that the dominant contributor to the overall pressure drop across the inverter was the convective acceleration associated with the significant change in cross sectional area of the fluid domain. In order to lower the blower power requirements to cool the inverter, the convective acceleration term associated with the change in cross sectional area of the fluid domain must be substantially reduced.

The third issue with the FY 2009 project was all of the simulations were solved in steady state mode. Although this type of simulation provides conservative results (i.e., higher maximum junction temperatures), it does not give insight into a realistic operating



condition of the inverter where the power of the inverter is changing with time. Therefore, it is desired to study the performance of an air-cooled simulation in transient mode.

The fourth issue of the FY 2009 design was that it was deemed unrealistic for manufacturing. Further effort must be taken to develop a simpler design that is capable of mass production.

The fifth and final issue of the FY 2009 project was that the complicated fins structure would be effectively acting like antennas. This would cause some electromagnetic interference (EMI) that is highly undesirable. New fin designs must be developed in order to reduce the fins contribution to EMI.

## Chapter 3. Problem Statement and Boundary Conditions

Specific details of the feasibility study taken place over the FY 2010 are now discussed. In order to explain what the simulations solved for and how they arrived at the solution, a brief introduction to forced convection heat transfer and turbulence will be given. The governing equations, boundary conditions, and input parameters used in the simulations will then be discussed. This section will conclude with a “bird’s eye view” of exactly how the simulations arrived at the results.

### 3.1 The Problem of Forced Convection Heat Transfer

Energy can be transferred from a system to its surrounding in the form of heat. It is well known that there are three modes of heat transfer: conduction, convection, and radiation. The mode of convection heat transfer consists of random molecular motion (diffusion) and energy transport due to bulk fluid motion (advection). Typically, convection occurs between a solid surface and a moving fluid. The rate equation for convection is given by Newton's Law of Cooling as

$$q'' = h(T_s - T_\infty) \quad (3.1)$$

where  $h$  is the convection heat transfer coefficient. The heat transfer coefficient is highly dependent on the local motion of the fluid, the geometry, and the thermal conductivity of the fluid.

There are two ways of solving this combined solid-fluid-thermal interaction. The first method involves solving the energy equation (diffusion) in the solid domain by specifying an average heat transfer coefficient and ambient temperature in the convection boundary condition on the solid surfaces exposed to a fluid. In this approach, the fluid domain is not directly modeled. This method was used early on in the FY 2009 study. This method is computationally efficient and is good for a first estimate of the temperature distribution. The shortcoming of this method is that it does not capture all of the relevant physics in the problem; such as the fact that the heat transfer coefficient is not constant, but rather varies with position. As previously stated, the heat transfer coefficient is highly dependent on the local velocities of the fluid. In order to simulate all of the relevant physics in the problem, the second method must be used.

The second method requires a simulation of the fluid motion by solving the mass and momentum transport equations in the fluid domain. The velocity field that is solved for in this simulation can then be used in the general viscous heat equation (advection and diffusion) to solve for the temperature distribution in both the solid and fluid domains. The second method is the most realistic simulation of the two and was chosen for this research project.

## 3.2 Problem Solving Methodology

Throughout this project, we assumed the flow to be incompressible with constant properties. It is well documented in the literature that the energy transport equation is uncoupled from the mass and momentum transport equations for an incompressible flow with constant viscosity [6]. This is a very useful characteristic of the governing equations, and is particularly useful in parametric studies. Therefore, the energy transport equation was solved separately from the mass and momentum transport equations. Furthermore, the general viscous energy equation contains advection terms that depend on the local fluid motion. Therefore, the problem solving methodology used throughout this research project can be summarized by the following two steps: first, solve the mass and momentum transport equations for the velocity field using a relative tolerance of  $1 * 10^{-6}$ ; and second, solve the energy transport equation for the temperature distribution using a relative tolerance of  $1 * 10^{-3}$  in both the solid and fluid domains subject to various input parameters. All numerical simulations presented in this thesis were developed using COMSOL Multi-physics software version 3.5a.

### 3.3 A Premise on Turbulence

It is well known throughout the engineering community that many real world flows are turbulent. Turbulence is a flow regime of the flow field. The dimensionless parameter that governs whether the flow field is in this regime is given by the Reynolds number expressed as

$$Re_L = \frac{\rho u L}{\mu} \quad (3.2)$$

The Reynolds number represents the ratio between the inertial and viscous forces acting on a fluid element. If the Reynolds number is sufficiently large, the inertial terms dominate and the flow field becomes turbulent. This regime is characterized by a highly chaotic and fluctuating fluid motion. The fluctuations in velocity, pressure, and temperature vary in space and time. The motion of a turbulent flow field is so complex that analytical solutions do not exist even for the simplest flow fields.

There is an advantage to a turbulent flow field. Turbulence significantly enhances the diffusion of mass, momentum, and energy due to the strong mixing action associated with the flow field. This results in enhanced heat transfer. Although a forced turbulent flow field will require more blower power to transport the fluid when compared to a forced laminar flow field, the enhancement in heat transfer makes a turbulent flow field desirable in this project. Throughout this project, the density and viscosity of the fluid were assumed to be constant and were taken at 300 K. It is important to demonstrate that for all flow rates in this study, the flow is indeed turbulent. This procedure is described in detail in the next section.

### 3.4 Reynolds Number Calculations

For the design under consideration, the characteristic length that should be used in Eq. (3.2) to calculate the Reynolds number for a given flow rate is the hydraulic diameter. The range of flow rates that was studied in this project was  $Q = 30, 40, 50, 60, 70$ , and  $80$  CFM. The density and viscosity were assumed to be constant in all simulations and were evaluated at  $300$  K. The Reynolds number for a given flow rate based on the inlet conditions are calculated as shown below. The range of Reynolds numbers based on inlet conditions encountered in this study are shown in Table 3.1.

$$A = \text{cross sectional area of the inlet} = 0.004188 \text{ m}^2$$

$$P = \text{perimeter of the inlet} = 0.31628 \text{ m}$$

$$D_h = \text{hydraulic diameter of the inlet} = \frac{4A}{P} = 0.052968 \text{ m}$$

Table 3.1 Range of Reynolds numbers encountered in this study based on inlet conditions

$Q$ , CFM	30	40	50	60	70	80
$U$ , m/s	3.4	4.5	5.6	6.7	7.9	9
$Re_{D_h}$	11195	14926	18658	22390	26121	29853

However, the air flows through a narrow channel between the fins. The details of the design under consideration will be discussed in Chapter 4. The narrow channel will have a significantly smaller hydraulic diameter; and therefore, a smaller Reynolds number. In order to ensure the fluid domain is fully turbulent, the Reynolds number should be sufficiently large everywhere in the fluid domain. The Reynolds number for a given flow rate based on the channel conditions are calculated as shown below, and the corresponding range of Reynolds numbers encountered in this study are shown in Table 3.2. We know from the work of Osborne Reynolds (1883) that transition to turbulence typically occurs at  $Re_D \approx 2000$  [6]. The accepted critical Reynolds number for engineering purposes is taken to be  $Re_D=2300$  for an internal flow [7]. Therefore, all flow rates considered in this study will produce a fully turbulent flow field everywhere in the fluid domain.

$$A = \text{cross sectional area of the channel} = 0.00003 \text{ m}^2$$

$$P = \text{perimeter of the channel} = 0.034 \text{ m}$$

$$D_h = \text{hydraulic diameter of the channel} = \frac{4A}{P} = 0.003529 \text{ m}$$

Table 3.2 Range of Reynolds numbers encountered in this study based on channel conditions

$Q$ , CFM	30	40	50	60	70	80
$U$ , m/s	12.1	16.1	20.1	24.1	28.1	32.1
$Re_{D_h}$	2670	3560	4450	5340	6230	7120

### 3.5 Steady State Mass and Momentum Transport Simulations

In the early 1500's, the equation for the conservation of mass for a one-dimensional incompressible fluid flow was correctly deduced by Leonardo Da Vinci [6]. The general form of this equation is now known as the continuity equation, and the steady incompressible form is given by

$$\nabla \cdot \mathbf{u} = 0 \quad (3.3)$$

In 1845, Sir George Stokes published the form of the governing equations for the transport of momentum of a viscous fluid that is used today [6]. These equations are known as the Navier-Stokes equations and the steady incompressible form is given by

$$\rho(\mathbf{u} \cdot \nabla)\mathbf{u} = -\nabla p + \mu \nabla^2 \mathbf{u} + \mathbf{F} \quad (3.4)$$

The continuity and Navier-Stokes equations form the fundamental basis for fluid mechanics. The unsteady form of these equations can be used for the simulation of turbulent flow fields. This method is referred to as direct numerical simulation (DNS). However, the computational resources (cpu time, memory, etc.) required to complete a DNS is far outside of the scope of this project.

An alternative method for simulating a steady turbulent flow field involves applying a time averaging technique to the general governing equations. The flow is separated into a mean and fluctuating part as shown in Figure 3.1. Substituting the mean and fluctuating components of velocity and pressure into the Navier-Stokes equations, assuming the fluctuations to be random, and integrating over a sufficiently large interval of time, the



general governing equations simplify to the time-averaged governing equations for mass and momentum transport of the turbulent flow field [6]. Solving for the mean flow usually provides sufficient information about the flow field for engineering purposes. This idea was first proposed by Osborne Reynolds in 1895 [6], and the averaged equations are named in his honor as the Reynolds Averaged Navier-Stokes equations (RANS). The RANS equations are listed in COMSOL literature [8] in the format given as

$$\nabla \cdot \mathbf{U} = 0 \quad (3.5)$$

$$\rho(\mathbf{U} \cdot \nabla)\mathbf{U} + \rho \nabla \cdot \overline{(\mathbf{u}' * \mathbf{u}')} = -\nabla \bar{p} + \mu \nabla^2 \mathbf{U} + \mathbf{F} \quad (3.6)$$

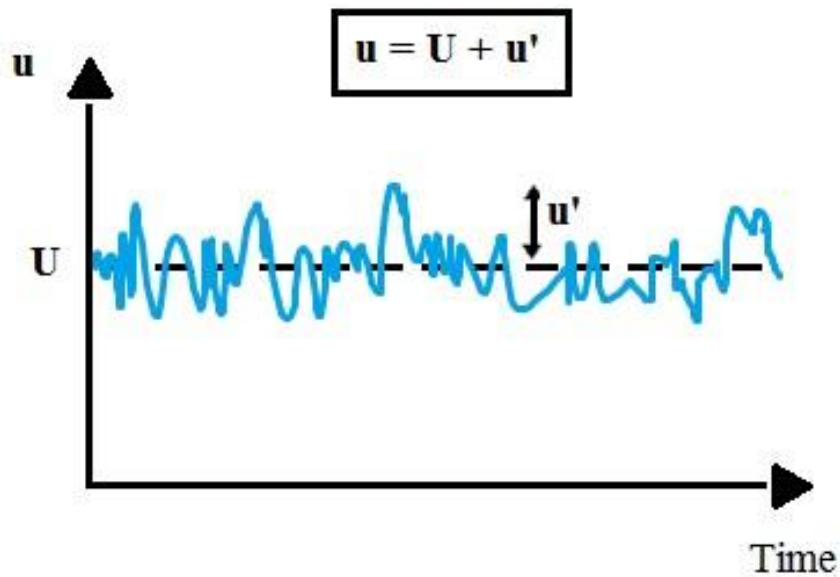


Figure 3.1 Schematic illustrating the separation of the velocity field into a mean and a fluctuating component

In Eq. (3.5) and (3.6),  $\mathbf{U}$  is the mean velocity,  $\bar{p}$  is the mean pressure of the flow field,  $\mathbf{F}$  is the body force, and  $*$  is the outer vector product. The second term on the left hand side of the RANS equation is known as the Reynolds stress tensor. The term represents the interaction between the mean and fluctuating components of the velocity field and it consist of 9 additional unknowns, 6 of which are independent of one another. At this point we have 4 equations and 10 independent unknowns. This is known as the closure problem of turbulence.

In order to solve this system of equations, additional relationships should be developed to relate the fluctuating components of the velocity field to the mean components of the velocity field. The most common way to do this is to assume turbulence to be purely diffusive in nature. This leads to the idea of eddy viscosity which is the basis of the  $k$ - $\epsilon$  closure relationship. The  $k$ - $\epsilon$  closure model assumes that the turbulent kinetic energy production,  $k$ , is equal to the dissipation rate of turbulent energy,  $\epsilon$ . The  $k$ - $\epsilon$  closure model is by far the most used closure relationship in numerical simulations of turbulent flow fields in industry. This model introduces two additional transport equations and two additional unknowns to the RANS equations. We now have a system of 6 equations and 6 unknowns to solve in the numerical simulation of the turbulent flow field [8]. These equations are given as Eq. (3.7) through Eq. (3.10). The constants in the following equations are determined from experimental data and are given in Table 3.3. In most engineering applications, the limited accuracy of the  $k$ - $\epsilon$  closure model is a reasonable trade off for the required computational cost to solve these equations.

The continuity equation is given by

$$\nabla \cdot \mathbf{U} = 0 \quad (3.7)$$

the momentum equations are given by

$$\rho(\mathbf{U} \cdot \nabla)\mathbf{U} = \nabla \cdot [-p\mathbf{I} + (\mu + \mu_T)(\nabla\mathbf{U} + (\nabla\mathbf{U})^T)] + \mathbf{F} \quad (3.8)$$

the equation governing the transport of turbulent kinetic energy is given by

$$\rho\mathbf{U} \cdot \nabla k = \nabla \cdot \left[ \left( \mu + \frac{\mu_T}{\sigma_k} \right) \nabla k \right] + \mu_T P(\mathbf{U}) - \rho\varepsilon \quad (3.9)$$

the equation governing the dissipation rate of turbulent energy is given by

$$\rho\mathbf{U} \cdot \nabla \varepsilon = \nabla \cdot \left[ \left( \mu + \frac{\mu_T}{\sigma_\varepsilon} \right) \nabla \varepsilon \right] + \left( \frac{C_{\varepsilon 1} \varepsilon}{k} \right) [\mu_T P(\mathbf{U})] - \frac{C_{\varepsilon 2} \rho \varepsilon^2}{k} \quad (3.10)$$

where:  $P(\mathbf{U}) = \nabla \mathbf{U} : (\nabla \mathbf{U} + (\nabla \mathbf{U})^T)$ .

Eddy viscosity is defined as

$$\mu_T = \rho C_\mu \frac{k^2}{\varepsilon} \quad (3.11)$$

Table 3.3 Constants used in the  $k$ - $\varepsilon$  closure model [8]

Constant	Value
$C_\mu$	0.09
$C_{\varepsilon 1}$	1.44
$C_{\varepsilon 2}$	1.92
$\sigma_k$	1.0
$\sigma_\varepsilon$	1.3

The boundary conditions used in the fluid flow simulations are now discussed. The boundary condition applied to all solid surfaces exposed to the fluid is the logarithmic wall function [8]. In this boundary condition, an empirical relation between the value of velocity and the wall friction replaces the thin boundary layer near the wall and is defined by

$$U = \frac{u_\tau}{K} \ln \left( \frac{\delta_w}{l^*} \right) + C^+ \quad (3.12)$$

This approach assumes the computational domain begins a distance,  $\delta_w$ , from the wall. It also assumes an impermeable wall, which can be described by

$$\mathbf{n} \cdot \mathbf{U} = 0 \quad (3.13)$$

In Eq. (3.12),  $U$  is the velocity perpendicular to the wall, and  $u_\tau$  is the friction velocity defined by

$$u_\tau = \sqrt{\frac{\tau_w}{\rho}} \quad (3.14)$$

$K$  is the von Karman constant and is equal to 0.42 in these simulations [8].  $C^+$  is a constant accounting for the wall roughness, and is equal to 5.5 in these simulations [8].  $l^*$  is the viscous length scale and is defined by

$$l^* = \frac{\mu}{\rho u_\tau} \quad (3.15)$$

while  $\delta_w$ , or its equivalent in viscous units  $\delta_w^+$ , must be specified in these simulation. The logarithmic wall functions are formally valid for  $\delta_w^+$  between 30 and 100, with 30 being the

most accurate simulation. Throughout this study,  $\delta_w^+$  was specified to be 30. The relationship between  $\delta_w^+$  and  $\delta_w$  is given by

$$\delta^+ = \frac{\delta_w}{l^*} \quad (3.16)$$

The boundary conditions for  $k$  and  $\varepsilon$  on the walls are derived from the assumption that turbulent production equals the dissipation as described in section 3.3. The boundary conditions for  $k$  and  $\varepsilon$  on the walls are given by

$$\nabla k \cdot \mathbf{n} = 0 \quad (3.17)$$

$$\varepsilon = \frac{\rho C_\mu^{3/4} k^{3/2}}{\kappa \delta_w} \quad (3.18)$$

respectively. In order to simulate a turbulent flow field, a turbulent length scale and a turbulent intensity is specified at the inlet of the fluid domain. The boundary condition for the inlet is given by

$$\mathbf{U} = -U_0 \mathbf{n} \quad (3.19)$$

Here,  $U_0$  is the normal inflow velocity. In addition to specifying the velocity at the inlet, the turbulent length scale and the turbulent intensity are specified by

$$k = \frac{3}{2} (|\mathbf{U}| I_T)^2 \quad (3.20)$$

$$\varepsilon = C_\mu^{3/4} \frac{k^{3/2}}{L_T} \quad (3.21)$$

Since we are only interested in the pressure drop across the fluid domain, and not the values of absolute pressure in the flow domain, the boundary condition at the exit of the flow domain was specified to be a gauge pressure equal to zero. In addition to specifying the gauge pressure equal to zero on the exit boundary, the boundary conditions for  $k$  and  $\varepsilon$  are specified by

$$\mathbf{n} \cdot \nabla k = 0 \quad (3.22)$$

$$\mathbf{n} \cdot \nabla \varepsilon = 0 \quad (3.23)$$

The fourth and last type of boundary condition that must be specified in these simulations is a symmetry boundary condition on the geometric planes of symmetry. The boundary condition sets zero mass flow across the symmetry boundaries. This is given by

$$\mathbf{n} \cdot \mathbf{U} = 0 \quad (3.24)$$

In addition to specifying the normal velocity equal to zero, the total normal flux of the turbulent quantities must also be zero. The boundary conditions for  $k$  and  $\varepsilon$  are specified on the symmetry boundaries by

$$\mathbf{n} \cdot \left( \left( \mu + \frac{\mu_T}{\sigma_k} \right) \nabla k - \rho \mathbf{U} k \right) = 0 \quad (3.25)$$

$$\mathbf{n} \cdot \left( \left( \mu + \frac{\mu_T}{\sigma_\varepsilon} \right) \nabla \varepsilon - \rho \mathbf{U} \varepsilon \right) = 0 \quad (3.26)$$

### 3.6 Steady State Energy Transport Simulations

Energy transport in a solid is by diffusion, while energy transport in a fluid is by diffusion and advection. Therefore, the governing equations for energy transport will be different in the solid and fluid domains.

The governing equation for the transport of energy in the solid domain is given as

$$\rho C_p \frac{\partial T}{\partial t} = \nabla \cdot (k \nabla T) + q''' \quad (3.27)$$

Since the simulation is solving for the steady state temperature distribution, the left hand side of Eq. (3.12) is set to zero. The first term on the right hand side of Eq. (3.12) is the diffusion term, and the second term on the right hand side of Eq. (3.12) is the heat source term. The heat source term for the electrical devices is given as a function of voltage, current, switching frequency, and local junction temperature. This will be discussed in Section 3.7.

The boundary condition applied to all solid surfaces exposed to the fluid is called the thermal wall function. It assumes the heat flux across the solid-fluid interface is proportional to the temperature difference between the wall and the fluid just outside the hydrodynamic boundary layer [8]. These boundary conditions are given by

$$\mathbf{n} \cdot (-k \nabla T_s) = \frac{\rho C_p C_\mu^{1/4} k_w^{1/2} (T_s - T)}{T^+} \quad (3.28)$$

$$T^+ = \frac{Pr \delta_w \rho C_\mu^{1/4} k^{1/2}}{\mu} \quad (3.29)$$

There are several boundaries in the simulations that are specified to be insulated. This boundary condition states that the normal conductive heat flux across that boundary is equal to zero. This is expressed as

$$\mathbf{n} \cdot (-k \nabla T_s) = 0 \quad (3.30)$$

The external solid boundaries were given a convection boundary condition given by

$$\mathbf{n} \cdot (-k \nabla T_s) = \bar{h}(T_s - T_{amb}) \quad (3.31)$$

In this boundary condition, an average heat transfer coefficient of  $10 \frac{W}{m^2 K}$  and an average ambient temperature were specified. The average heat transfer coefficient of  $10 \frac{W}{m^2 K}$  was chosen because it is within the typical range of heat transfer coefficients encountered in natural convection [9]. The ambient temperature is an input parameter that was varied in the parametric study.

The governing equation for the transport of energy in the fluid domain is given by

$$\rho C_p \mathbf{U} \cdot \nabla T + \rho C_p \frac{\partial T}{\partial t} = \nabla \cdot ((k + k_T) \nabla T) \quad (3.32)$$

The first term on the left hand side of Eq. (3.32) is the advection term. It contains the local mean velocities that were determined from the fluid flow simulation. For the steady state simulations, the second term on the left hand side of Eq. (3.32) is equal to zero. The first term on the right hand side of Eq. (3.32) is the diffusion term.

The boundary condition applied to the fluid boundaries in contact with the solids is the same thermal wall function used on the solid boundaries exposed to the fluid. This is a



simple statement of the first law of thermodynamics, and specifies the heat flux is continuous. In other words, the normal conductive heat flux out of the solid is equal to the normal conductive heat flux into the fluid on these boundaries.

The boundary condition used on the inlet of the fluid domain is given as a constant uniform temperature on the boundary. The inlet temperature of the fluid domain is an input parameter that is varied in the parametric study.

The boundary condition used on the exit of the fluid domain states that the normal conductive heat flux into the fluid domain is equal to zero. This is given by

$$\mathbf{n} \cdot (-k \nabla T_f) = 0 \quad (3.33)$$

The boundary condition on the symmetry planes of the fluid domain is a little bit different than the typical adiabatic boundary condition due to the turbulent flow field. The boundary condition specified on the planes of symmetry corresponding to fluid boundaries is given by

$$\mathbf{n} \cdot (-(k + k_T) \nabla T_f) = 0 \quad (3.34)$$

where  $k_T$  is the eddy conductivity and is a property of the flow field.

### 3.7 Heat Generation Equations

The inverter used in this research project consists of silicon carbide metal oxide semiconductor field effect transistors (MOSFETs) and diodes. An experiment was performed at ORNL to determine the efficiency of these devices as a function of voltage, current, switching frequency, and junction temperature. Equations were developed from the experimental data, and were used as the input for the volumetric heat generation equations in the simulations. The equations that were used were provided by Chinthavali [10] of ORNL, and are given in Eq. (3.35) through (3.38). In these equations,  $P_{cond}$  and  $P_{swit}$  are in W,  $T$  is in °C,  $f_{sw}$  is in Hz,  $I$  is in A, and  $V$  is in V. The constants used in Eq. (3.35) through (3.38) are given in Table 3.4.

#### MOSFET:

$$P_{cond} = I^2(a_1T + a_2) \times 2 \quad (3.35)$$

$$P_{swit} = f_{sw}(b_1T + b_2) \left( \frac{I}{62.5A} \right) \left( \frac{V}{600V} \right) \quad (3.36)$$

#### DIODE:

$$P_{cond} = I^2(c_1T^2 + c_2T + c_3) \times 2 + I(d_1T + d_2) \quad (3.37)$$

$$P_{swit} = f_{sw}(e_1T + e_2) \left( \frac{I}{62.5A} \right) \left( \frac{V}{600V} \right) \quad (3.38)$$

Table 3.4 Constants used in the heat generation equations [10]

Constant	Value	Units
a1	$2 * 10^{-5}$	$\frac{W}{A^2 * ^\circ C}$
a2	0.0132	$\frac{W}{A^2}$
b1	$4 * 10^{-6}$	$\frac{W}{Hz * ^\circ C}$
b2	0.0038	$\frac{W}{Hz}$
c1	$3 * 10^{-7}$	$\frac{W}{A^2 * ^\circ C^2}$
c2	$2 * 10^{-5}$	$\frac{W}{A^2 * ^\circ C}$
c3	0.0084	$\frac{W}{A^2}$
d1	-0.0011	$\frac{W}{A * ^\circ C}$
d2	0.909	$\frac{W}{A}$
e1	$4 * 10^{-5}$	$\frac{W}{Hz * ^\circ C}$
e2	0.0011	$\frac{W}{Hz}$

A plot of the heat generation equations is provided in Figure 3.2. The data points in these plots are from the experiment. The solid and dashed lines represent the curve fits of the data. The total losses of the electrical devices are a sum of the conduction losses and the switching losses. As can be seen in Figure 3.2, the conduction losses dominate over the switching losses. Since the conduction losses depend on the square of current, an effort was made in designing the inverter package to reduce the current per device by adding more devices. This would decrease the heat load per device, spread the heat load over a larger area, and provide additional space for fins. There will be more detail on this in Chapter 4.

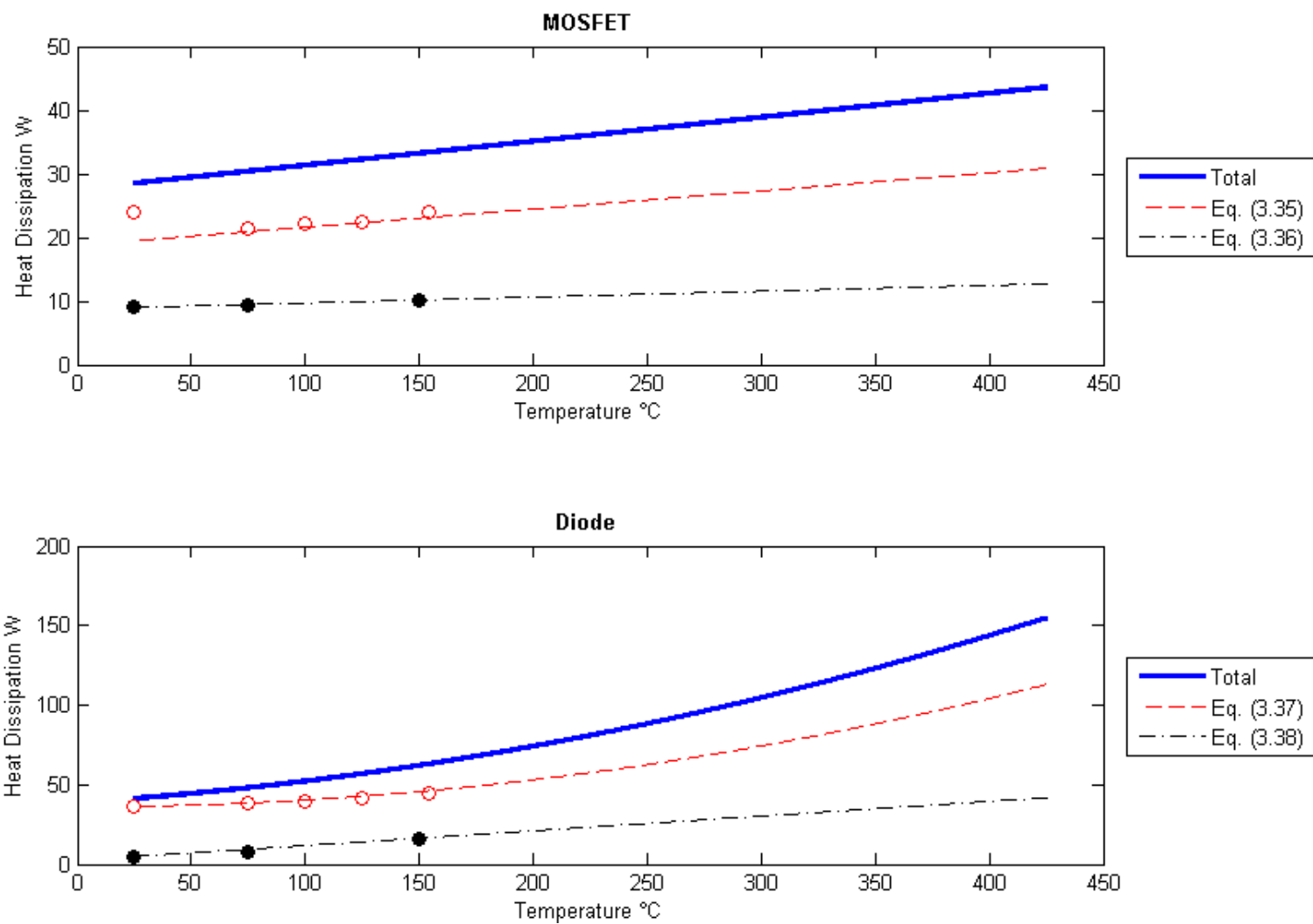


Figure 3.2 Plot of the heat generation equations with  $V = 650$  V,  $I = 240$  A,  $f_{sw} = 10$  kHz [10]

### **3.8 Transient Energy Transport Simulations**

The governing equations and boundary conditions for the transient simulations of energy transport are the same as the steady state simulations except that the unsteady term is not zero. The current input into the heat generation equations is now a function of time. Since the heat generation term varies with time, the temperature distribution will also vary with time.

As previously stated, the input for current into the heat generation equations in the transient simulations is given as a function of time. This function was deduced from the EPA US 06 drive cycle [2] for the specific design presented here. The US 06 drive cycle was chosen because it is the most aggressive and demanding of the three most common drive cycles used in the US. The function for current that was used in the heat generation equations of the transient simulations is given in Figure 3.3.

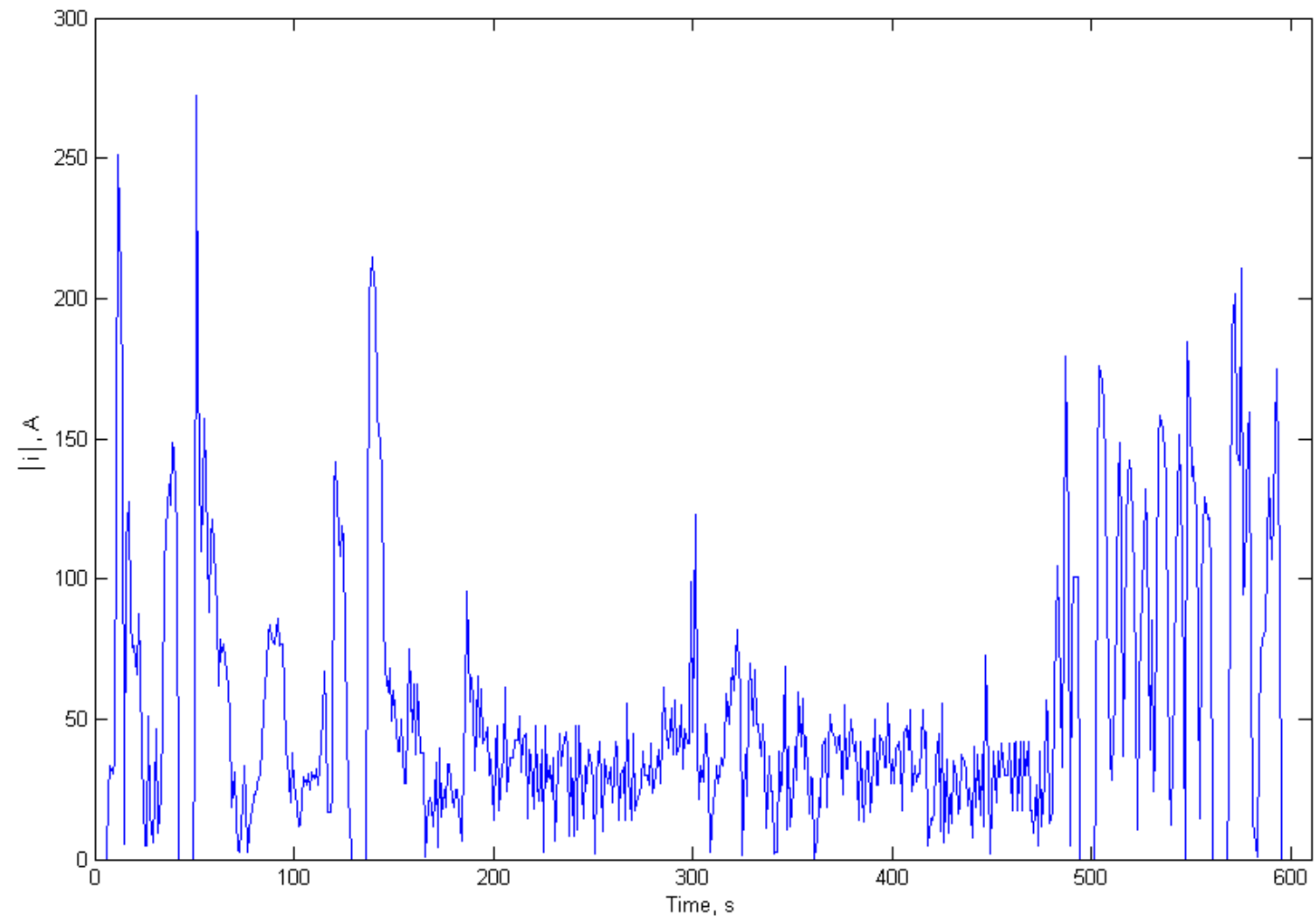


Figure 3.3 Input current for the transient simulations

### 3.9 Input Parameters for the Simulations

The range of input parameters, fluid properties, and material properties used in the simulations will now be discussed. All properties were assumed constant in the simulations.

The steady state velocity simulations were solved over the following range of volumetric flow rates:

$$Q = 30, 40, 50, 60, 70, 80 \text{ CFM}$$

The steady state simulations of the energy equation were solved for the following input parameters:

$$i = 240 \text{ A}$$

$$V = 650 \text{ V}$$

$$f_{sw} = 10 \text{ kHz}$$

$$Q = 40, 50, 60 \text{ CFM}$$

$$T_{inlet} = T_{amb} = 50, 55, 60, 65, 70, 75, 80, 85 \text{ }^{\circ}\text{C}$$

The transient simulations of the energy equation were solved for the following input parameters:

$$i = \text{US06 Drive Cycle A, (Figure 3.3)}$$

$$V = 450, 650 \text{ V}$$

$$f_{sw} = 10, 20 \text{ kHz}$$

$$Q = 30, 60 \text{ CFM}$$

$$T_{inlet} = 50 \text{ }^{\circ}\text{C}$$

$$T_{amb} = 50, 120 \text{ }^{\circ}\text{C}$$

The fluid and material properties used all simulations throughout this study are given in Table 3.5.

Table 3.5 Properties used in the simulations

Property	Value	Unit	Source
Density of Air	1.1614	$kg/m^3$	[9]
Viscosity of Air	$1.85 * 10^{-5}$	$Pa * s$	[9]
Thermal Conductivity of Air	0.0263	$W/(m * K)$	[9]
Cp of Air	1007	$J/(kg * K)$	[9]
Thermal Conductivity of 4H-SiC	370	$W/(m * K)$	[11]
Density of 4H-SiC	3211	$kg/m^3$	[11]
Cp of 4H-SiC	690	$J/(kg * K)$	[11]
Thermal Conductivity of AlN	160	$W/(m * K)$	[11]
Density of AlN	3200	$kg/m^3$	[11]
Cp of AlN	740	$J/(kg * K)$	[11]
Thermal Conductivity of Cu	401	$W/(m * K)$	[9]
Density of Cu	8933	$kg/m^3$	[9]
Cp of Cu	385	$J/(kg * K)$	[9]
Thermal Conductivity of Al	237	$W/(m * K)$	[9]
Density of Al	2702	$kg/m^3$	[9]
Cp of Al	903	$J/(kg * K)$	[9]
Thermal Conductivity of Gel	0.17	$W/(m * K)$	[12]
Density of Gel	2330	$kg/m^3$	[9]
Cp of Gel	712	$J/(kg * K)$	[9]
Thermal Conductivity of Torlon	0.259	$W/(m * K)$	[13]
Density of Torlon	1410	$kg/m^3$	[13]
Cp of Torlon	1200	$J/(kg * K)$	[13]
Thermal Conductivity of the Capacitor	265	$W/(m * K)$	Calculated
Density of the Capacitor	6270	$kg/m^3$	Calculated
Cp of the Capacitor	820	$J/(kg * K)$	Calculated



### 3.10 Summary of the Thermal-Fluid Interaction Simulations

In order to summarize the overall process of the parametric study, and explain the interaction between the various inputs of the finite element simulations, a flow chart was drawn and is given in Figure 3.4. In all simulations, iterations continue until convergence on  $T_j$  has been reached. The value of  $T_j$  that is used in the heat generation equations is determined from the previous iteration. Once  $T_j$  converges, a steady state solution has been reached for that value of current. The iterative solver that was used throughout this project was the bi-conjugate gradient stabilization method (BiCGStab) with the geometric multi-grid pre-conditioner. The relative tolerance for the velocity simulations was set to  $1 * 10^{-3}$ , and the relative tolerance for the temperature simulations was set to  $1 * 10^{-6}$ .

The transient simulations operate on the same internal loop for  $T_j$ , but also include an external loop for current. In other words, the iteration for  $T_j$  is nested within the time stepping scheme for current. At each time step in the transient simulations, a converged solution for  $T_j$  must be reached before moving onto the next time step. Once a converged solution for  $T_j$  has been reached for all values of time, the transient simulation is then complete.

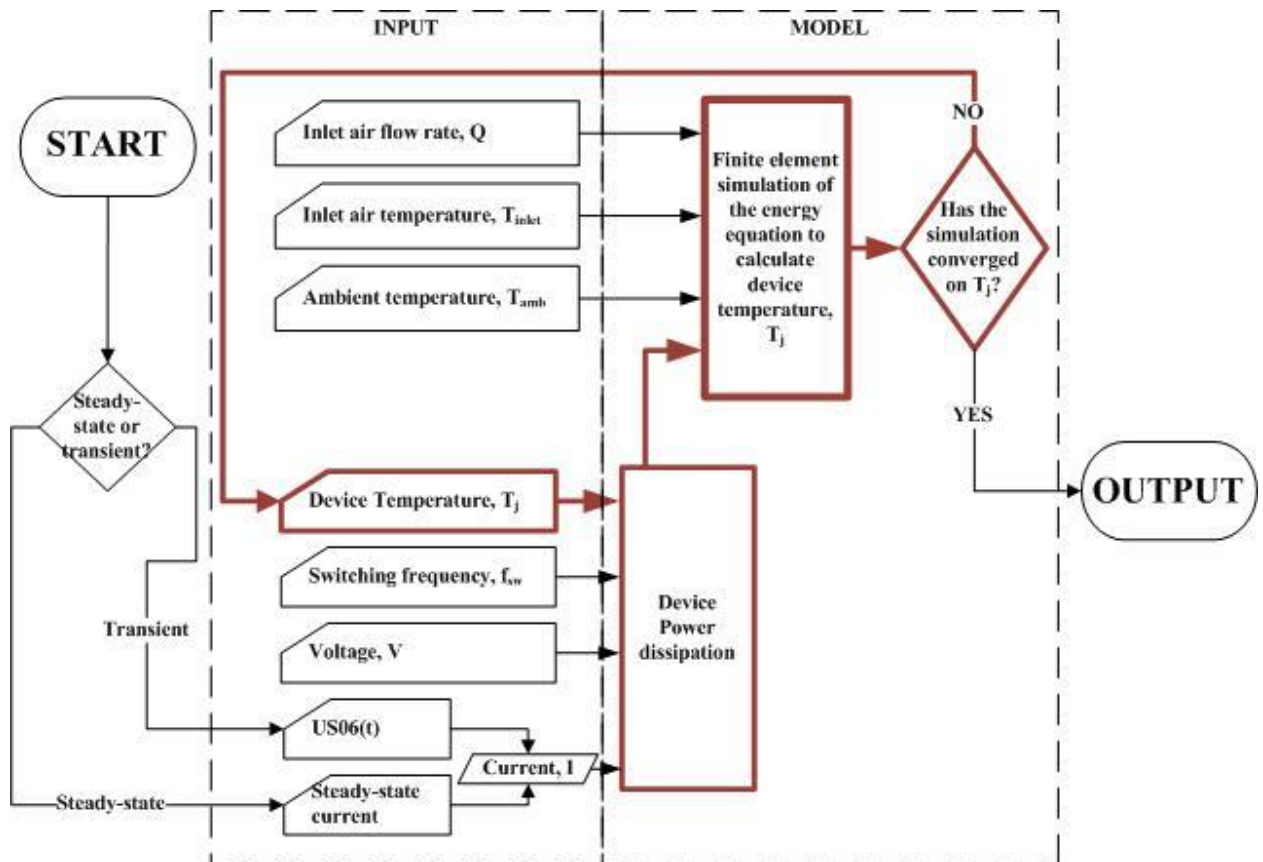


Figure 3.4 Flow chart of the simulations

## **Chapter 4. Module Design Details**

In this section, a discussion of the final inverter design of the FY 2010 feasibility study will be given. This design was developed after several design iterations. Along the way, there have been unforeseen issues that turned out to be significant problems. Some of these problems as well as the approach that was taken to overcome these problems will be discussed in the results section.

### **4.1 Motivation for the Module Based Design**

An inverter presents a lot of options to the designer. Because of the array of devices that make up an inverter, the designer can arrange them in various ways to meet the design objective. Planes of symmetry are very important for the numerical analyst. All of the relevant physics in the problem can be captured, and the performance of the entire inverter can be determined by studying a single unit cell of the overall system. Planes of symmetry were taken advantage of in the FY 2009 study, as shown in Figure 2.1. By modeling a unit cell of the entire inverter in the FY 2009 study, a new idea emerged. The basic idea is to optimize the performance of a single rectangular module, and then stack several modules together in a package to make an entire inverter, see Figures 4.1 and 4.2.



Figure 4.1 Isometric view of a single module



Figure 4.2 Three views of the entire inverter formed by stacking nine modules vertically.

If the module is designed to be self contained, it leaves the designer the freedom to arrange them in a configuration suitable for their application. It also provides a convenient maintenance solution. If the inverter was to fail, the damage could be contained within a single module. In this case, the module could be replaced and the rest of the system would be unharmed.

In summary, the module design concept is a simple, robust, and practical solution for this research study. It alleviates the concerns with manufacturability of the complex FY 2009 design.

## 4.2 DBA Card

Direct bonded aluminum (DBA) is a manufacturing process in which an aluminum trace is bonded to an aluminum nitride substrate by placing a liquid phase of aluminum between the two materials, and then cooling the liquid phase until solidification occurs. The aluminum nitride substrate is needed to provide electrical insulation to the electrically conducting traces. The DBA process substantially reduces contact resistance between the two materials, and has been the focus of much research aimed at high temperature electronic packaging applications. It was chosen for this application because of its low cost compared to the alternative direct bonded copper (DBC).

The DBA card used in this design is made up of three layers, see Figure 4.3. The top layer is the electrically conducting trace. The devices will be attached to this layer. The middle layer is the aluminum nitride substrate. It electrically insulates the trace from the rest of the module assembly. The third layer is another layer of aluminum. This layer does not conduct any electric current, and is included to add structural rigidity and strength to the card.

The DBA card comes pre-assembled from the manufacture. The thickness of the aluminum trace is 0.58 mm. The thickness of the aluminum nitride substrate is 0.66 mm.

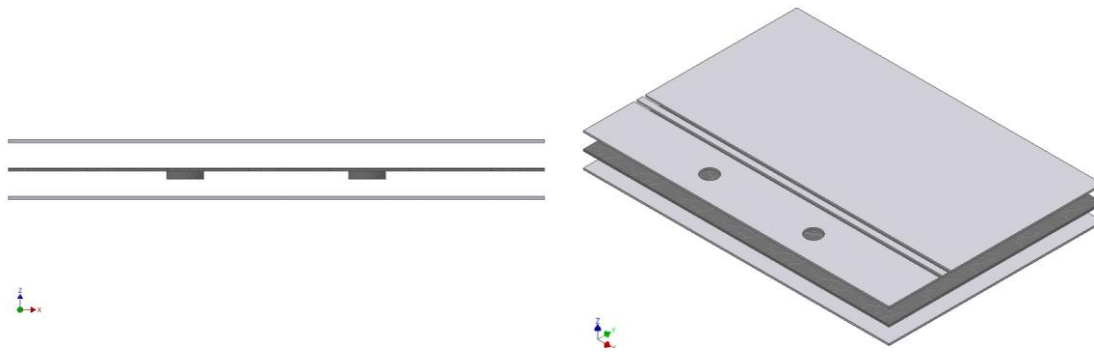


Figure 4.3 Front and isometric views of an exploded DBA card

There are three distinct sections of the trace seen in Figure 4.3. The largest section of the trace on one side of the module is the DC + trace, and the largest section on the other side of the module is the DC – trace. This can be seen more clearly in Figure 4.5. The DC + and DC - traces are directly connected to the capacitor. The smallest section located in the middle of the trace is the gate trace which is connected to the devices, and to the gate driver. The third and last section of the trace with the holes punched out of it is the phase trace. This section is connected to the motor outside of the inverter as can be seen in Figure 4.11.

Since the heat transfer coefficient of air-cooling is small, fins are necessary to meet the temperature requirements of the devices. The material for the fins was chosen to be aluminum, because of the low cost and coefficient of thermal expansion (CTE) of the material. It is important that the CTE of all materials used in the design be close to being the same throughout the entire inverter. The CTE of the aluminum fins will match up well with the CTE of the DBA card. Aluminum has favorable mechanical and thermal properties, and will perform well for this application.

One of the most critical tasks of this project was to optimize the design of the aluminum fins. In the FY 2009 project, fins were added on the outside of the card, and air was blown over the entire card and fin structure. This method is often referred to as direct cooling, since the air is in direct contact with the devices that are being cooled. The problem with this method of air-cooling is that particulates in the air can damage the devices. For the FY 2010 study, a decision was made early on to design a finned air-flow channel within the card and attach the traces on the outside of the channel. This design is very simple to manufacture, it removes the devices from direct contact with the air-flow domain, and it provides additional space for fins. The final design of the finned aluminum air-flow channel can be seen in Figure 4.4.

The relative dimensions regarding the thickness, span, and spacing of the fins were chosen from Scofield et al.[14]. They conducted a CFD parametric study that determined the optimal fin dimensions for air-cooling devices mounted onto a trace. The geometry in Scofield was not exactly the same as the one under consideration, but it was close enough to lead in the right direction.

In designing the fin channel, I wanted to maximize the surface area to volume ratio. In order to do this, I chose the smallest reasonable dimension for the thickness and spacing of the fins. This would allow us to maximize the number of fins in the channel. The fin thickness for the flow channel was chosen to be 1 mm, and the spacing between the fins was chosen to be 2 mm. There is a total of 34 fins in the final design of the flow channel. The span of the fins was limited by the overall volume of the inverter. After several design iterations, I settled upon a span of 15 mm.



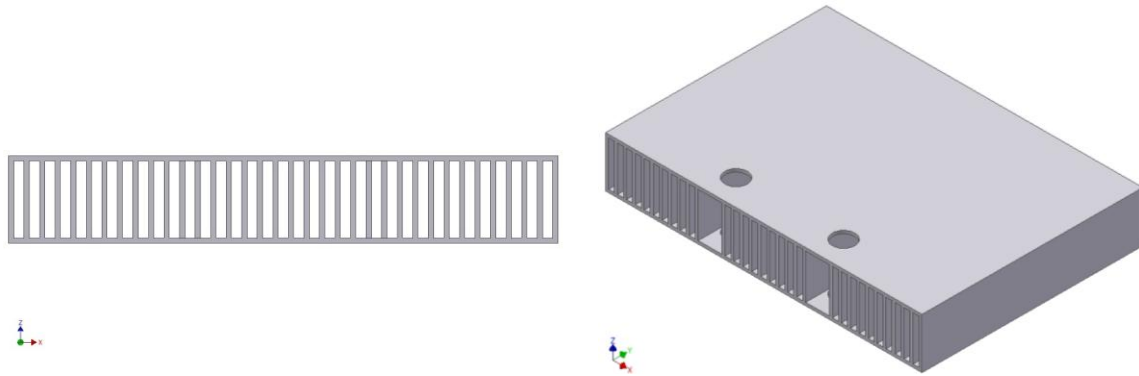


Figure 4.4 Front and isometric views of the finned flow channel

The assembled module consists of two DBA cards soldered onto the flow channel. There are a total of seven layers in the module, see Figure 4.5. Only the two outer most layers are conducting an electric current. The aluminum flow channel is electrically insulated from the DC + and DC – traces by the aluminum nitride substrate. The phase trace is connected by the copper bolts seen in the assembled module, Figure 4.6. This is the only mismatch of CTE in the entire module. It is not cause for concern though. Copper has a 26 % smaller coefficient of thermal expansion than aluminum. Therefore, the copper post will help hold the layers of the assembled module together as the module heats up, rather than push them apart.

As can be seen in Figure 4.6, there are six devices on the top trace. There are 6 on the bottom trace as well. We decided to use twelve devices per module instead of six to lower the current per device. This decreases the heat generation per device, and spreads the heat generation out over a greater area.

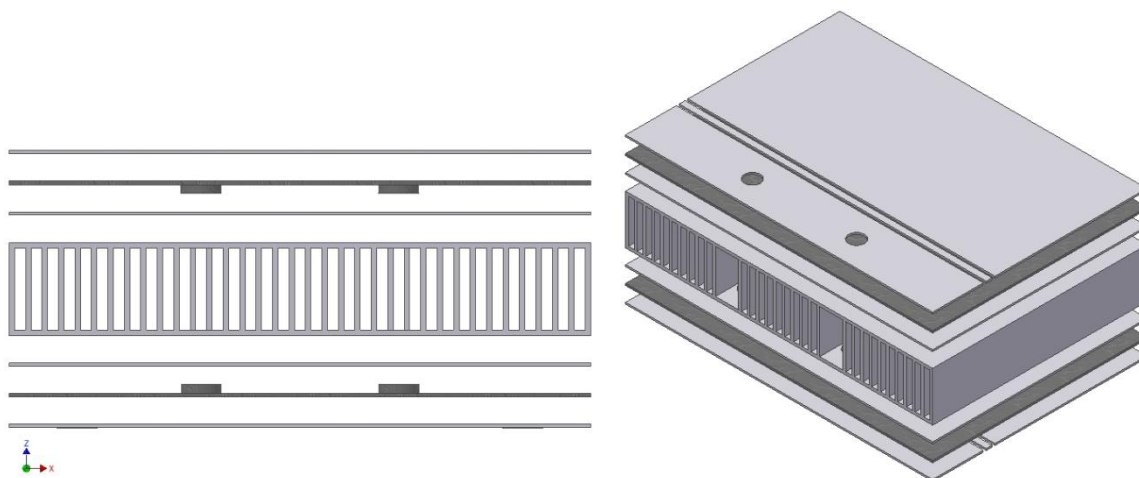


Figure 4.5 Front and isometric views of an exploded module assembly to illustrate the 7 layers

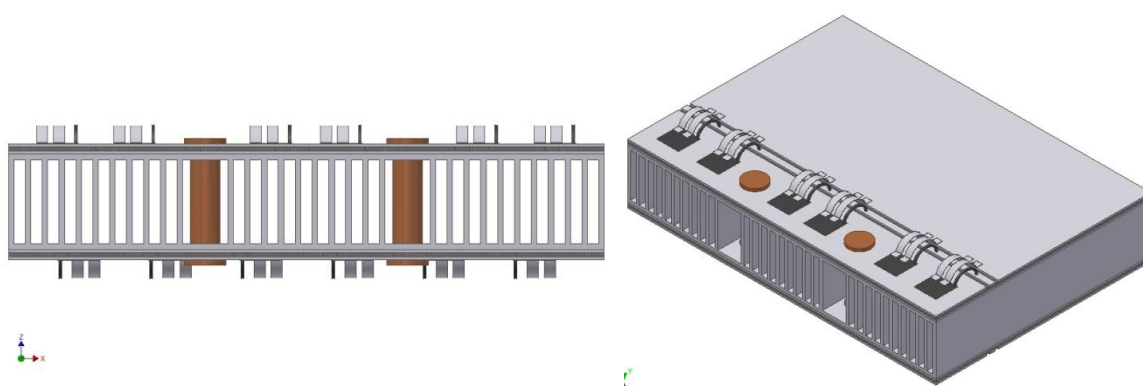


Figure 4.6 Front and isometric views of the assembled module

### 4.3 Motivation for the Relative Dimensions of the Trace

Since the efficiency of the device varies inversely with the junction temperature of the device, it is very important that all devices are close to the same temperature. In order to meet this requirement, the size of the upstream and downstream traces had to be adjusted to provide approximately the same amount of cooling to each trace. After several design iterations, the relative dimension of the traces needed to provide equal cooling to each trace was found and is shown in detail in Figure 4.7.

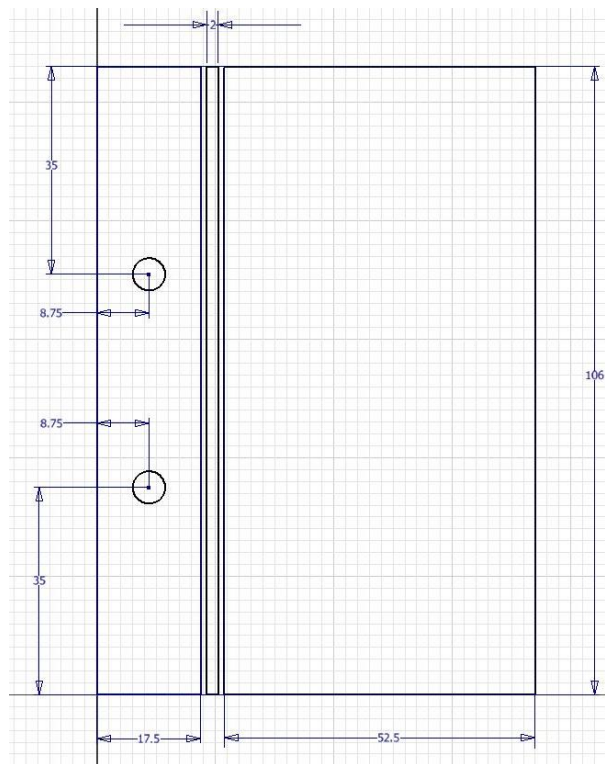


Figure 4.7 Top view of the trace showing the detailed dimensions of the final design. All dimensions are in mm

## 4.4 Electrical Connections

The electrical connections for the module design were developed in tandem with Chinthavali [10] from ORNL. Chinthavali is an electrical engineer, and provided the expertise needed to sufficiently design these connections. An isometric view of the final design of the connections without the card is given in Figure 4.8. The connections on the far left are the DC + and – connections. They connect the DC + and – traces to the capacitor. They are electrically insulated from one another by a layer of aluminum nitride. The pin connections at the bottom of Figure 4.9 are the gate connections. They connect the gate trace to the gate driver. The large connection on the bottom of Figure 4.8 is the phase connection. It connects the phase trace with the electric motor outside the module.

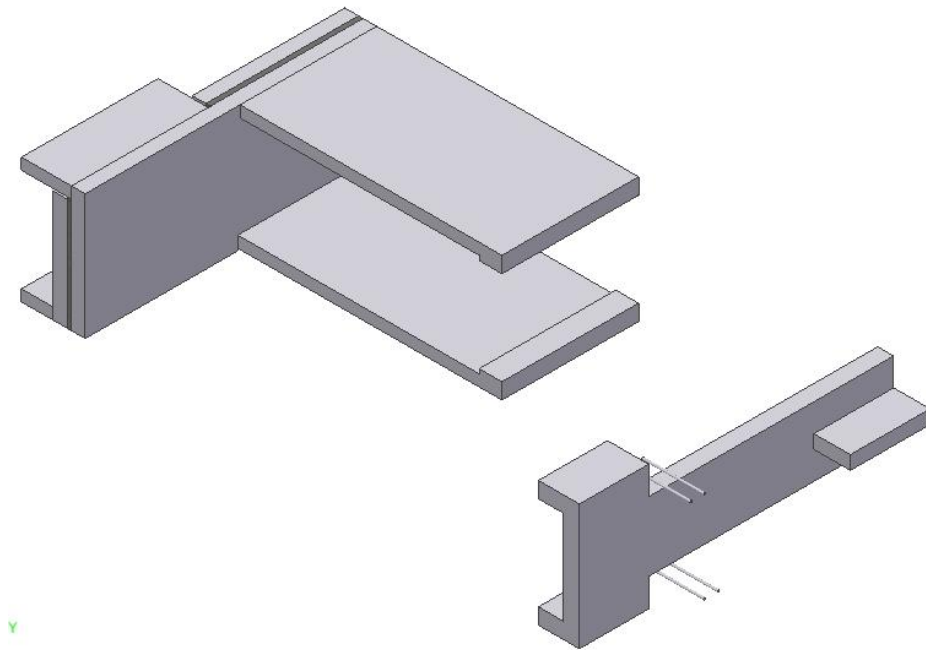


Figure 4.8 Isometric view of the electrical connections in the module

The primary concern in designing these connections is to ensure the cross sectional area of the connection is large enough to carry the 400 A of current for which the inverter is conservatively rated. The larger the cross sectional area, the more heat is transferred through them by conduction. This is especially detrimental in the DC connections, because the capacitor has strict temperature requirements. Therefore, the minimum cross sectional area required to conduct the maximum current rating of the inverter was chosen for this study. The current density of aluminum was assumed to be  $2.5 \text{ A/mm}^2$ .

## 4.5 Module Casing

The material for the module casing is Torlon<sup>TM</sup> [13], chosen for the desirable thermal and mechanical properties. Torlon<sup>TM</sup> is a thermo-set polymer which makes the design of the module casing seen in Figure 4.10 easily mass produced. Torlon<sup>TM</sup> has a maximum operating temperature of  $250^\circ\text{C}$  which makes it thermally feasible for this application. It is strong and stiff, and should perform well for this application. The thickness of the module casing was chosen to be 3 mm from engineering judgment. This thickness should provide for a reliable, robust design.

Recall that one of the objectives of the FY 2010 study was to substantially decrease the blower power required to provide sufficient cooling to the inverter. The ideal blower power is equal to the product of the volumetric flow rate of air through the inverter and the pressure drop across the inverter. The most practical way to lower the pressure drop across the inverter for this application is to streamline the solid parts of the module that are exposed

to the air-flow domain. One example of where this was done can be seen in Figure 4.9. Due to the required spacing for electrical connections on the top and bottom of the assembled card, the fluid domain must be converged before entering the finned flow channel. In order to decrease the additional pressure drop associated with this change in flow domain geometry, elliptical shaped flow guiders were implemented in the design. From wind tunnel tests, aerodynamic engineers have determined that ellipse shaped bodies have a smaller drag coefficient than cylindrical or wedge shaped bodies for sub-sonic flow [7]. Therefore, ellipse shaped flow guiders were chosen for this application.

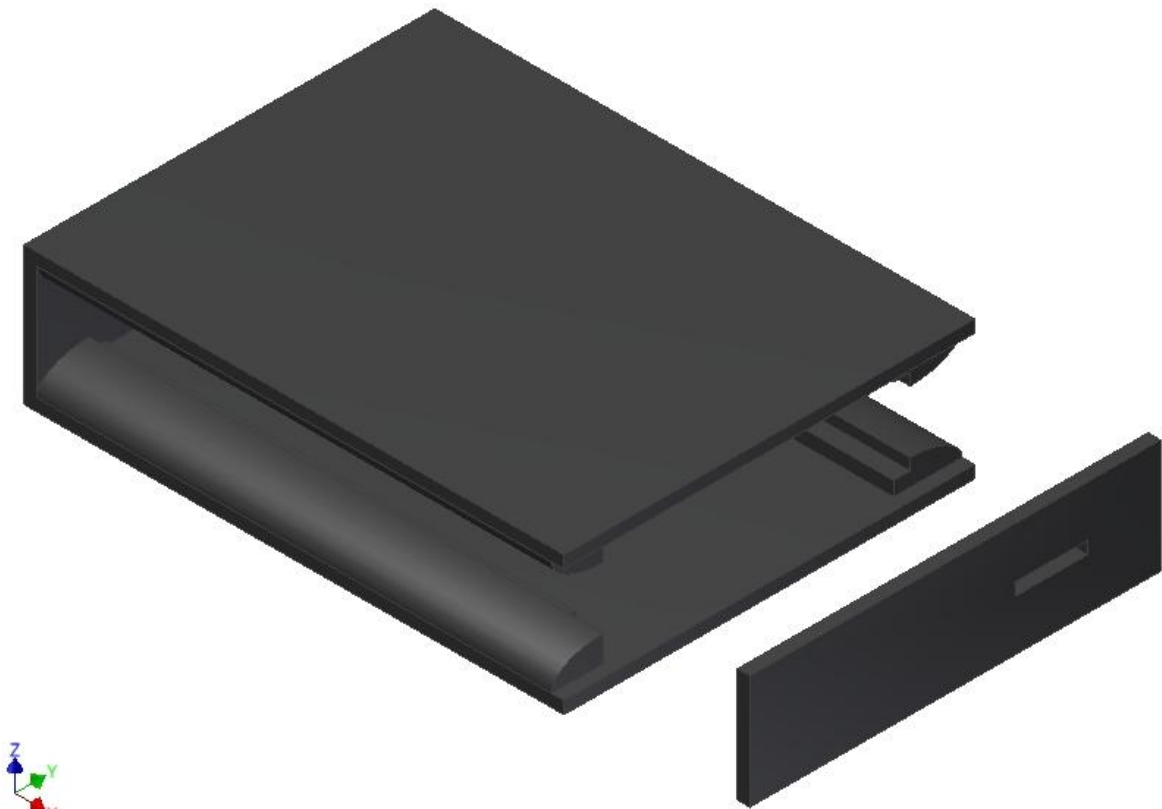


Figure 4.9 Isometric view of the exploded module casing

## 4.6 Assembly Details

As can be seen in Figures 4.9 and 4.10, the entire module casing is made out of two parts. The assembled card with electrical connections slides into the large part of the module casing from the side, and the capped end is then bolted on to secure the card in place. The card rests on built in shelves mounted to the inside of the elliptical flow guiders within the casing. A small section of these shelves can be seen in Figure 4.9. This assembly process is very simple and robust, and should work well for this application.

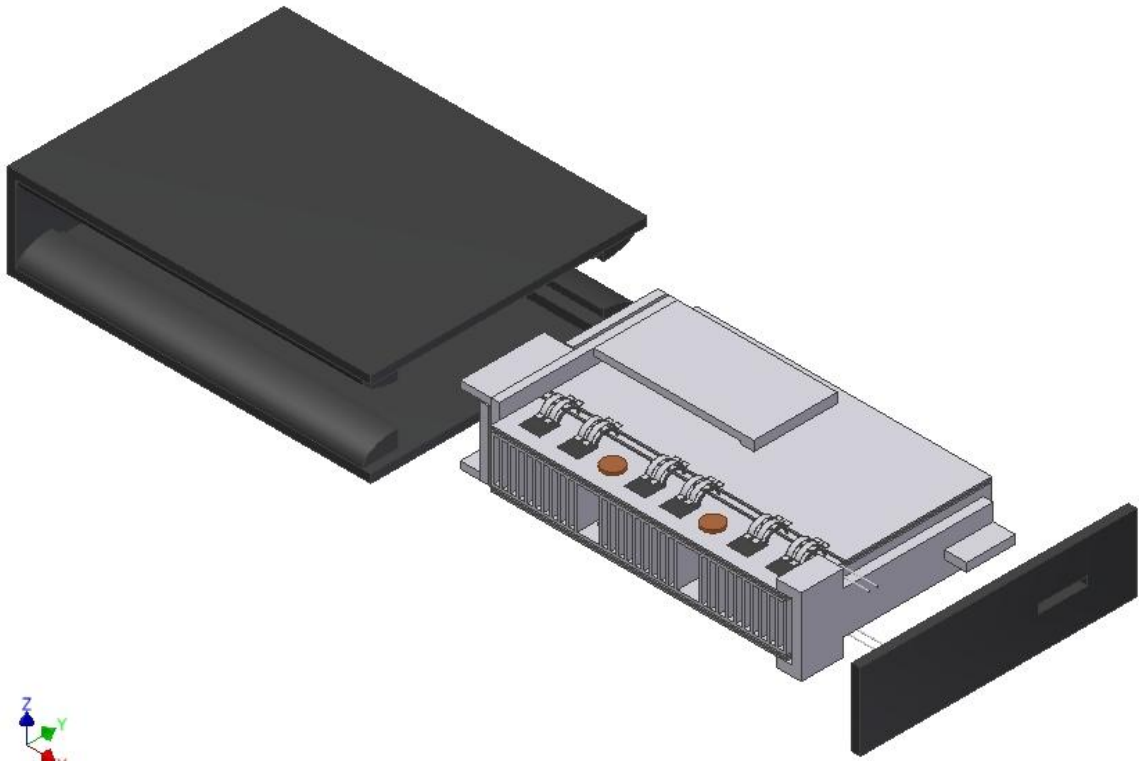


Figure 4.10 Isometric view of the exploded module assembly

## 4.7 Power Density Calculation

The overall dimensions of the module are shown in Figure 4.11. The volume of one module is found to be 0.416 L, and the volume of a sample rectangular capacitor was given by Chinthavali [10] to be 1.34 L. Therefore, the volume of a stack of nine modules is found to be 3.74 L, and the volume of the entire rectangular inverter is found to be 5.1 L. The power rating for the inverter is determined to be 60 kW from

$$Power\ Rating = \frac{4*PF*V*I}{2\pi\sqrt{2}} \quad (4.2)$$

with the  $PF$  (power factor) = 0.85,  $V = 650$  V, and  $I = 240$  A. The power density of the final module design with  $V = 650$  V and  $I = 240$  A is determined to be 11.75 kW/L which is comparable with the alternative liquid-cooled systems.



Figure 4.11 Isometric view of the assembled module with dimensions



## Chapter 5. Results and Discussion

The results for the finite element simulations of the final module design are now presented. A discussion of the validity of the results is given in Section 5.5.

### 5.1 Steady State Velocity Results

A plot of the velocity field in the fluid domain for  $Q = 40$  CFM, or  $0.01878 \frac{m^3}{s}$  is given in Figure 5.1. The cross sectional area of the inlet boundary of the fluid domain is equal to  $0.004188 m^2$ . Therefore, the average velocity at the inlet of the simulation was specified to be  $4.51 \frac{m}{s}$ . The fluid domain converges to a smaller cross sectional area in the finned flow channel. The convergence of the fluid domain accelerates the fluid to a maximum velocity of  $32.3 \frac{m}{s}$  in the channel. The maximum velocity in the fluid domain is confined to a small portion of the domain as shown in Figure 5.2. Throughout most of the fluid domain, the maximum velocity is less than  $18 \frac{m}{s}$ . The minimum velocity in the fluid domain is equal to  $0 \frac{m}{s}$  to satisfy the no slip boundary condition.

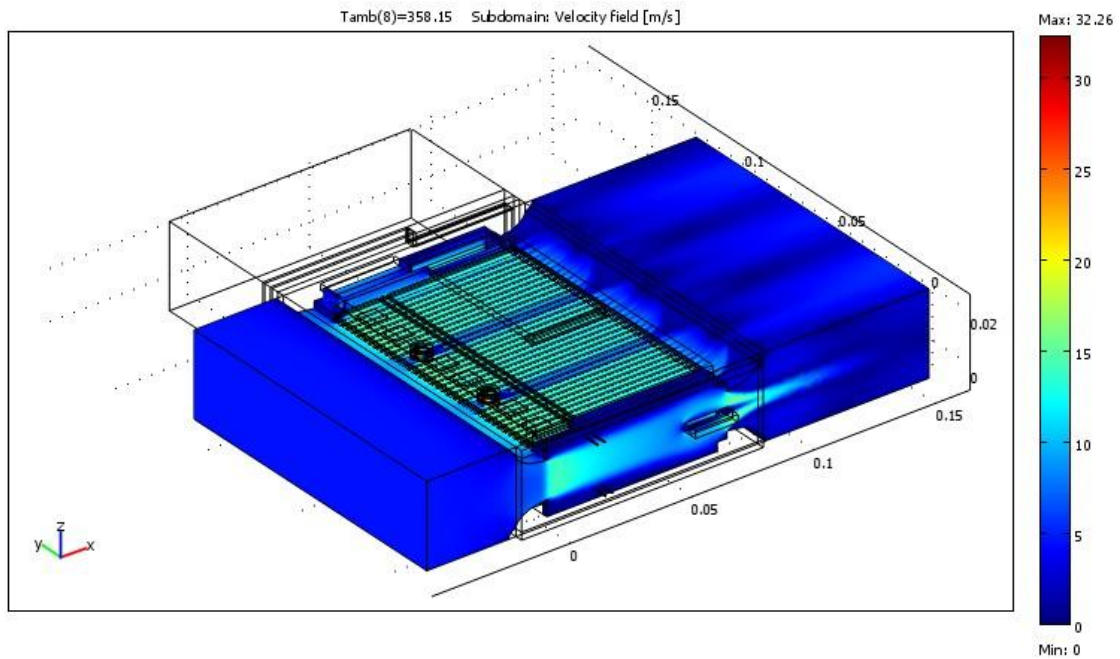


Figure 5.1 Isometric view of the velocity field for  $Q = 40$  CFM

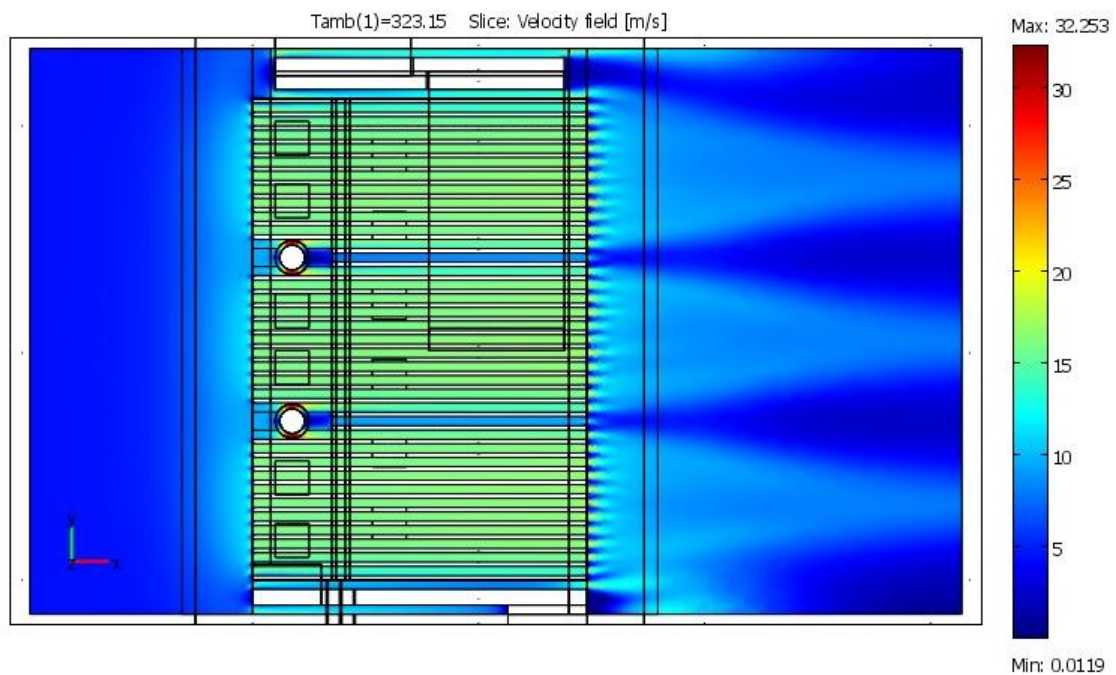


Figure 5.2 Top view of a slice plot of the velocity field through the middle of the fluid domain with  $Q = 40$  CFM

A plot of the pressure distribution in the fluid domain is given in Figure 5.3. The gauge pressure was specified to be 0 Pa at the exit of the fluid domain. The average pressure on the inlet boundary of the fluid domain was determined to be 187 Pa. Therefore the pressure drop across the module in this simulation was determined to be 187 Pa.

From Bernoulli's equation, we know the relationship between flow rate and pressure drop for an in viscid flow is  $\Delta P \sim \Delta Q^2$ . Although air is a viscous fluid, the results of these simulations are very consistent with in viscid flow theory over this range of flow rates. A plot of the pressure drop across the inverter versus flow rate per module is given in Figure 5.4 for all flow rates considered in this study.

The ideal blower power required to drive the flow field is given by White [7] as

$$\text{Ideal Blower Power} = Q * \Delta P \quad (5.1)$$

The ideal blower power required to drive the flow for the FY 2009 project with  $Q = 60$  CFM per module was determined to be 967 W. The ideal blower power required to drive the flow for the FY 2010 project with  $Q = 60$  CFM per module was determined to be 105 W. By eliminating the convective acceleration term associated with the change in cross sectional area of the fluid domain, the blower power requirements have decreased by 89 %. A plot of the ideal blower power required to drive the flow versus flow rate through the entire inverter is given in Figure 5.5 for all flow rates considered in this study. All of the results for the steady state fluid velocity simulations are given in Table 5.1.

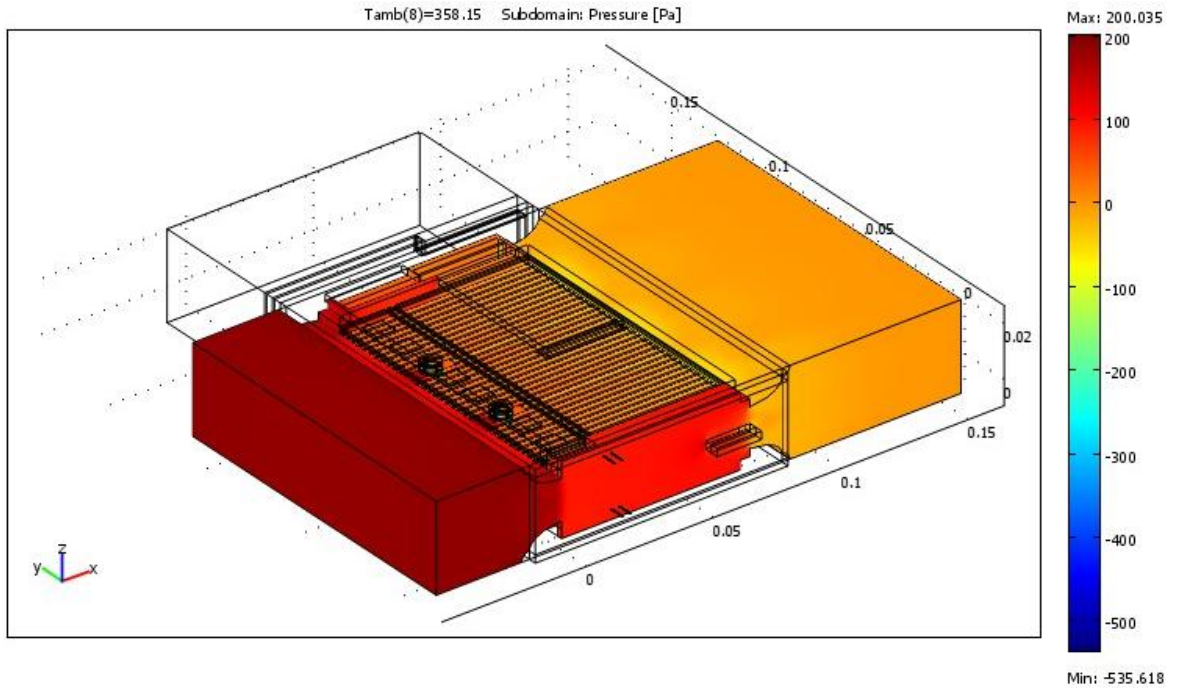


Figure 5.3 Isometric view of the pressure distribution in the fluid domain for  $Q = 40$  CFM

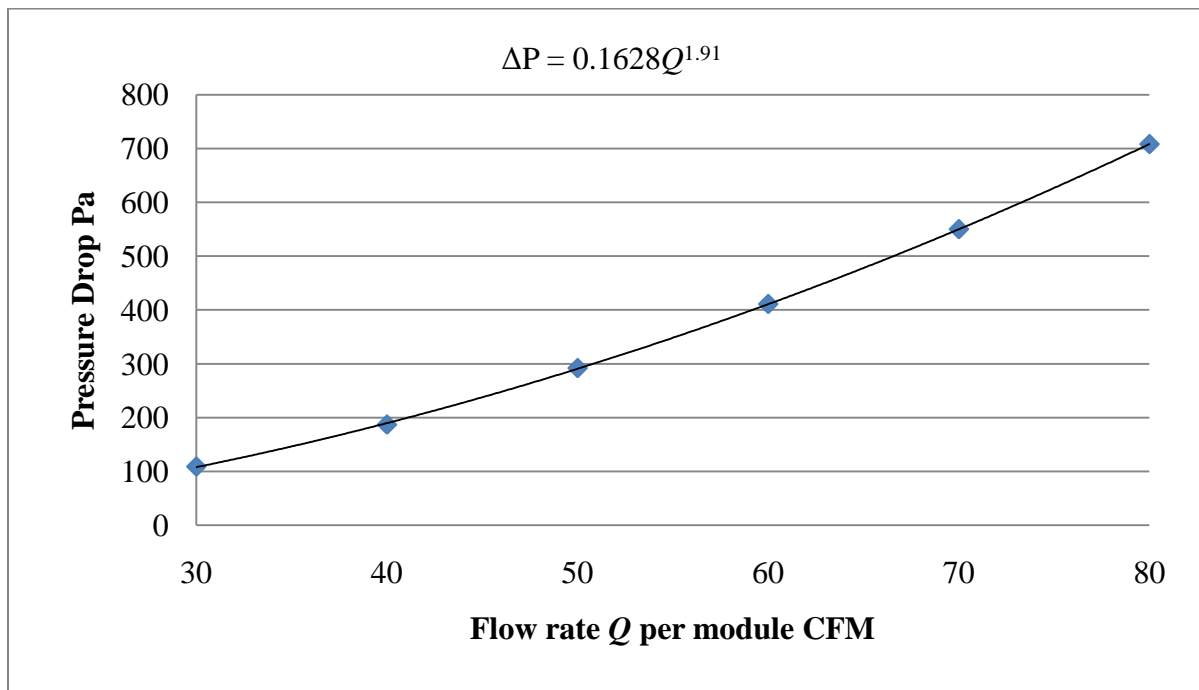


Figure 5.4 Plot of the pressure drop across the inverter versus flow rate per module

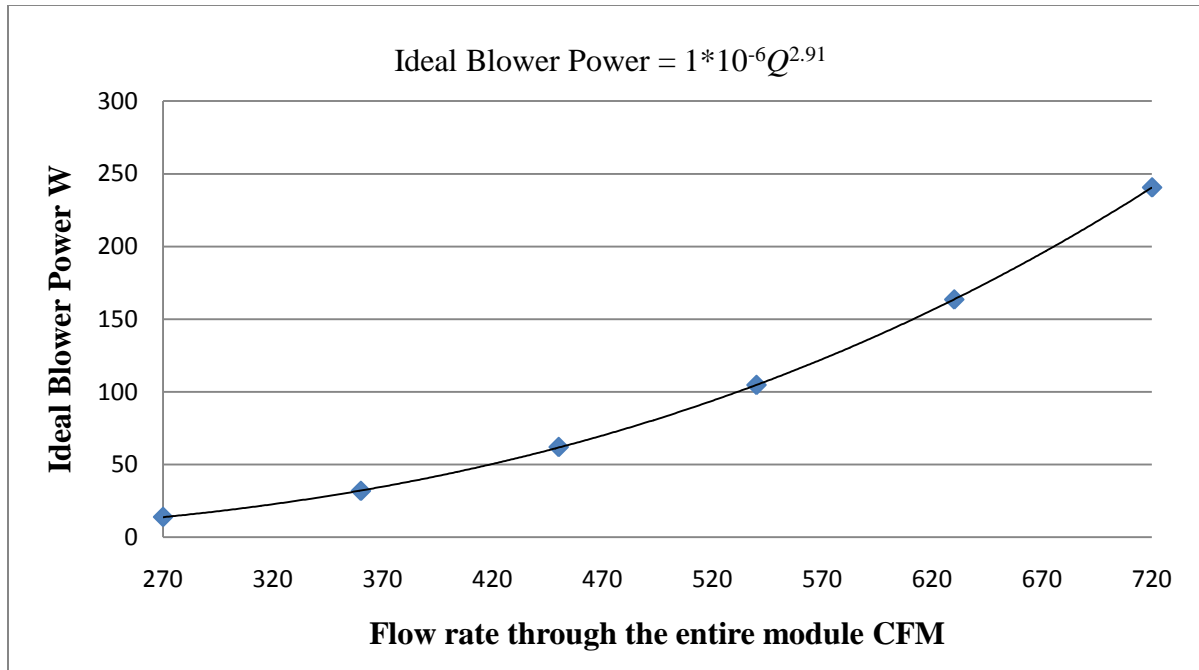


Figure 5.5 Plot of the ideal blower power required to drive the flow field as a function of flow rate through the entire inverter

Table 5.1 Results for the steady state velocity simulations

$Q$ per Module, CFM	30	40	50	60	70	80
$Q$ for Entire Inverter, CFM	270	360	450	540	630	720
Inlet Velocity, m/s	3.38	4.51	5.63	6.76	7.89	9.02
$\Delta P$ Across the Entire Inverter, Pa	109	187	292	411	550	708
Ideal Blower Power for the Entire Inverter, W	13.9	31.8	62	104.7	163.5	240.6

## 5.2 Steady State Temperature Results

A plot of the temperature distribution in all solid domains for  $Q = 60$  CFM and  $T_{inlet} = 50$  °C is given in Figure 5.6. The maximum temperature in the simulation is determined to be 184 °C, which is well below the maximum operating temperature of the Si-C devices. The maximum capacitor temperature in this model is less than 100 °C, which meets the temperature requirement given by the manufacturer. Therefore, a flow rate of  $Q = 60$  CFM per module is determined to be provide sufficient cooling for the proposed design under steady state operating conditions with  $T_{inlet} = 50$  °C .

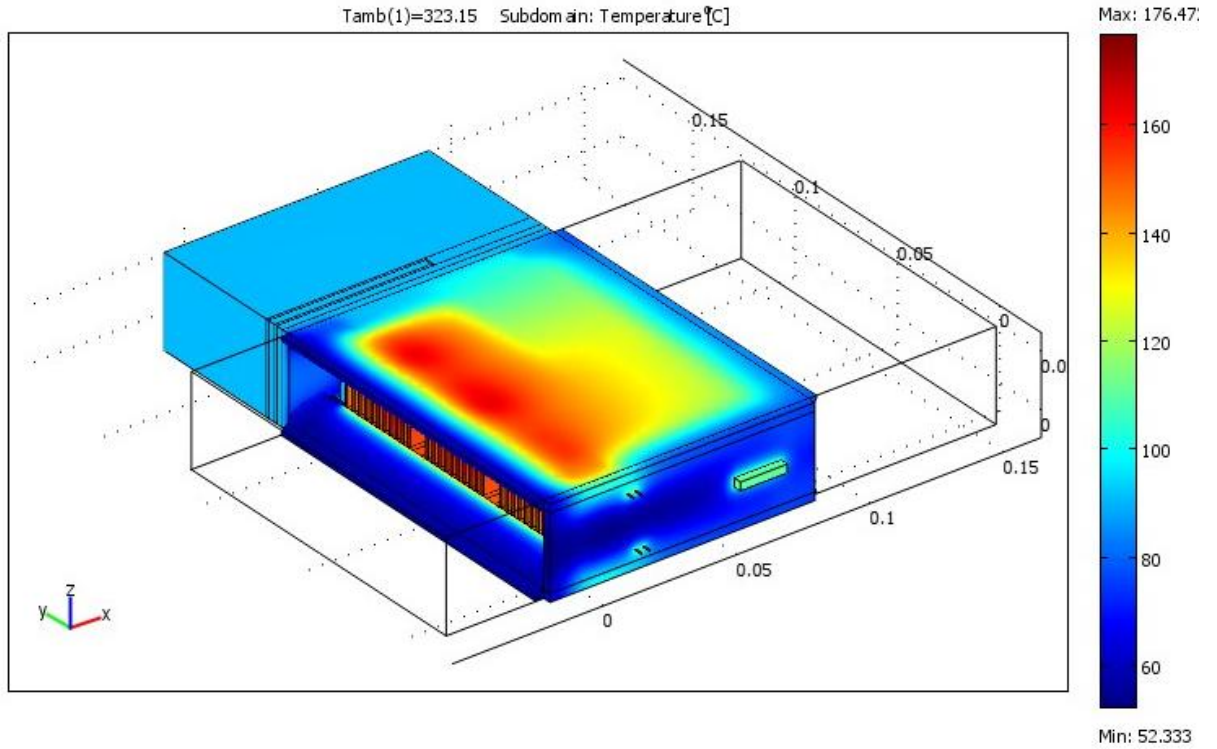


Figure 5.6 Isometric view of the solid temperature distribution with  $I = 60$  CFM and  $T_{inlet} = 50$  °C

A plot of the temperature distribution in all solid domains for  $Q = 40$  CFM and  $T_{inlet} = 50$  °C is given in Figure 5.7. The maximum temperature in the simulation is determined to be 252 °C, which is close to the maximum operating temperature of the Si-C devices. Notice the similarity of the temperature distributions shown in Figures 5.6 and 5.7. The two temperature distributions are nearly identical in shape, and differ only in magnitude.

In all steady state simulations, the device temperatures are outside the range of temperatures of the experiment that determined the heat generation equations. Extrapolation is always a cause for concern. However as will be presented in Section 5.3, the device temperatures in the transient simulations are lower than those resulting in the steady state simulations, and are within the temperature range of the experiment. Therefore, the heat generation functions used in the transient simulations is not extrapolated.

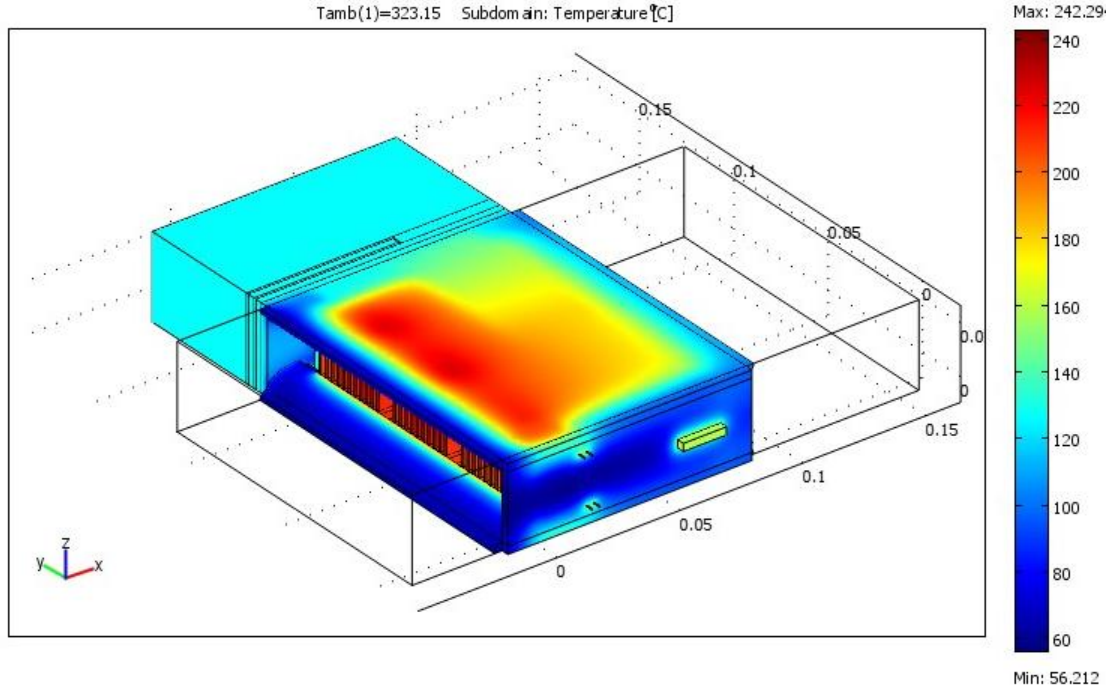


Figure 5.7 Isometric view of the solid temperature distribution with  $Q = 40$  CFM and

$$T_{inlet} = 50$$

A plot of the maximum diode and MOSFET temperatures versus  $T_{inlet}$  for all flow rates considered in this study is given in Figure 5.8. Here,  $T_D$  and  $T_m$  represent the maximum diode and MOSFET temperatures respectively.

As expected, all temperatures increase with an increase in  $T_{inlet}$ , and decrease with an increase in air flow rate. Note that the steady state simulations describe a very conservative operating condition. As a consequence, the temperatures come out to be high for all cases. However, these temperatures are useful because they correspond to the upper limit on temperature that the device can reach.

As shown in Figure 5.8, the hottest diode is at a higher temperature than the hottest MOSFET. This is because the diodes are generating more heat than the MOSFET's. A trend can be established from Figure 5.8. Increasing the flow rate from 40 to 50 CFM substantially decreases device temperatures, but further increasing the flow rate from 50 to 60 CFM only slightly decreases device temperatures. This is because the heat generation equations follow a quadratic curve fit, and the higher temperature simulations are generating substantially more heat than the lower temperature simulations. When the flow rate was lowered below 40 CFM, the device temperatures approached infinity and a converged solution could not be obtained. The parametric study has established that the minimum flow rate required to provide sufficient cooling under steady state operating conditions with  $T_{inlet} = 50\text{ }^{\circ}\text{C}$  is 50 CFM per module.



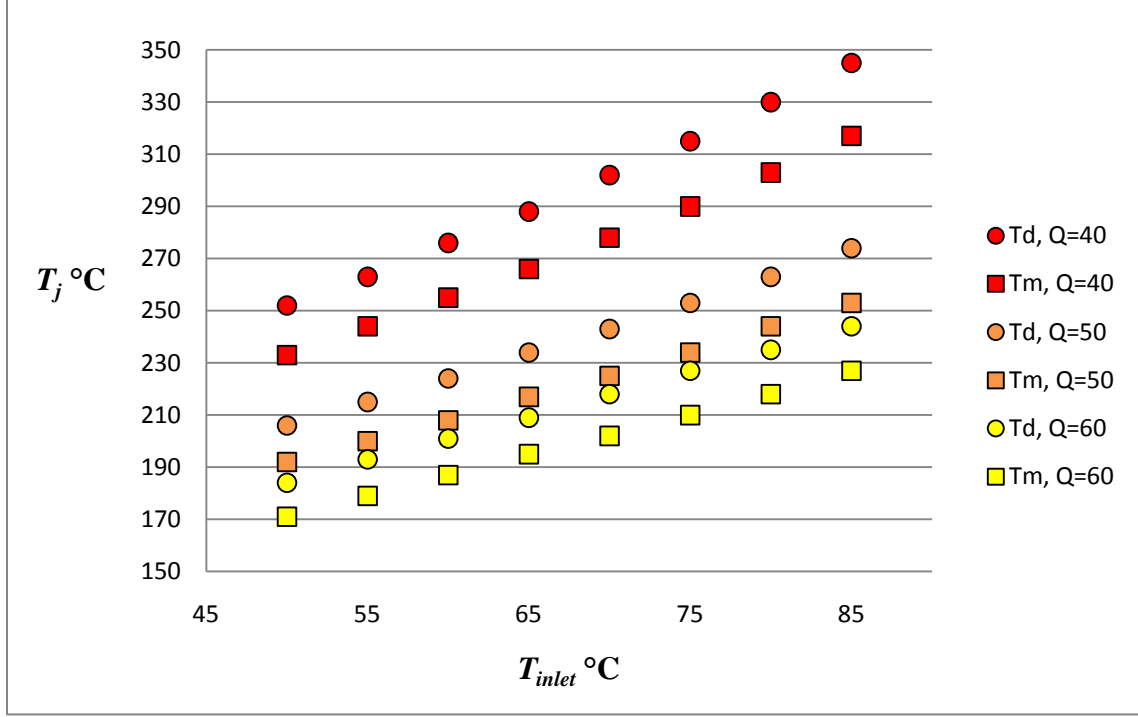


Figure 5.8 Plot of the maximum device temperatures versus  $T_{inlet}$  for  $Q = 40, 50, 60$  CFM

A plot of the heat generation rate per module versus  $T_{inlet}$  for all flow rates considered in this study is provided in Figure 5.9. The heat generation rates are determined from the solutions of the simulations. The steady state temperature results of the parametric study are given in Table 5.2. Each module contains six MOSFETs and six diodes.  $\dot{E}_{gen}$  in Figure 5.9 and Table 5.2 is the sum of the heat generation rates of these twelve devices. The heat generation of each device is proportional to its local temperature. Therefore, as  $T_{max}$  decreases,  $\dot{E}_{gen}$  will also decrease and the net effect is a more efficient inverter. From Table 5.1, when  $Q$  is increased from 40 to 60 CFM, the ideal blower power for the entire inverter increases by 72.9 W. Correspondingly from Table 5.2,  $\dot{E}_{gen}$  decreases by 120 W because  $T_{max}$  decrease by 78 °C. Therefore, the additional power requirement for increasing  $Q$  is more than offset by the change in  $\dot{E}_{gen}$ . Even more significant is the decrease in  $T_j$ .

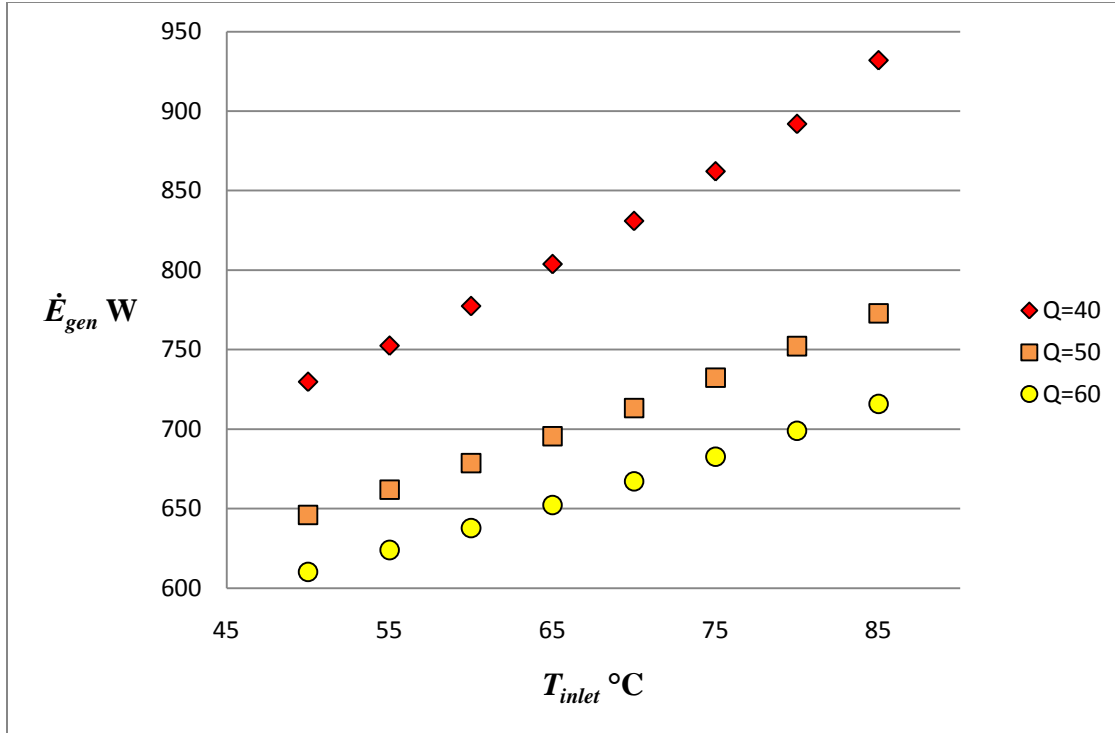


Figure 5.9 Plot of the heat generation rate versus  $T_{inlet}$  for  $Q = 40, 50, 60$  CFM

Table 5.2 Results of the steady state temperature simulations showing the influence of air flow rate and inlet temperature on the maximum device temperatures and total heat generation rates

	$Q = 40$ CFM		$Q = 50$ CFM		$Q = 60$ CFM	
$T_{inlet}, ^\circ\text{C}$	$T_{max}, ^\circ\text{C}$	$\dot{E}_{gen}, \text{W}$	$T_{max}, ^\circ\text{C}$	$\dot{E}_{gen}, \text{W}$	$T_{max}, ^\circ\text{C}$	$\dot{E}_{gen}, \text{W}$
50	252	730	206	646	184	610
55	264	753	215	662	193	624
60	276	777	224	679	201	638
65	288	804	234	696	209	652
70	302	831	243	713	218	667
75	315	862	253	732	227	683
80	330	892	263	752	235	699
85	346	932	274	773	244	716

From Figures 5.8 and 5.9,  $T_j$  and  $\dot{E}_{gen}$  appear to vary linearly with  $T_{inlet}$ , but this is not the case. As shown in Table 5.3, the relationship between  $T_j$  versus  $T_{inlet}$ , and  $\dot{E}_{gen}$  versus  $T_{inlet}$  is indeed nonlinear, and the nonlinearity decreases with increasing flow rate. The cause of this nonlinearity is  $\dot{E}_{gen}$  is directly dependent upon  $T_j$ , and increasing  $T_{inlet}$  will raise  $T_j$  as well as  $\dot{E}_{gen}$ . Rising  $\dot{E}_{gen}$  will in turn raise  $T_j$  further and the cycle will continue until convergence is reached

Table 5.3. Results of the steady state temperature simulations to illustrate the nonlinear trend in the results between  $T_j$  versus  $T_{inlet}$ , and  $\dot{E}_{Gen}$  versus  $T_{inlet}$  for  $Q = 40$  and  $60$  CFM

	$Q = 40$ CFM							
$T_{inlet}$ °C	50	55	60	65	70	75	80	85
$T_{max}$ °C	252	264	276	288	302	315	330	346
$\Delta T$ °C		12	12	12	14	13	15	16
$\dot{E}_{Gen}$ W	730	753	777	804	831	862	892	932
$\Delta \dot{E}_{Gen}$ W		23	25	26	27	31	30	40

	$Q = 60$ CFM							
$T_{inlet}$ °C	50	55	60	65	70	75	80	85
$T_{max}$ °C	184	193	201	209	218	227	235	244
$\Delta T$ °C		9	8	8	9	9	8	9
$\dot{E}_{Gen}$ W	610	624	638	652	667	683	699	716
$\Delta \dot{E}_{Gen}$ W		14	14	15	15	16	16	17

Figure 5.10 is a plot of the temperature of the twelve devices. As can be seen in Figure 5.10, the upstream devices are hotter than the downstream devices. This is because the relative dimensions of the trace were overdone, i.e., in order to obtain a more uniform temperature distribution throughout the devices, the upstream trace could be extended by a few millimeters.

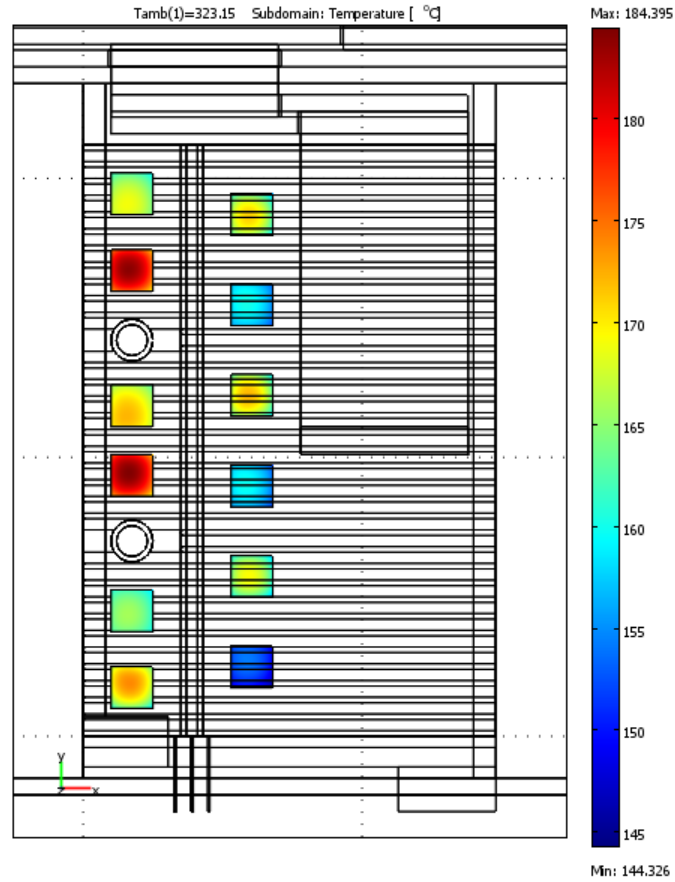


Figure 5.10 Top view of the devices temperature distribution with  $Q = 60$  CFM and  $T_{inlet} = 50^{\circ}\text{C}$

A plot of all 12 device temperatures versus  $T_{inlet}$  for  $Q = 60$  CFM is given in Figures 5.11 and 5.12. This plot is included to illustrate that there are temperature differences between the maximum temperatures of the devices. As previously stated, since the efficiency of the devices is dependent on the local junction temperature of the device, it is crucial that all devices be at close to the same temperature throughout the inverter. As can be seen in Figure 5.11, the temperature difference between the hottest MOSFET and the coldest MOSFET is at most 20 °C. This temperature difference is acceptable. A schematic of the module illustrating the location of the devices referred to in Figures 5.11 and 5.12 is given in Figure 5.13.

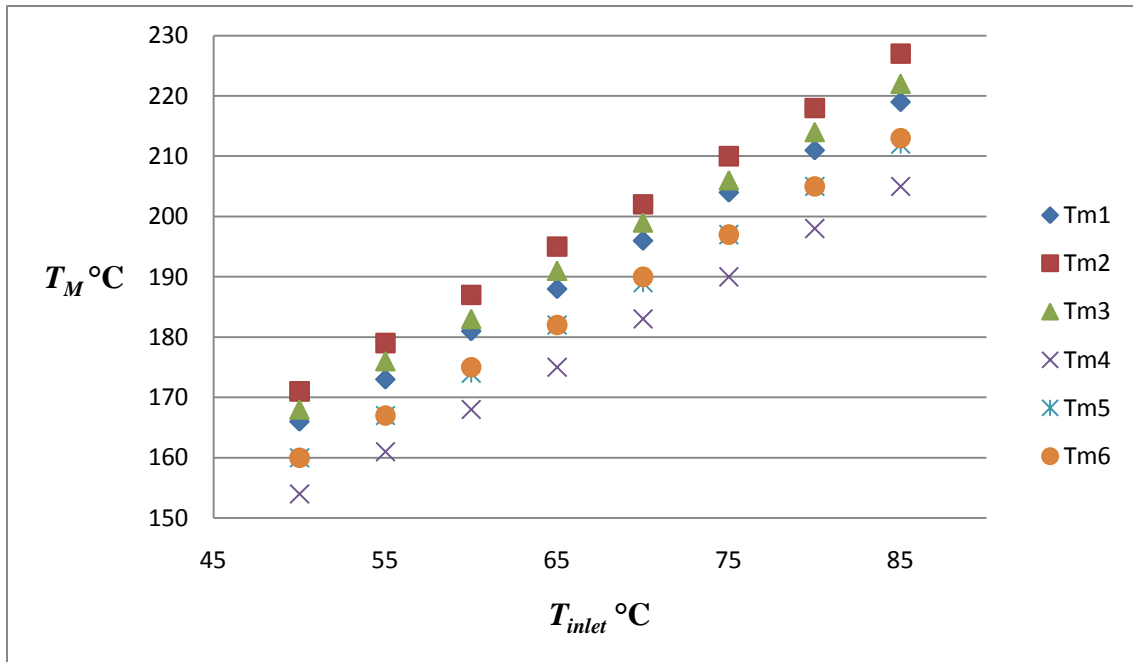


Figure 5.11 Plot of all MOSFET temperatures to illustrate the temperature difference among them,  $Q = 60$  CFM

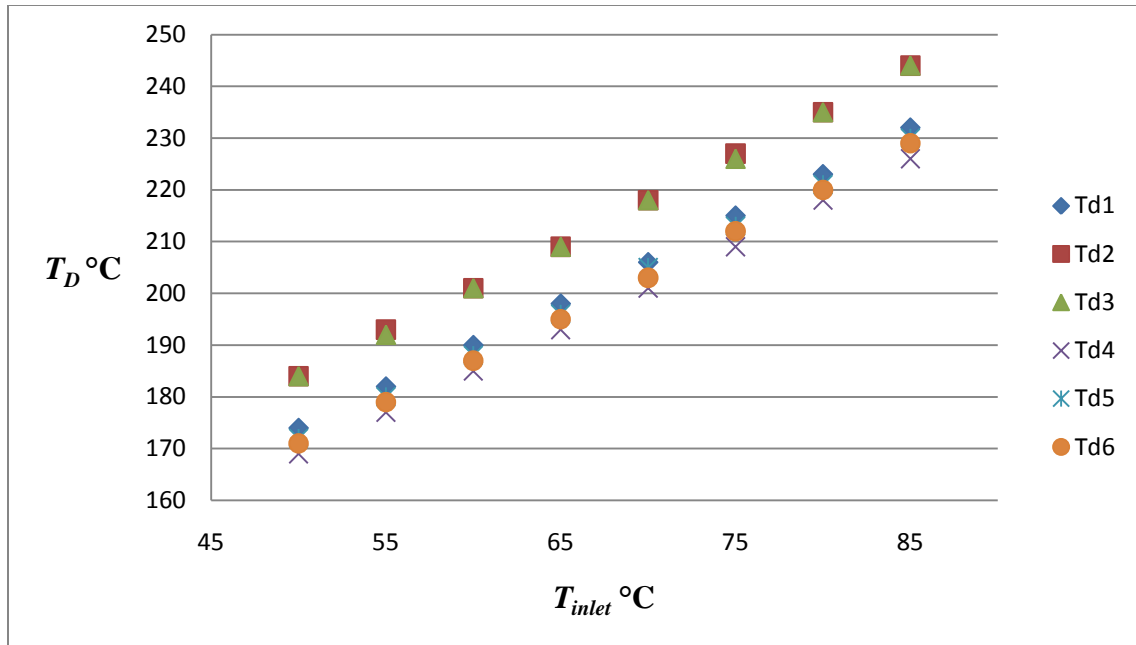


Figure 5.12 Plot of all diode temperatures to illustrate the temperature difference among them with  $Q = 60$  CFM

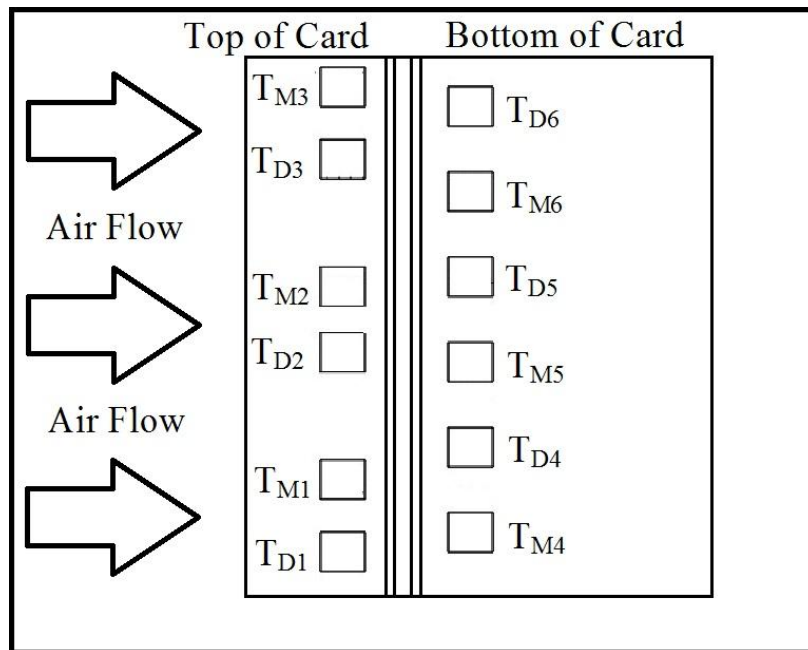


Figure 5.13 Schematic of the card showing the locations of the devices referred to in Figures 5.11 and 5.12

To demonstrate the performance of the fins, slice plots of the steady state solid temperature distribution of the module cross section and the flow channel cross section are provided in Figures 5.15 through 5.17 and in Figures 5.19 through 5.21. In all of these Figures,  $Q = 40$  CFM and  $T_{amb} = 50$  °C.

The locations of the planes used in Figures 5.15 through 5.17 are illustrated in Figures 5.14. In Figure 5.14, three vertical planes that are normal to the flow direction are shown. The front plane in Figure 5.14 is through the mid-plane of the upstream devices, the middle plane in Figure 5.14 is through the mid-plane of the gate trace, and the back plane in Figure 5.14 is through the mid-plane of the downstream devices.

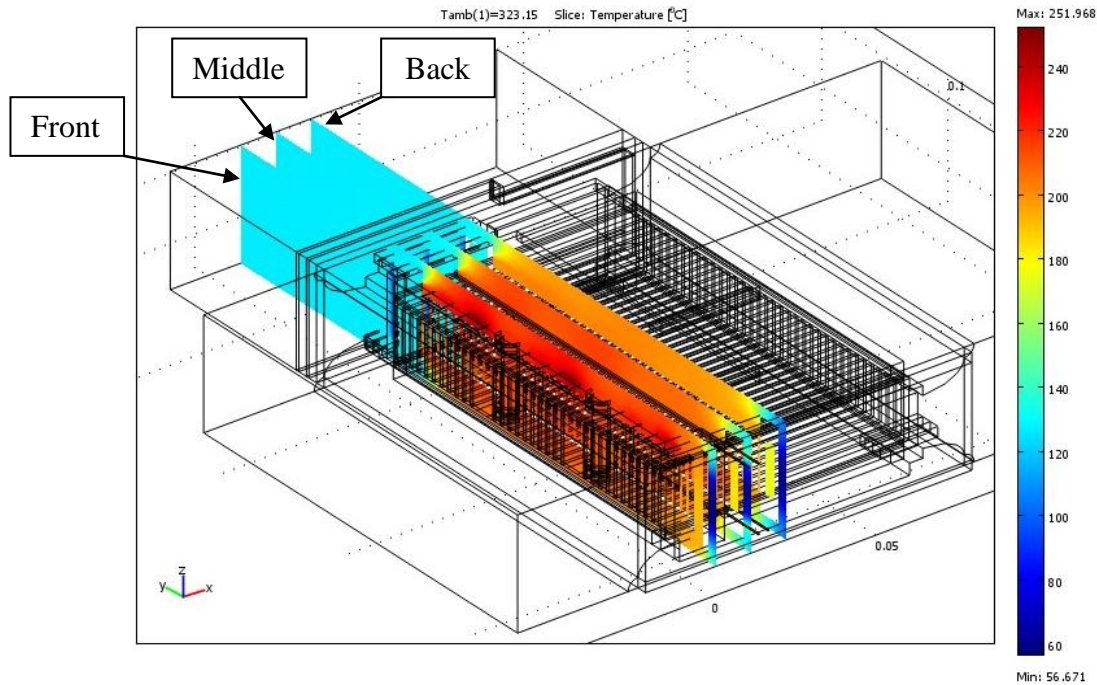


Figure 5.14 Isometric view of the slice plots showing the location of the planes used in Figures 5.15 through 5.17 and Figure 5.22

Figures 5.15 (a) through 5.17 (a) show the solid temperature distribution of a cross section of the entire module on the three vertical planes shown in Figure 5.14, while 5.15 (b) through 5.17 (b) show the temperature distribution of a cross section of the flow channel alone on these three vertical planes. In all of these six Figures,  $Q = 40$  CFM.

The heat transfer in the design under consideration is highly three dimensional. As can be seen from the temperature distribution shown in Figure 15 (b), nearly all of the heat conduction in the front plane is from the top to the bottom of the plane. Furthermore as can be seen in Figure 16 (b), the heat conduction in the middle plane is from the top and the bottom of the plane which results in a more uniform temperature distribution. Finally as can be seen in Figure 17 (b), nearly all of the heat conduction in the back plane is from the bottom to the top of the plane.

The maximum temperature on the cross section shown in Figure 15 (a) is equal to the maximum temperature of the upstream devices, and the maximum temperature on the cross section shown in Figure 17 (a) is the maximum temperature of the downstream devices.



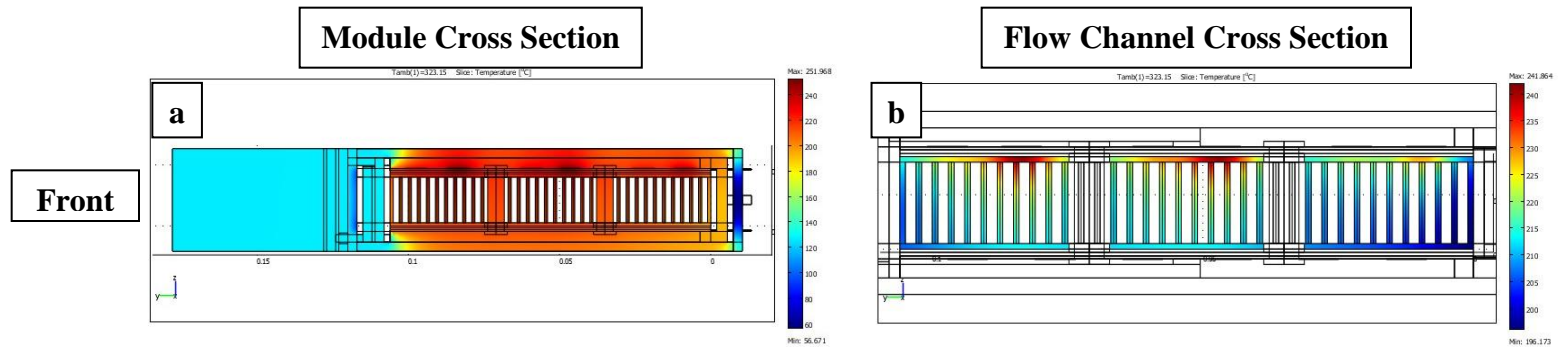


Figure 5.15 Slice plot of the temperature distribution on the front plane with  $Q = 40$  CFM

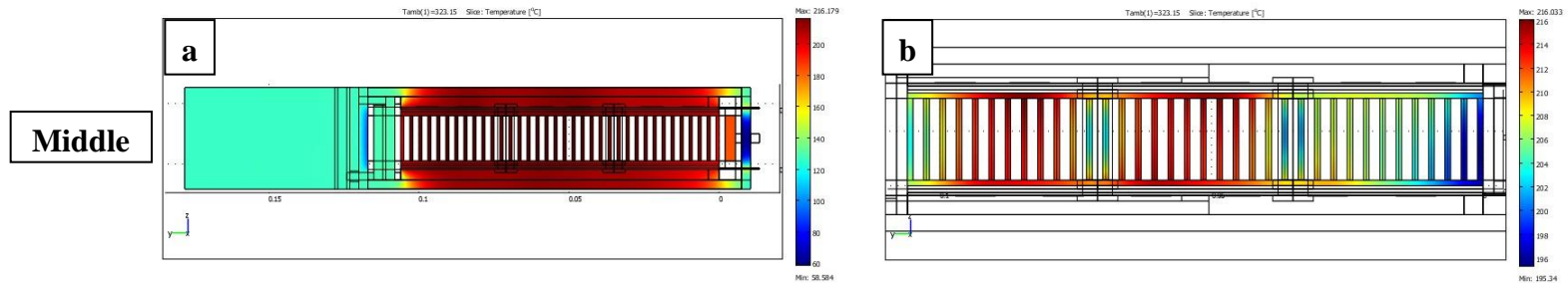


Figure 5.16 Slice plot of the temperature distribution on the middle plane with  $Q = 40$  CFM

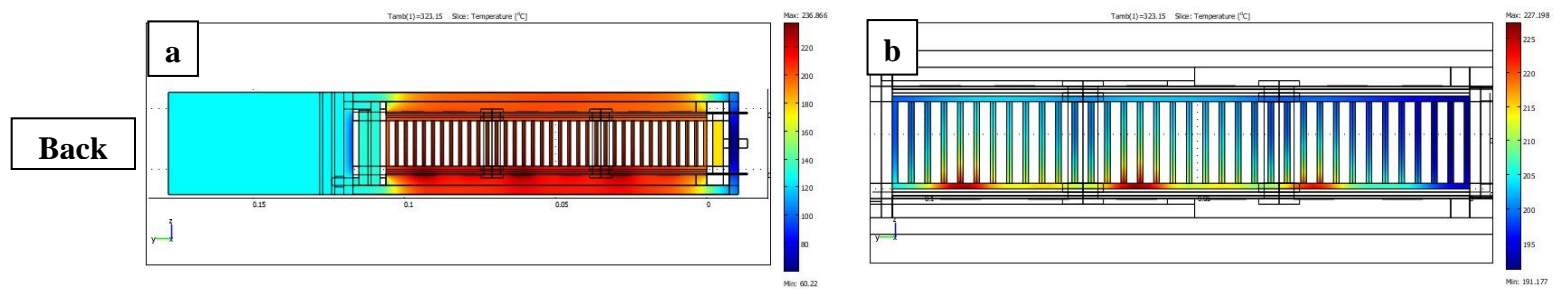


Figure 5.17 Slice plot of the temperature distribution on the back plane with  $Q = 40$  CFM

The locations of the planes used in Figures 5.19 through 5.21 are illustrated in Figures 5.18. In Figure 5.18, three horizontal planes that are parallel to the flow direction are shown. The top plane in Figure 5.18 is through the top base of the fins, the middle plane in Figure 5.18 is through the mid-plane of the fins, and the bottom plane in Figure 5.18 is through the bottom base of the fins.

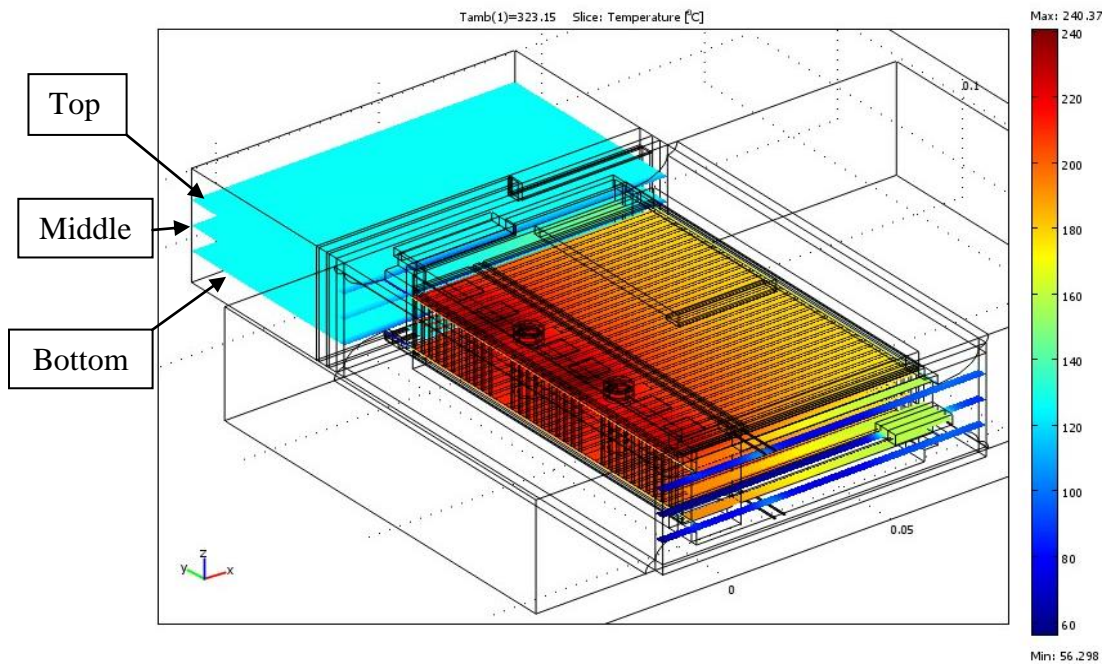


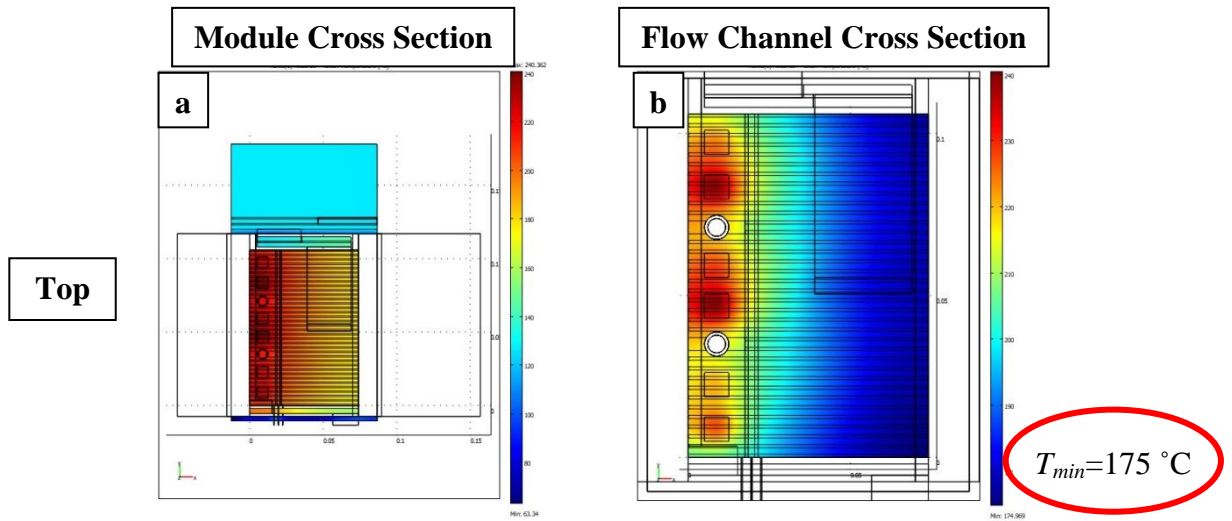
Figure 5.18 Isometric view of the slice plots showing the location of the planes used in Figures 5.19 through 5.21 and Figure 5.23

Figures 5.19 (a) through 5.21 (a) show the solid temperature distribution of a cross section of the entire module on the three horizontal planes shown in Figure 5.18, while 5.19 (b) through 5.21 (b) show the temperature distribution of a cross section of the flow channel alone on these three horizontal planes. In all of these six Figures,  $Q = 40$  CFM.

As can be seen from the temperature distribution shown in Figure 19 (b), the maximum temperature on the top plane occurs near the front of the plane. The hotspots that can be seen in Figure 5.19 (b) are the thermal footprints of the upstream devices. Since the maximum temperature is located at the front of the plane, nearly all of the heat conduction in the top plane is from the front to the back of the plane. However as can be seen in Figure 21 (b), the maximum temperature on the bottom plane is near the center of the plane. These hotspots are the thermal footprints of the downstream devices. In this plane, the heat conduction is from the center to the front of the plane, as well as the center to the back of the plane.

The minimum temperature of the fin channel with  $Q = 40$  CFM was found to be 175 °C in all three horizontal planes. This minimum temperature is significantly higher than the fluid temperature. Therefore, the entire flow channel is effective at transferring heat.

Figures 5.22 and 5.23 show the effect of changing  $Q$  from 40 to 60 CFM on the solid temperature distribution. As previously stated, changing  $Q$  only changes the magnitude of the temperature distribution. The minimum temperature of the fin channel with  $Q = 60$  CFM was found to be 123 °C.



Figures 5.19 Slice plot of the temperature distribution on the top plane with  $Q = 40$  CFM

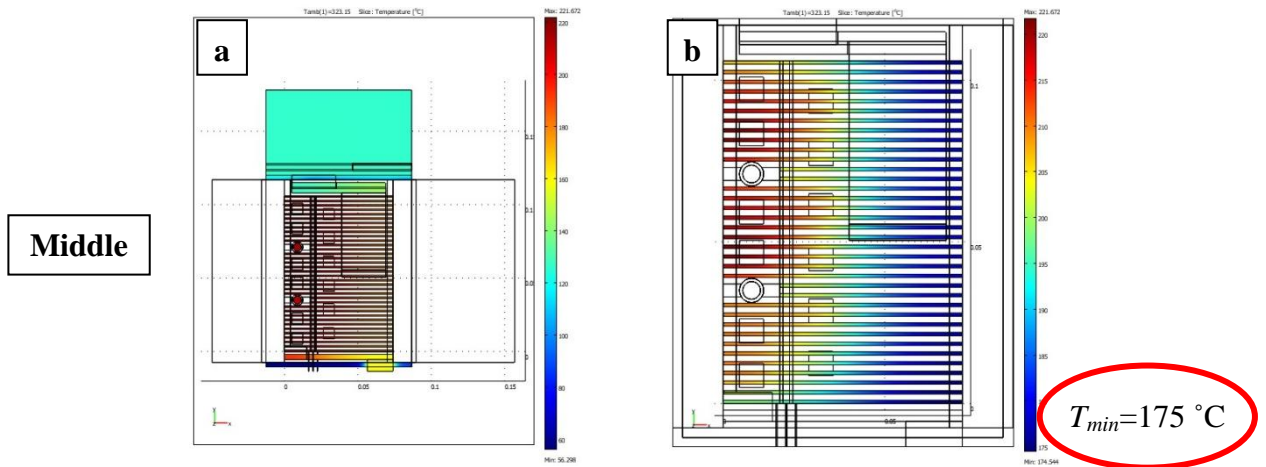


Figure 5.20 Slice plot of the temperature distribution on the middle plane with  $Q = 40$  CFM

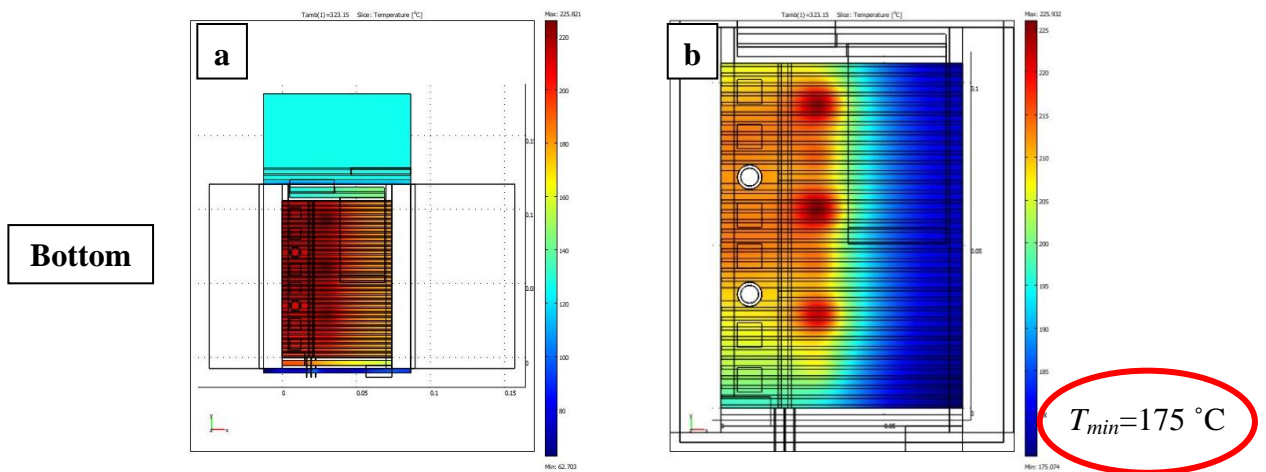


Figure 5.21 Slice plot of the temperature distribution on the bottom plane with  $Q = 40$  CFM

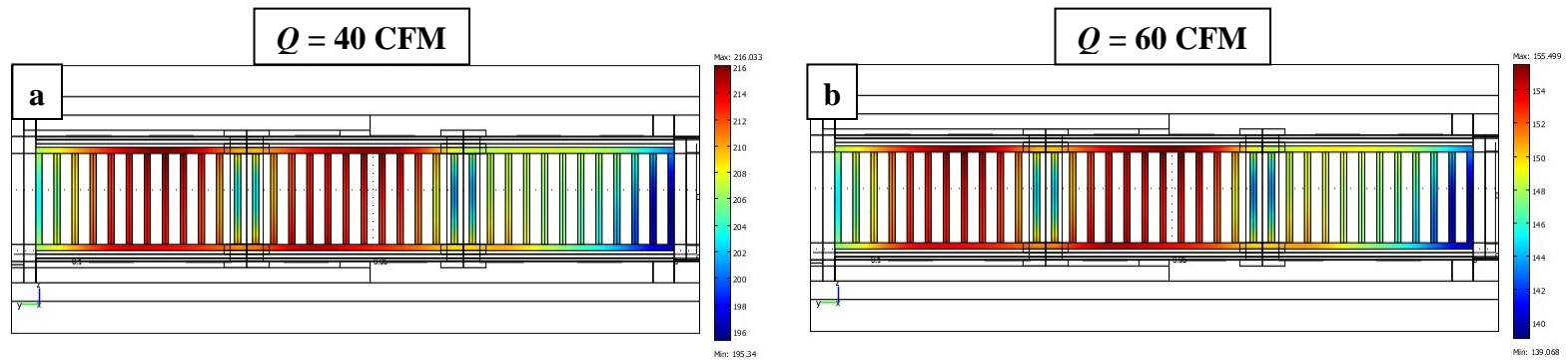


Figure 5.22 Slice plot of the temperature distribution on the middle vertical plane with  $Q = 40$  and 60 CFM

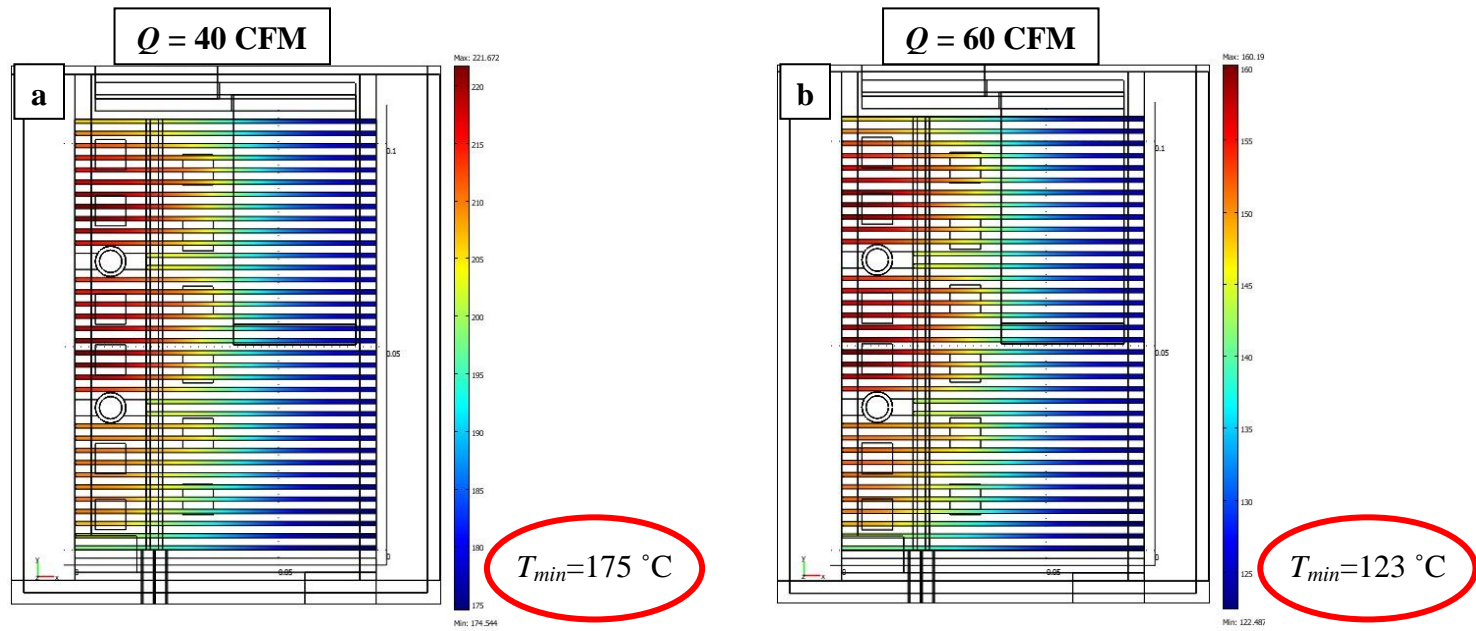


Figure 5.23 Slice plot of the temperature distribution on the middle horizontal plane with  $Q = 40$  and 60 CFM



A plot of the temperature distribution in the phase connection is given in Figure 5.24. As previously stated, in order to design a thermally self-contained module, the temperatures of the connections were lowered as much as possible before leaving the module. This was done by actively cooling the connection with air. The connection was extended in the stream-wise direction, and was exposed to the moving fluid. By making the connection longer, the resistance to heat conduction increases, and the surface area of the connection for convection heat transfer to occur increases. Therefore, the temperature of the connection decreases substantially from the card to the exit of the module. This concept was applied to the DC and gate connections as well. A plot of the temperature distribution in the gate connections is given in Figure 5.25. Since the cross sectional area of these connections is so small, there was no need to extend them in the stream-wise direction in the flow domain.

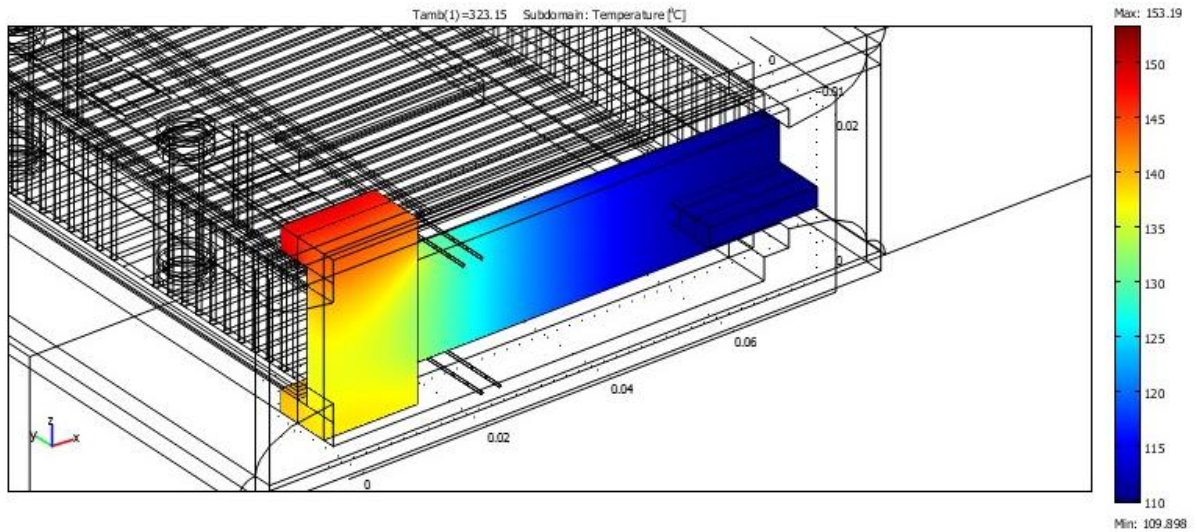


Figure 5.24 Isometric view of the temperature distribution in the phase connection leaving the module with  $Q = 60$  CFM and  $T_{inlet} = 50$  °C

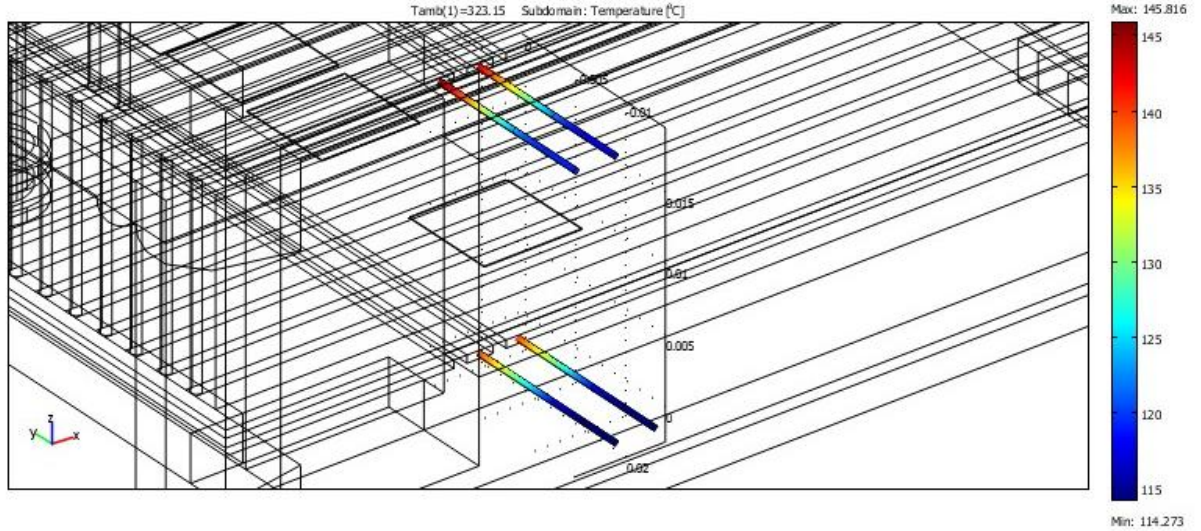


Figure 5.25 Isometric view of the temperature distribution in the gate connections leaving the module with  $Q = 60$  CFM and  $T_{inlet} = 50$  °C

The temperature distribution in the DC connections is given in Figures 5.26 and 5.27. Lowering the temperature of these two connections before they leave the module was very important and challenging. This is because the DC connections connect to the capacitor after leaving the module, and the capacitor has strict temperature requirements. To lower the temperature of these connections, the strategy of actively cooling them by extending them in the stream-wise direction and exposing them to the moving fluid was implemented. In order to electrically isolate the two connections from one another, a layer of aluminum nitride was placed in between the two DC connections. If the connections need to be cooled further, the aluminum nitride can be removed to allow air to flow in between the connections. This additional cooling should prove to be effective in lowering the DC connection temperatures further.

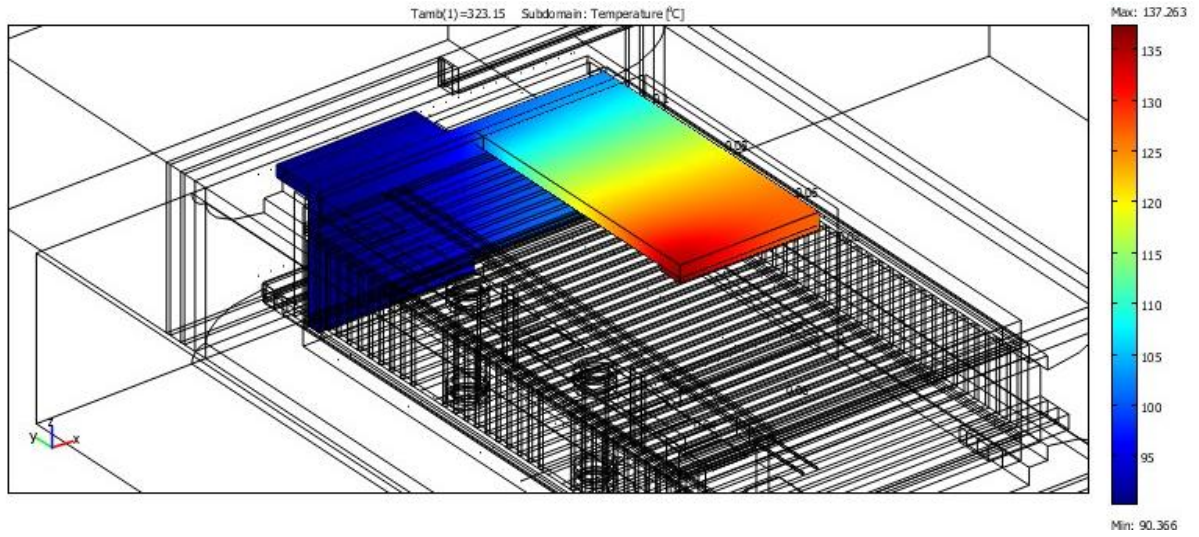


Figure 5.26 Isometric view of the temperature distribution in the DC negative connection with  $Q = 60$  CFM and  $T_{inlet} = 50$  °C

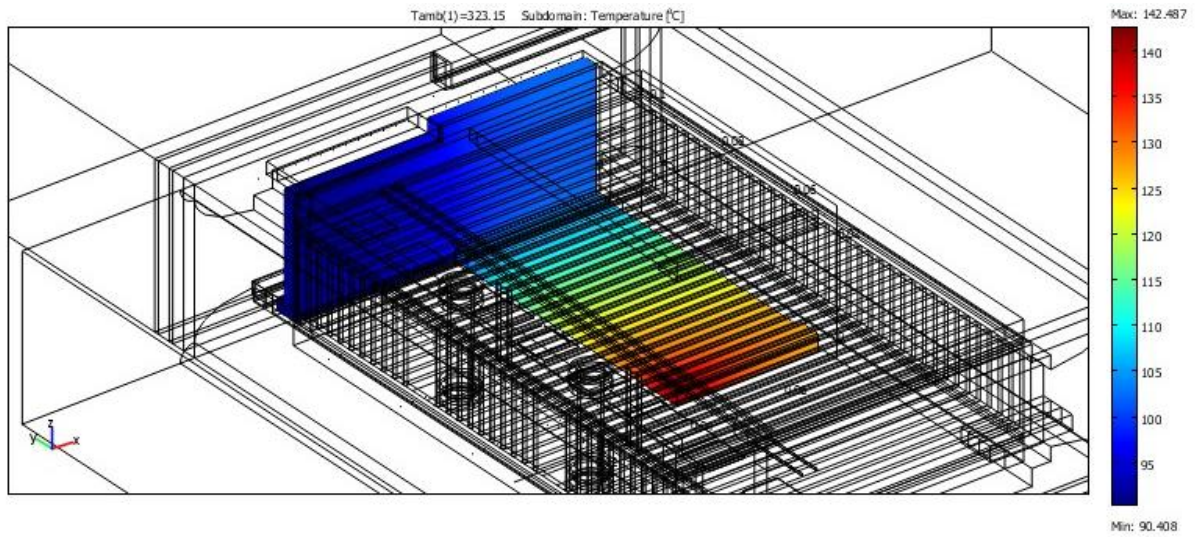


Figure 5.27 Isometric view of the temperature distribution in the DC positive connection with  $Q = 60$  CFM and  $T_{inlet} = 50$  °C



A plot of the temperatures of the connections leaving the module versus  $T_{inlet}$  for all flow rates considered are given in Figures 5.28 though 5.30. In order to conclude the module design is thermally self-contained, the temperature of the connections leaving the module must be reasonable. Therefore, the temperatures of the connections were determined from the simulations, and are presented here for discussion.

The temperature of the connections varies directly with  $T_{inlet}$  similar to the device temperatures. An increase in flow rate decreases the temperatures of the connections, but the reward diminishes. All connection temperatures vary nonlinearly with  $T_{inlet}$  similar to the devices. Whether these temperatures are reasonable or not depends on the specific application in mind. For this application, it was determined that the temperatures of the connections leaving the module are reasonable.

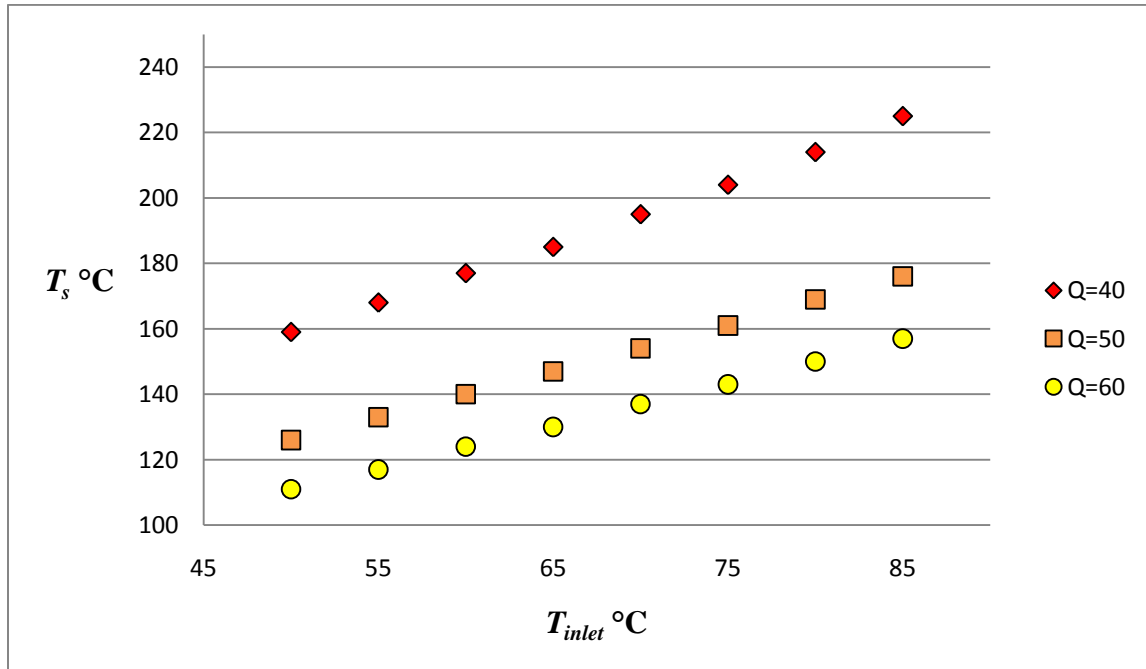


Figure 5.28 Plot of the phase connection temperatures leaving the module versus  $T_{inlet}$

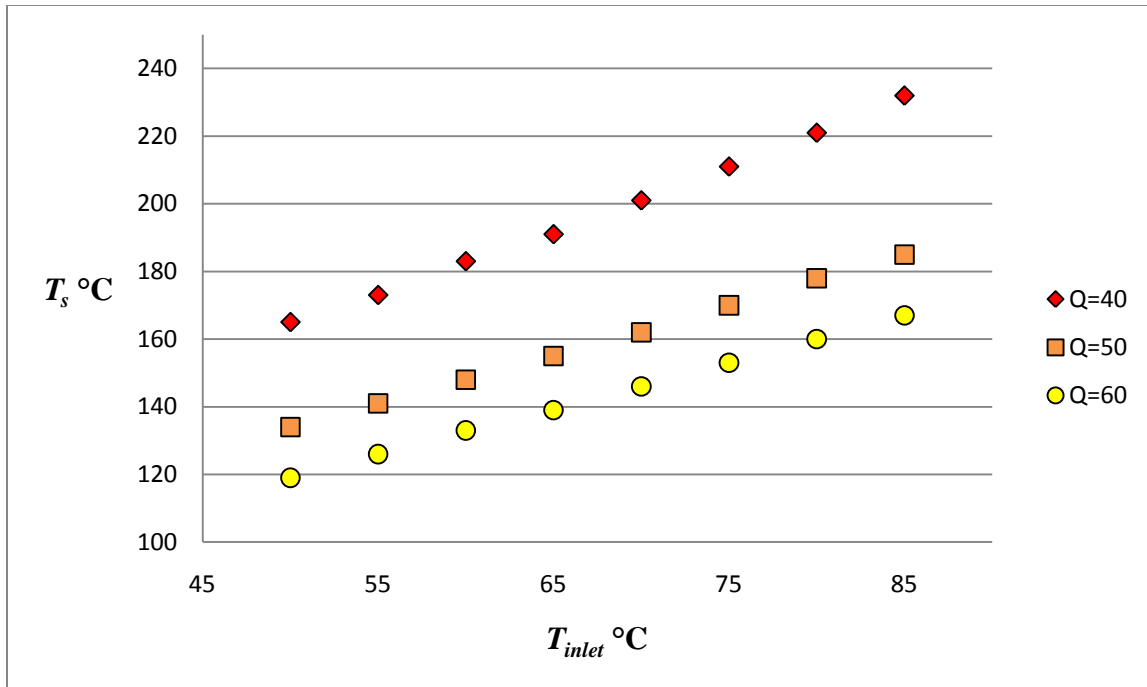


Figure 5.29 Plot of the gate connection temperatures leaving the module versus  $T_{inlet}$

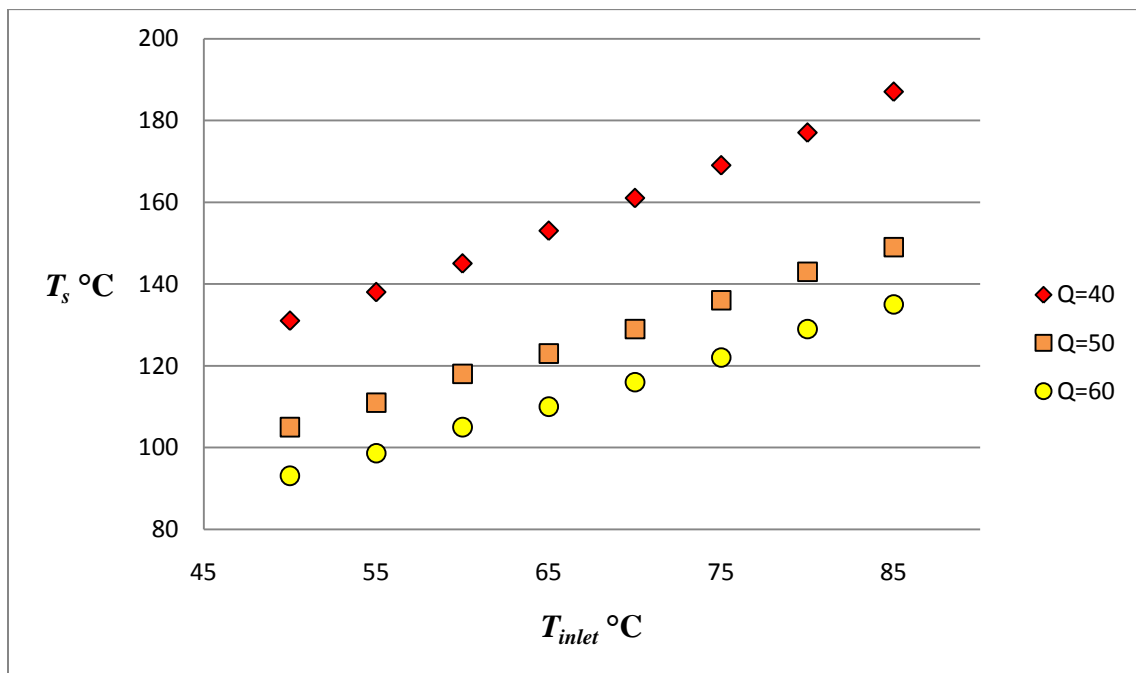


Figure 5.30 Plot of the DC connection temperatures leaving the module versus  $T_{inlet}$

Table 5.3 presents the results for the temperature of the connections leaving the module, and the temperature of the capacitor versus  $T_{inlet}$  for flow rates of 40, 50, and 60 CFM.

Table 5.4 Temperatures of the connections and the capacitor from the steady state temperature simulations

$Q = 40$ CFM								
$T_{inlet}$ °C	50	55	60	65	70	75	80	85
Phase Connection °C	159	168	177	185	195	204	214	225
Gate Connection °C	165	173	183	191	201	211	221	232
DC Connection °C	131	138	145	153	161	169	177	187
Capacitor °C	127	134	142	149	157	165	173	182
$Q = 50$ CFM								
$T_{inlet}$ °C	50	55	60	65	70	75	80	85
Phase Connection °C	126	133	140	147	154	161	169	176
Gate Connection °C	134	141	148	155	162	170	178	185
DC Connection °C	105	111	118	123	129	136	143	149
Capacitor °C	102	108	115	120	126	133	140	146
$Q = 60$ CFM								
$T_{inlet}$ °C	50	55	60	65	70	75	80	85
Phase Connection °C	111	117	124	130	137	143	150	157
Gate Connection °C	119	126	133	139	146	153	160	167
DC Connection °C	93.1	98.6	105	110	116	122	129	135
Capacitor °C	90.9	96.3	102	108	114	120	126	132

A plot of the temperature distribution in the module casing is given in Figure 5.31. Note the magnitude of the temperature difference in the material. The maximum temperature in the module casing with  $Q = 60$  CFM and  $T_{inlet} = 50$  °C was determined to be 170 °C, and the minimum temperature was determined to be 52 °C. This large temperature difference is evidence that Torlon™ has a low thermal conductivity, and does not diffuse energy well.

The maximum allowable operating temperature of Torlon™ is given by the manufacturer to be 250 °C. Therefore, all temperatures within the model have met the temperature requirements of the manufacturers. After analyzing the results of the steady state finite element simulation of the module design with a volumetric flow rate of 60 CFM, we have determined that air-cooling the proposed WBG inverter is thermally feasible.

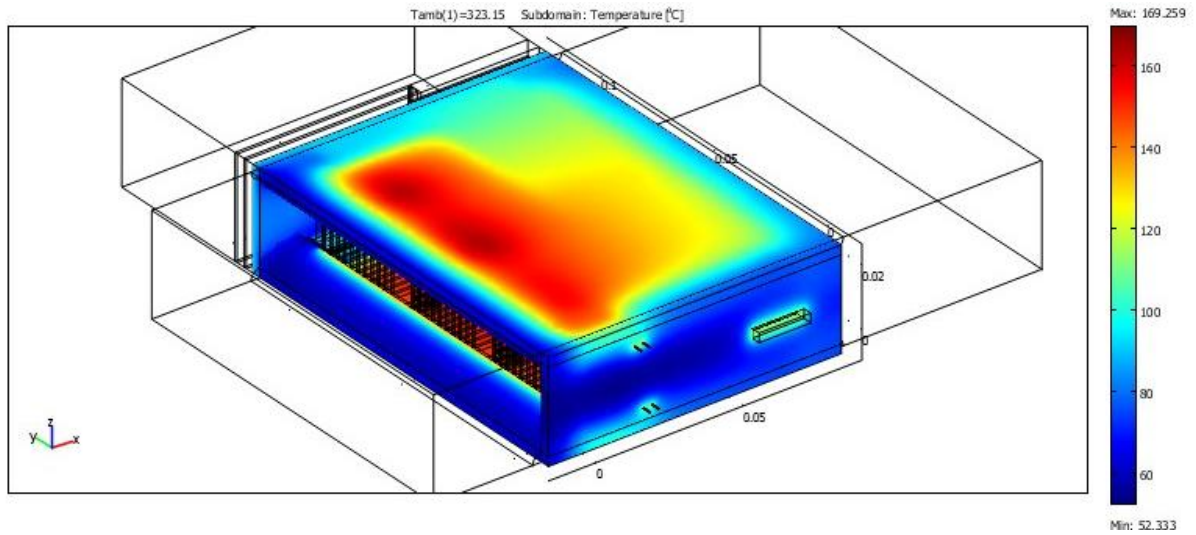


Figure 5.31 Isometric view of the temperature distribution in the module casing with  $Q = 60$  CFM and  $T_{inlet} = 50$  °C

A plot of the temperature distribution in the fluid domain is given in Figures 5.32 through 5.34. The fluid temperature was specified to be 50 °C at the inlet. Notice the wake of the phase bolts and phase connection in Figures 5.33 and 5.34. The fluid temperature is significantly higher in this wake than in the rest of the finned flow channel. There are several reasons why this is happening. First, the material for the phase bolts is copper, and has a higher thermal conductivity than the aluminum finned flow channel. The high thermal conductivity and the relatively high cross sectional area of the phase bolts results in a small resistance to heat conduction. Since the bases of the bolts are close to the heat sources, they are also very hot. This makes the bolts very effective fins for heat transfer. Figure 5.33 is a slice plot of the temperature distribution through the middle horizontal slice of the fluid domain, and Figure 5.34 is a slice plot of the temperature distribution at the exit of the fluid domain.

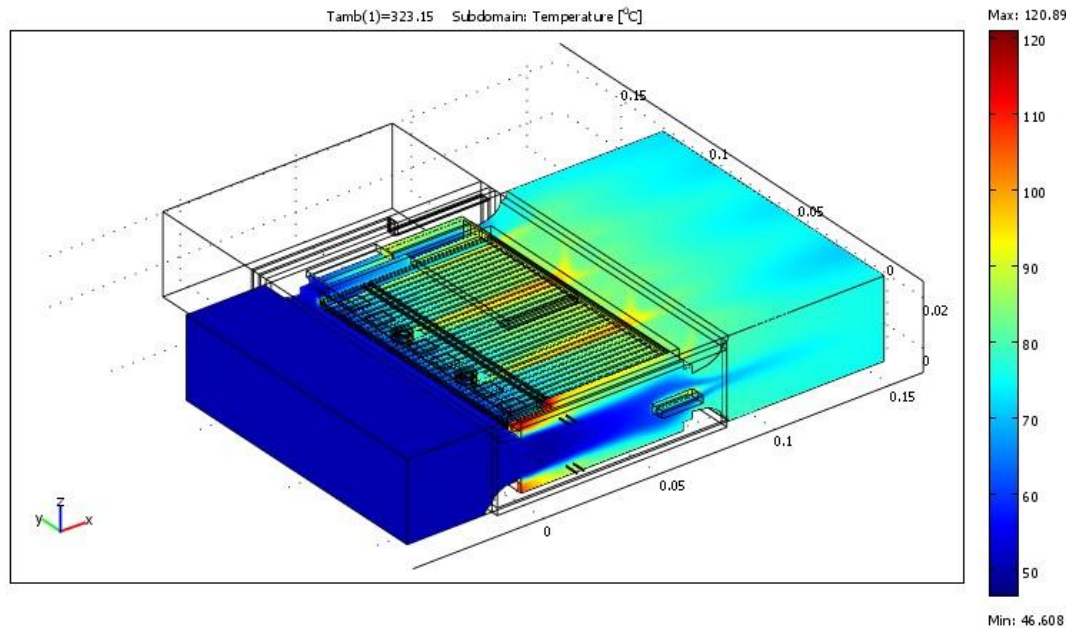


Figure 5.32 Isometric view of the fluid temperature distribution with  $Q = 60$  CFM and  $T_{inlet} = 50$  °C

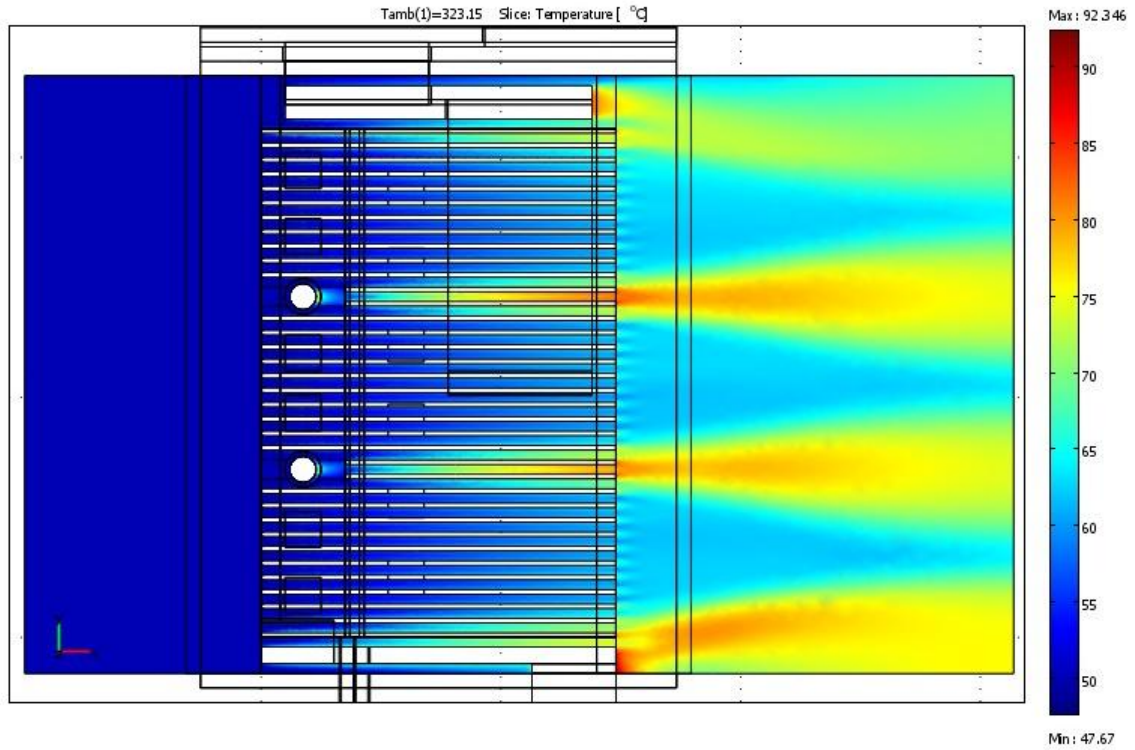


Figure 5.33 Top view of a slice plot of the fluid temperature distribution through the middle horizontal slice of the fluid domain with  $Q = 60$  CFM and  $T_{inlet} = 50$  °C

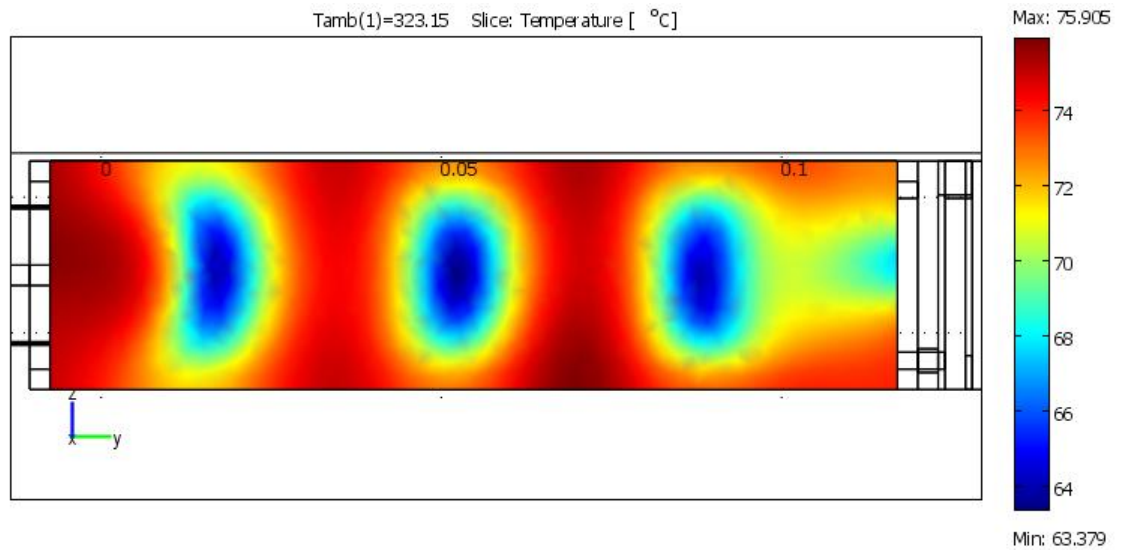


Figure 5.34 Side view of a slice plot of the fluid temperature distribution at the exit plane of the fluid domain with  $Q = 60$  CFM and  $T_{inlet} = 50$  °C

Table 5.5 provides a comparison of the results from the steady state simulations of the FY 2009 and FY 2010 projects. The ideal blower power requirements of the rectangular shaped inverter were 89 % less than the annular inverter from the FY 2009 study. Using the heat generation equations detailed in Section 3.7, the resulting heat generation rate in the 2010 study with  $Q = 60$  CFM and  $T_{amb} = 50$  °C was determined (from the solution) to be 610 W per module, while the heat generation rate in the FY 2009 study was specified to be 192 W per unit cell. In spite of the increase in the total heat load, the design under consideration achieved a lower maximum device temperature with  $Q = 60$  CFM and  $T_{amb} = 50$  °C.

Table 5.5 Comparison of the results of the steady state temperature simulations from the FY 2009 and FY 2010 studies with  $Q = 60$  CFM,  $T_{inlet} = T_{amb} = 50$  °C

Performance Parameters	units	FY 2009 Without Fins	FY 209 Final Design with Fins	FY 2010
$T_s$ max	°C	380	200	184
Pressure Drop	Pa	3400	3500	411
Ideal Blower Power	W	940	970	105
Total Heat Load	W	192	192	610

### 5.3 Special Steady State Simulation

After completing the steady state simulations, the time dependent input for current that was deduced from the US 06 drive cycle was implemented in the transient simulations. Before running the transient simulations, a special steady state simulation was studied. This special simulation is now discussed.

As can be seen in Figure 5.35, the transient current distribution has three distinct patterns; a relatively high level of current in the beginning up to about 194 s, followed by a low level of currents up to a time of 482 s, and ending with a third high level of current. In the three time intervals, an integrated average value of current was computed. The average current of these three time intervals are shown by the red lines in the Figure 5.35 [15] and given in Table 5.6 [15].

Table 5.6 Average current of the transient current distribution over three intervals [15]

Time dependent input for current deduced from the US 06 Drive Cycle			
Time interval in the US06 Drive Cycle	1 - 194 s	194 to 482 s	482 to 602 s
Integrated average current A through Inverter As shown by the redlines in Figure 5.35	56.31	34.19	82.45



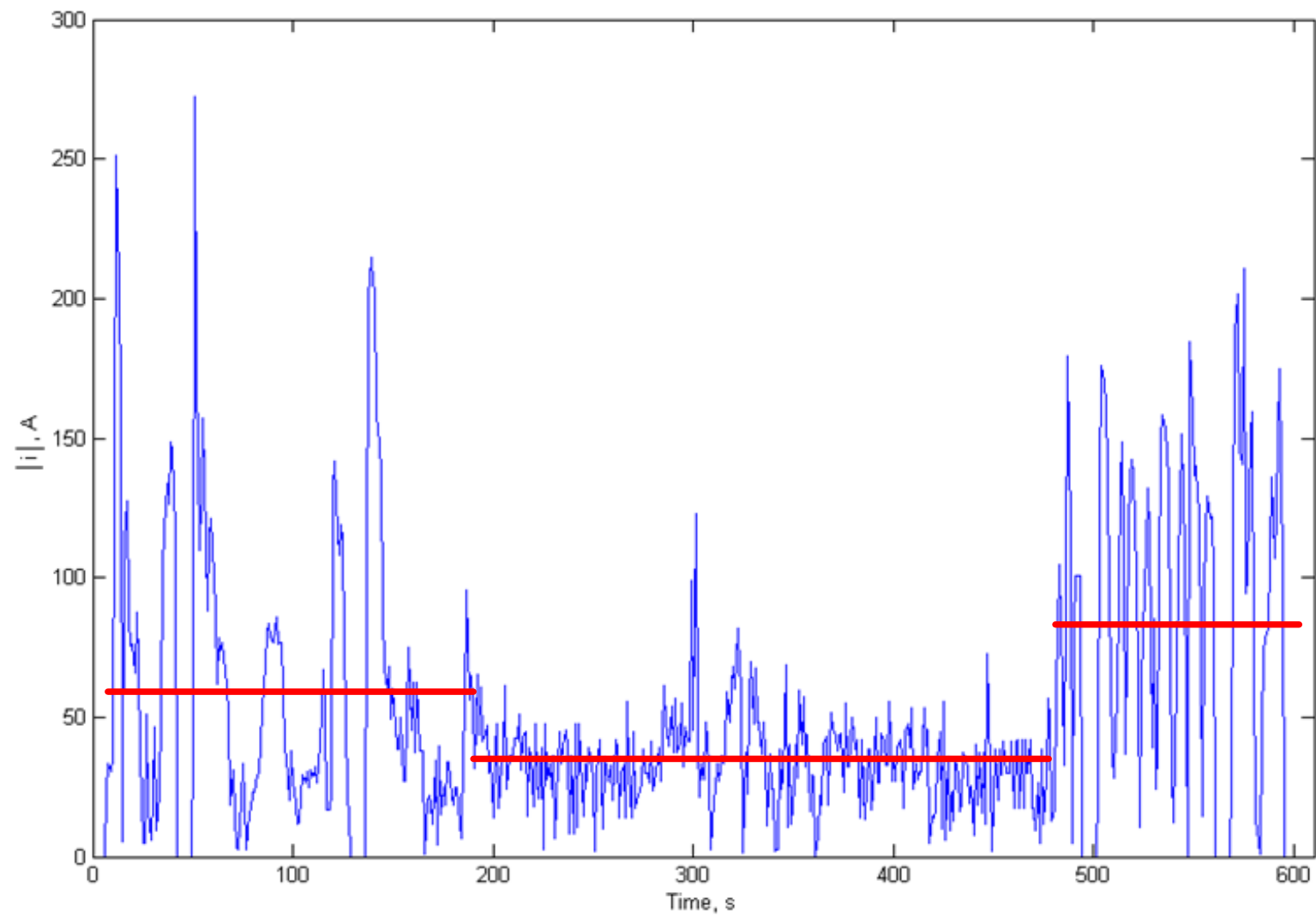


Figure 5.35 Plot of the input current for the transient simulations with lines showing the average current over three distinct intervals [15]

In an attempt to estimate the maximum device temperatures that would be present in the transient simulation, a special steady state simulation was studied with  $I = 82.45$  A,  $Q = 30$  CFM,  $T_{amb} = 120$  °C,  $T_{inlet} = 50$  °C,  $V = 650$  V, and  $f_{sw} = 20$  kHz. The results from this simulation are shown in Figure 5.36. The maximum device temperature was determined to be 101 °C, and  $\dot{E}_{Gen}$  was determined to be 160 W for this simulation.

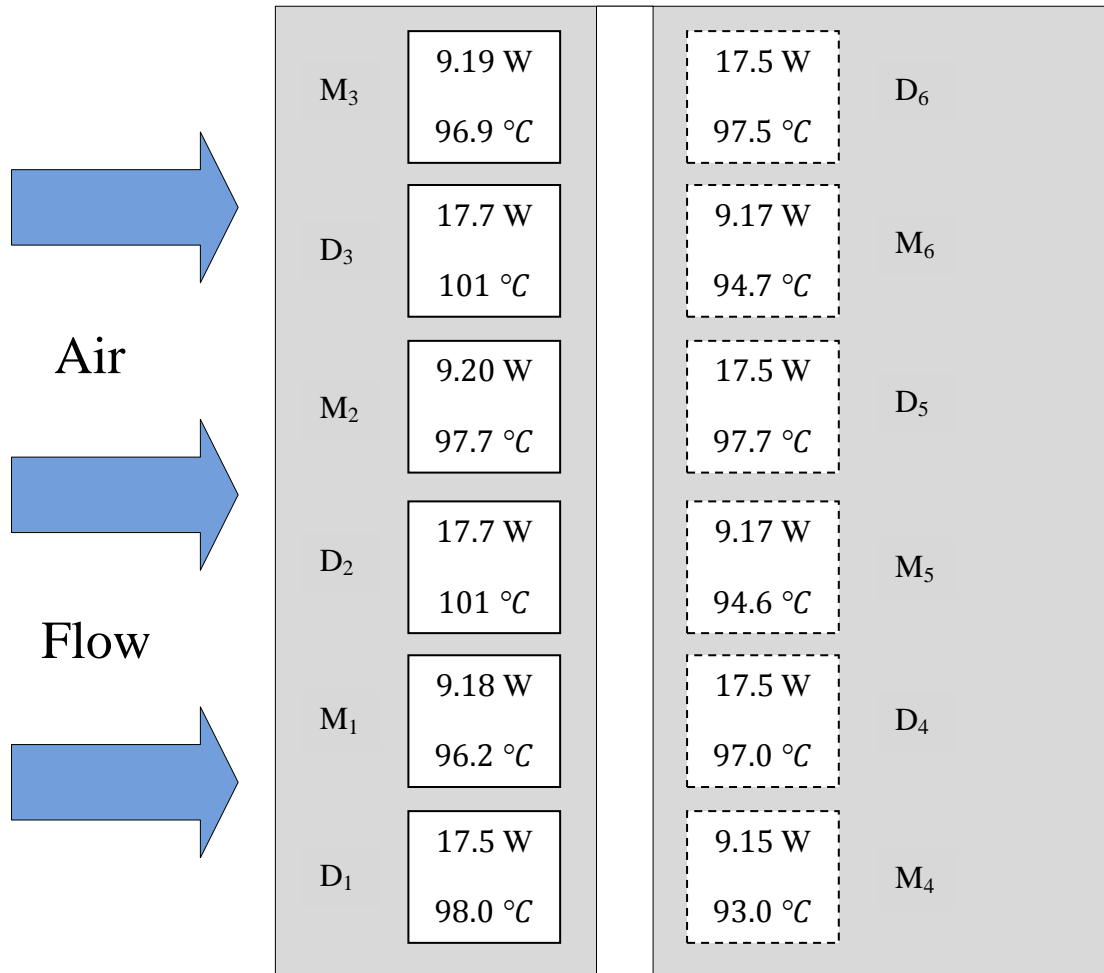


Figure 5.36 Top view of the card with the results from the special steady state simulation with  $Q = 30$  CFM,  $T_{amb} = 120$  °C,  $T_{inlet} = 50$  °C,  $V = 650$  V,  $f_{sw} = 20$  kHz,  $I = 82.5$  A. M and D represent MOSFET and diode, respectively.

## 5.4 Transient Temperature Results

Using the transient current distribution deduced from the US06 drive cycle, a total of 16 different transient cases were simulated comprising of all possible combinations from two selected values for each of four parameters of interest. They are volumetric flow rates of air of 30 and 60 CFM, voltages of 450 and 650 V, switching frequencies of 10 and 20 kHz, and ambient temperatures of 50 and 120°C. In all cases studied, the maximum device temperatures occur in the diode in the middle of the phase trace of the card. The results shown in Table 5.7 correspond to that diode during one drive cycle.

Table 5.7 Results of the transient temperature simulations for maximum device temperatures

$Q$ , CFM	$T_{amb}$ , °C	Voltage, V	$f_{sw}$ , kHz	$T_{max}$ , °C
30	50	450	10	86
30	50	450	20	91
30	50	650	10	94
30	50	650	20	111
30	120	450	10	130
30	120	450	20	132
30	120	650	10	136
30	120	650	20	146
60	50	450	10	80
60	50	450	20	83
60	50	650	10	89
60	50	650	20	98
60	120	450	10	122
60	120	450	20	125
60	120	650	10	128
60	120	650	20	138

For all transient cases studied, the inlet air temperature was specified to be 50 °C. Furthermore, the initial temperature of the entire module was specified to be uniform and equal to  $T_{amb}$ . Figure 5.37 (a) through 5.37 (d) show the effect of changing one of the parameters of interest. Figure 5.38 (a) through 5.38 (d) is a plot of the temperature response of all 16 transient simulations.

An increase in voltage, an increase in switching frequency, or a decrease in flow rate has a very similar effect on the temperature response of the simulation. If the voltage is increased, the switching frequency is increased, or the flow rate is decreased, the device temperature across the entire cycle is increased with an exception of the start of the cycle. A change in flow rate results in a change on the temperature response of the simulation, and a change in switching frequency results in the smallest effect on the temperature response of the simulation.

Figure 5.37 (b) shows the effect of changing  $T_{amb}$  on the temperature response. Changing  $T_{amb}$  has a significant effect on the start of the cycle. However by the end of the cycle, the effect of changing  $T_{amb}$  is diffused out of the temperature response which can be seen in Figure 5.37 (b). Both simulations with  $T_{amb} = 50$  °C and  $T_{amb} = 120$  °C end up at approximately the same final (end of the cycle) temperature. This is a desirable result. If the simulations were carried out for more than one cycle, the effect of the ambient condition would be diffused out in the first cycle, the maximum device temperatures would occur at the end of the cycle for both  $T_{amb} = 50$  and 120 °C. Therefore, caution should be taken when comparing the results in Table 5.7 for simulations with different values of  $T_{amb}$ .

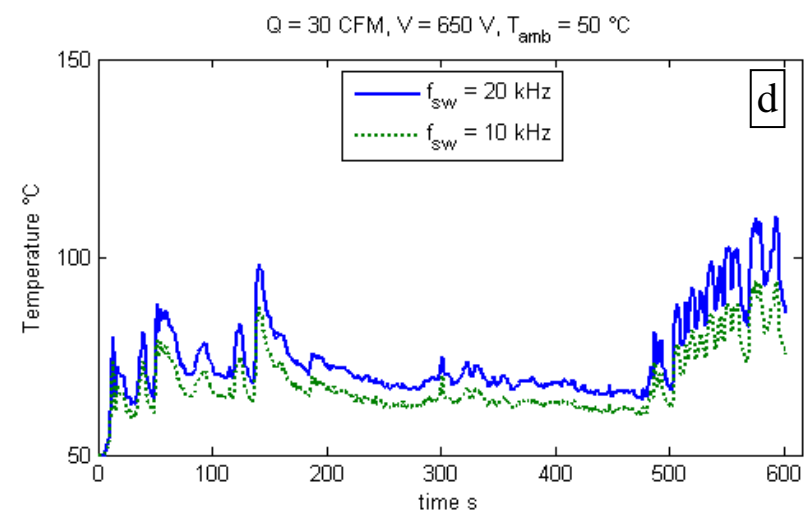
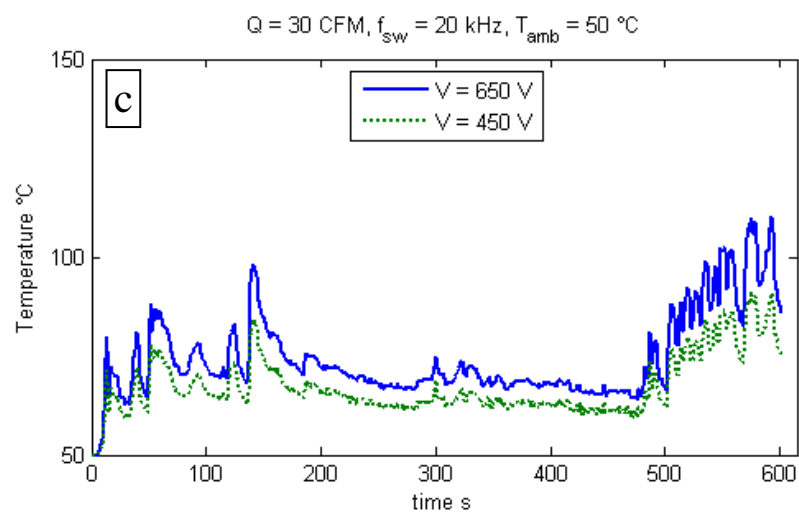
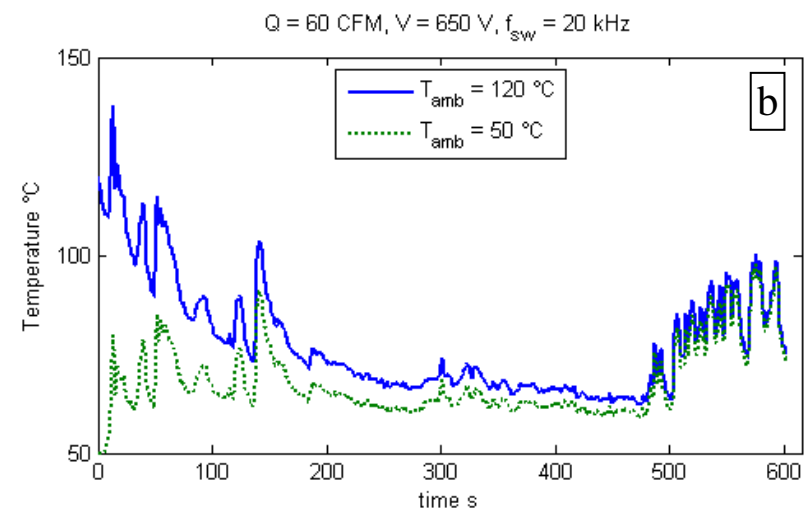
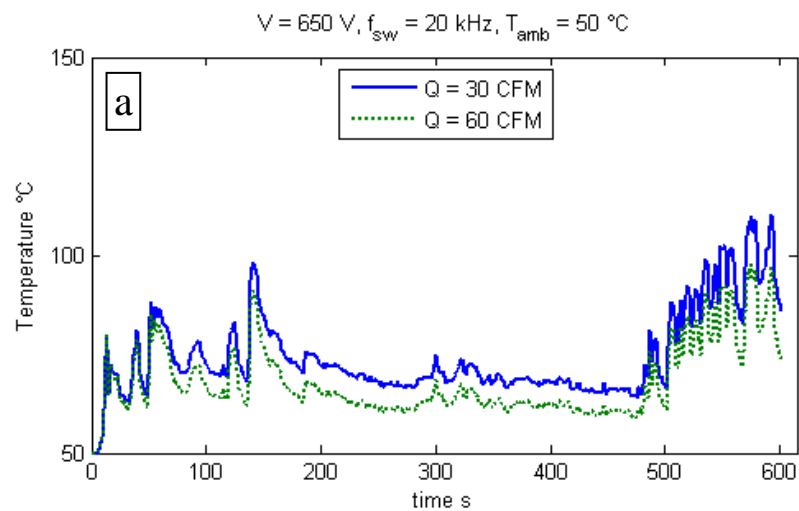


Figure 5.37 Plot of the transient results showing the effect of changing  $Q$ ,  $T_{amb}$ ,  $V$ , and  $f_{sw}$  with  $T_{inlet} = 50 \text{ }^{\circ}\text{C}$

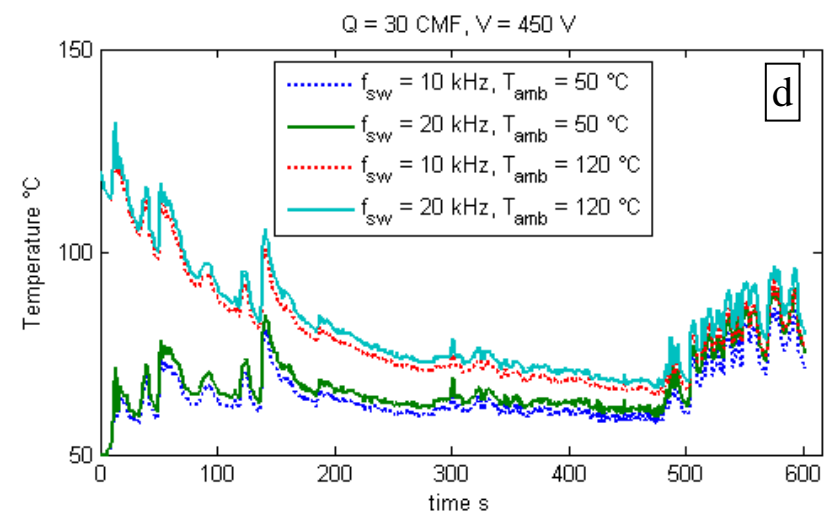
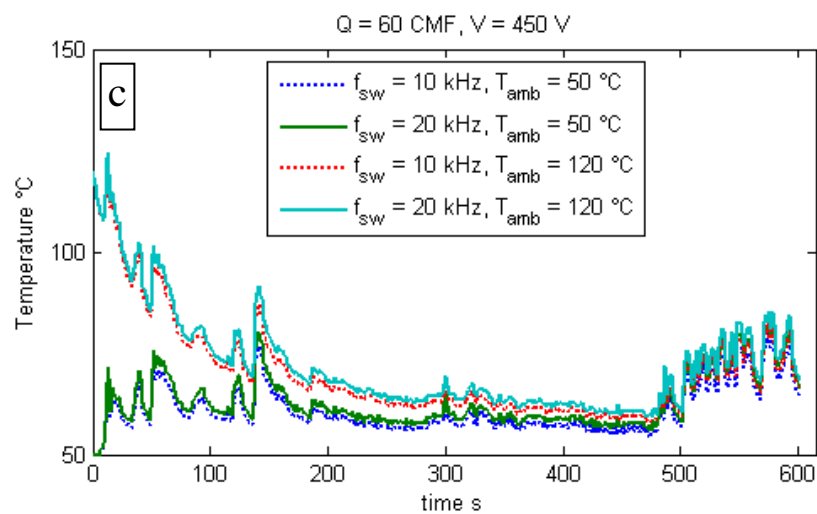
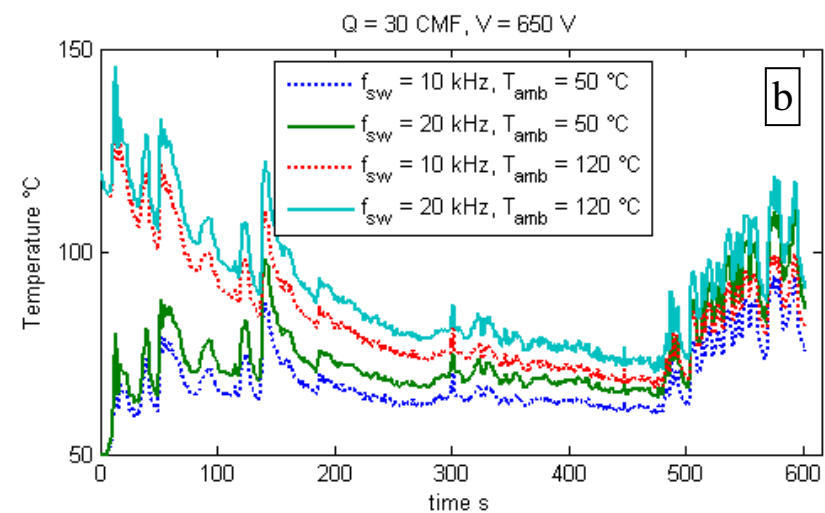
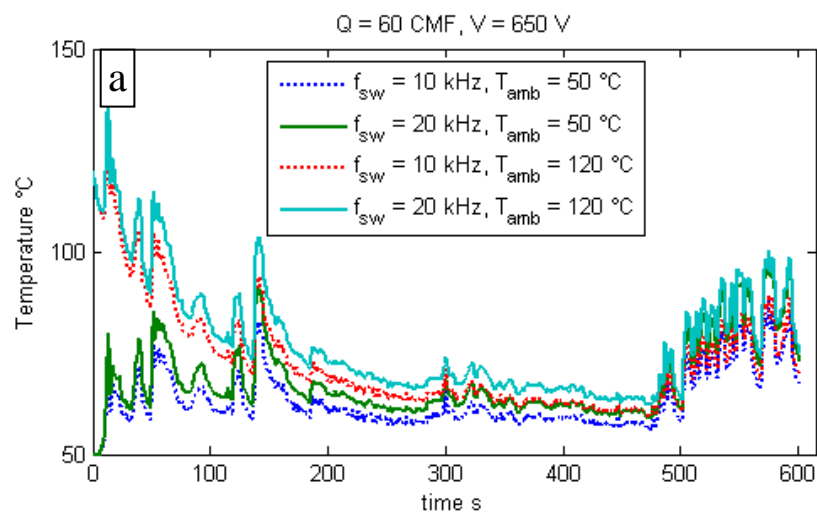


Figure 5.38 Plot of all 16 transient simulations of the US06 drive cycle with  $T_{inlet} = 50 \text{ }^{\circ}\text{C}$

## 5.5 Validation of the Results

It is important to validate the results of any numerical simulation. For a steady state steady flow simulation, the mass and energy balance should always be checked to determine the accuracy of the results. This was done in all steady state models. The largest relative error in mass balance for the six velocity simulations was found to be less than 5 %. This is an acceptable error considering the simulations involve a 3-D fully turbulent flow field. For the temperature simulations, the largest relative error in the global energy balance for all steady state models was found to be less than 8%. This is also an acceptable relative error considering the complexity of the model.

However, the assumptions that were made to simplify the simulations should be kept in mind when analyzing the results. First, the flow field was assumed to be incompressible. This is a valid assumption for this problem because the maximum velocity in the model is less than thirty percent of the speed of sound for air, and density will be constant throughout the fluid domain. The second major assumption that was made to simplify the simulations was that of constant viscosity. The difference in bulk temperature from the inlet to the exit of the fluid domain in these models was at most 29 °C. The difference in viscosity over this temperature difference is approximately 11 %. Therefore, this assumption will affect the accuracy of the results. Recall that the assumption of constant viscosity allowed us to uncouple the energy equation from the mass and momentum equations. While this is a more restrictive assumption, it decreased the amount of computational resources required to complete this study. The only relevant physics not modeled are contact thermal resistance and radiation. Both of these phenomena will be present in the real world.

## Chapter 6. Conclusions

The objectives of this study were to design a feasible air-cooling system for the proposed rectangular inverter while substantially reducing the blower power requirements relative to the FY 2009 design, incorporating temperature dependent heat generation equations into the simulations, and incorporating a time dependent input for current into the simulations that was deduced from the US 06 drive cycle. These objectives were met. The specific conclusions are presented below.

1. The results from the steady state mass and momentum transport simulations of the rectangular inverter configuration showed that substantial reduction of the convective acceleration term that was associated with the narrowing of the cross sectional area of the fluid domain can be achieved. By reducing this term, the pressure drop across the inverter was reduced from 3473 Pa in the FY 2009 design to 411 Pa for a flow rate of 60 CFM per module. The reduction in pressure drop across the inverter results in a corresponding reduction in the blower power required to drive a certain flow rate through the inverter. The ideal blower power required to drive a flow rate of 60 CFM per module was reduced from 967 W to 105 W, which is about one ninth of the previous requirement.
2. The following conclusions are drawn from the results of the steady state energy transport simulations.
  - (a) It is indeed feasible to cool the proposed rectangular inverter with air. In order to meet the temperature requirements of the devices, a minimum flow rate of 50 CFM per module should be used with  $T_{inlet} = T_{amb} = 50\text{ }^{\circ}\text{C}$ .



(b) Increasing flow rate decreases the magnitude of the temperature distribution throughout the entire inverter. However, due to the nonlinear nature and temperature dependence of the heat generation equations, the benefits associated with increasing the flow rate diminishes quickly. For  $50 \ll T_{inlet} \ll 85^{\circ}\text{C}$ , increasing the air flow rate beyond 50 CFM per module of air through the inverter would be excessive for the design presented in this thesis.

3. The following conclusions are drawn from the results of the transient energy transport simulations.

(a) When the proposed inverter is subjected to the time-dependent input for current that was deduced from the EPA US 06 drive cycle, it is feasible to cool the proposed rectangular inverter with air for all flow rates considered in this study.

(b) Device temperatures are substantially reduced when current varies with time. A flow rate of 30 CFM per module was more than adequate to accomplish the cooling task, and the highest device temperature in all transient simulations was found to be  $146^{\circ}\text{C}$  which is far less than the maximum device temperature specified by the manufacturer.

## List of References

- [1] K. Lowe, I. Bodey, J. Faulkner, and R.V. Arimilli, *Annual Technical Report on the Feasibility of Thermal Packaging of Air-Cooled WBG Inverter*, University of Tennessee, Knoxville, Tn. September, 2009.
- [2] [www.epa.gov](http://www.epa.gov), January 2011.
- [3] K. Lowe, *Direct Cooled Ceramic Substrate for Thermal Control of Automotive Power Electronics*, Ph.D. Dissertation, University of Tennessee, Knoxville, Tn. Dec. 2009.
- [4] A. Bergles, *Evolution of cooling technology for electrical, electronic, and microelectronic equipment*, *Components and Packaging Technologies, IEEE Transactions on* , vol.26, no.1, pp. 6- 15, March 2003
- [5] T. Gradinger, Y. Liu, *Fast and Accurate Simulation of Time-Variant Air-Cooling Systems*, 6th International Conference on Integrated Power Electronics Systems , Nuremberg Germany, 2010.
- [6] F. M. White, *Viscous Fluid Flow*, 3rd ed. McGraw-Hill, 2006.
- [7] F. M. White, *Fluid Mechanics*, 5th ed. McGraw-Hill, 2006
- [8] COMSOL 3.5a *Reference Guide*, COMSOL Multiphysics.
- [9] F. P. Incropera and D. P. Dewitt, *Fundamentals of Heat and Mass Transfer*, 5<sup>th</sup> ed. John Wiley & Sons, Inc, 2002.
- [10] M. Chinthavali, Oak Ridge National Laboratory, personal communication.
- [11] [www accuratus.com](http://www accuratus.com), January, 2011.
- [12] F. Breit, D. Malec, and T. Lebey, “Investigations on DC conductivity and space charge in silicone gel,” in *Electrical Insulation and Dielectric Phenomena, 2002 Annual Report Conference on*, pp. 48–51, Semeac, France, 2002.
- [13] [www.designwithtorlon.com](http://www.designwithtorlon.com), January, 2011.
- [14] J. D. Scofield, J. N. Merrett, J. Richmond, A. Agarwal, S. Leslie, *Performance and Reliability Characteristics of 1200 V, 100 A, 200 °C Half-Bridge SiC MOSFET-JBS Diode Power Modules*, IMAPS International Conference & Exhibition on High Temperature Electronics, Albuquerque, New Mexico, 2010.
- [15] J. Tawfik, J. Faulkner, R.V. Arimilli, and I. Bodey, *Design and Parametric Study of the Performance of Rectangular and Annular Inverters*, University of Tennessee, Knoxville, Tn. September, 2010.

## **Vita**

Jacob Christopher Faulkner was born in Oklahoma City, Oklahoma, on June 13, 1985. Raised in Jackson Tennessee, Jacob attended Saint Mary's Elementary School before attending North Side High School. He played four years of varsity baseball at North Side High before graduating in 2004. Jacob pursued his Bachelor's of Science in Mechanical Engineering at Tennessee Tech University, before transferring to the University of Tennessee in Knoxville. He graduated with his degree in 2009. During these studies, he worked as an intern for Alstom Power Inc. in Knoxville.

Jacob continued his graduate education at the University of Tennessee in Knoxville while working on a funded graduate research project through Oak Ridge National Laboratory. He will receive his Master of Science degree in Mechanical Engineering with a concentration in heat transfer and fluid mechanics in May 2011.

Jacob plans to join the Pressure Pumping & Chemistry Product Group (PPC) of Schlumberger's Research, Engineering, Manufacturing, & Sustaining (REMS) department in Sugar Land Texas as a Mechanical Engineer in June, 2011.